

ADVANCEMENTS TO PERFORMANCE-BASED EARTHQUAKE ENGINEERING  
METHODS: FROM BUILDING CODE PROVISIONS TO REGIONAL LOSS ASSESSMENT

by

D. JARED DEBOCK

B.S. California State University, Chico

M.S. University of Colorado, Boulder

A thesis submitted to the

Faculty of the Graduate School of the

University of Colorado in partial fulfillment

of the requirement for the degree of

Doctor of Philosophy

Department of Civil, Environmental, and Architectural Engineering

2013

This thesis entitled:  
Advancements to Performance-Based Earthquake Engineering Methods: From Building Code  
Provisions to Regional Loss Assessment  
Written by D. Jared DeBock  
Has been approved for the Department of Civil, Environmental, and Architectural Engineering

---

(Abbie Liel)

---

(Jack Baker)

---

(Ross Corotis)

---

(Shideh Dashti)

---

(Keith Porter)

Date \_\_\_\_\_

The final copy of this thesis has been examined by the signatories, and we  
Find that both the content and the form meet acceptable presentation standards  
Of scholarly work in the above mentioned discipline.



DeBock, David Jared (Ph.D., Civil Engineering, Department of Civil, Environmental, and Architectural Engineering)

Advancements to Performance-Based Earthquake Engineering Methods: From Building Code Provisions to Regional Loss Assessment

Thesis directed by Assistant Professor Abbie B. Liel

## **ABSTRACT**

The essence of performance-based earthquake engineering (PBEE) is to design and assess structures to meet specific performance goals, rather than prescriptive requirements. This thesis applies PBEE methods to three problems: (1) evaluating the effectiveness of accidental torsion requirements for seismic design; (2) quantifying spatial correlations of building responses for regional seismic loss assessments; (3) developing and evaluating regional seismic loss assessment methodologies.

(1) Seismic ground motions induce torsional responses in buildings that are difficult to predict. To compensate for this, most modern building codes require the consideration of accidental torsion when computing design earthquake forces. This study evaluates the influence of accidental torsion seismic design requirements on the performance of 230 archetypical buildings, taking collapse capacity as the performance metric. The study concludes that accidental torsion provisions may not be necessary for seismic design of buildings without excessive torsional flexibility or asymmetry.

(2) The possible seismic losses to a portfolio of buildings are of interest for insurance and reinsurance companies, developers, and policy makers. Probabilistic estimates of earthquake-induced losses to portfolios of buildings require quantifying correlations between losses of the different buildings comprising the building stock. This study examines spatial correlations in

building seismic responses. The results demonstrate that correlation patterns in building response parameters are closely linked to correlations in spectral acceleration measured at buildings' first-mode periods. Based on this finding, enhancements are proposed to state-of-the-art methods for regional loss assessment to account for correlations in building response. These building responses provide the basis for computation of earthquake-induced losses in the regional building stock.

(3) This study compares current and developing probabilistic regional (portfolio) loss assessment methods, including those proposed in (2). Of particular interest are: the impact of directly computing losses from building response measures rather than ground motion intensity measures; identifying best practices for predicting collapsed buildings; and examining the sensitivity of loss assessments to other methodological decisions related to building stock classification, exposure, and key sources of uncertainty. On the basis of the identified strengths and weaknesses of the different regional loss assessment techniques, "high-end" and "simplified" methods are recommended for computing probabilistic regional seismic losses.

## **DEDICATION**

God has graciously afforded me the opportunities and resources to excel in structural engineering and has placed just the right people in my life to make it happen. Thank you Jesus!

I dedicate this thesis to my wife, Kristi DeBock. Her patience, encouragement, support, and fantastic attitude are of immeasurable value. She has unselfishly taken my dreams as her own and made countless sacrifices to help us reach them. She constantly seeks ways to make life better and easier, such as making me breakfast in the mornings, and she maintains a joyful heart through all of her hard work. Charm is deceptive and beauty is fleeting, but Kristi is an honorable woman who is worthy of praise, in whom I have full confidence. She is truly a woman of noble character; I am grateful to her and for her. Thank you Kristi!

I am thankful to my advisor, Professor Abbie Liel. Professor Liel has demonstrated unselfish and trusting leadership by providing me with projects that fit my interests and giving me the freedom to take our research “where it goes.” Many of my weaknesses also happen to be her strengths, which has proven to be of significant worth for improving my engineering, research, and writing skills— especially my writing skills! Despite her demanding schedule, she has consistently made herself available and approachable over the past three and a half years. I have learned a lot from Professor Liel, and I will always be proud (and very thankful) that she is my Ph.D. advisor.

Many thanks also to Professor Curt Haselton, for directing me to graduate school in the first place. He saw potential in me that I personally did not see at the time. I thank Professor Haselton for teaching me to do research early in my academic career and introducing me to Professor Liel. I thank him also for our many meaningful conversations, which have ranged from ground motion selection and nonlinear modeling to family, religion, and even politics.

I have also enjoyed the company and research insights of my officemates Siamak Sattar, Meera Raghunandan, Derek Kozak, Cody Harrington, Yolanda Lin, Sarah Welsh-Huggins, Holly Bonstrom, Emily Elwood, Lan Nguyen, and Karim Farokhnia. I also thank Kevin Kim for his work as an undergraduate researcher. Thank you to John Hooper and Jim Harris for involving me in interesting ATC and BSSC projects– I greatly respect them and their contributions to the engineering profession. Thank you to Professors Ross Corotis, Keith Porter, Jack Baker, and Shideh Dashti for their participation as members of my Ph.D. committee. Through classes, office hours, conferences, and even undergraduate research, each of these professors has taught me valuable lessons about research and the engineering profession.

I am also thankful for the support of many family members and friends who have encouraged Kristi and I and who now share in our joy as I finalize my Ph.D. work. Our parents, David and Laurie DeBock and Mark and Kathy Bohlander, have been especially supportive. I thank my sister, Jennifer DeBock, for her many humorous stories and text messages; she always makes me laugh, I admire her, and I am proud to call her my friend. Thank you to Andy Armstrong, Don Wilcox, John Lamb, and Nathan Bowers, who have been role models to me for the past few years. I am also grateful to Nathan Bowers for getting me away from research once in a while to do fun outdoor activities and work/play on the ranch; thanks to him, I will always know that Ph.D. means “Posthole Digger.”

## TABLE OF CONTENTS

<b>1</b>	<b>INTRODUCTION.....</b>	<b>1</b>
<b>2</b>	<b>IMPORTANCE OF SEISMIC DESIGN ACCIDENTAL TORSION REQUIREMENTS FOR BUILDING COLLAPSE CAPACITY .....</b>	<b>6</b>
2.1	Reference Article.....	6
2.2	Introduction .....	7
2.3	Background .....	8
2.4	Methodology .....	9
2.4.1	Archetype Buildings.....	11
2.4.2	Design and Modeling of Archetype Buildings.....	15
2.4.3	Dynamic Analysis of Archetype Building Models .....	24
2.5	Findings.....	26
2.5.1	Definition of Terms.....	26
2.5.2	Trends with the Torsional Irregularity Ratio .....	28
2.5.3	Comparison of Significance of Accidental Torsion Requirements for Ordinary and Special Moment Frames.....	29
2.5.4	Effect of Inherent Torsion.....	32
2.5.5	Trends with Other Building Characteristics.....	34
2.5.6	Verification of Observations by Statistical Analysis .....	36
2.5.7	Additional Parametric Studies.....	38

2.5.8	Limitations .....	40
2.6	Summary and Recommendations .....	42
2.7	Acknowledgements .....	44
<b>3</b>	<b>INCORPORATION OF SPATIAL CORRELATIONS BETWEEN BUILDING RESPONSE PARAMETERS IN REGIONAL SEISMIC LOSS ASSESSMENT.....</b>	<b>45</b>
3.1	Reference Article.....	46
3.2	Introduction .....	46
3.3	Spatial Correlations in Building Responses .....	48
3.3.1	Earthquake Scenarios and Building Simulations .....	49
3.3.2	Computation of Spatial Correlations in Earthquake Scenarios .....	51
3.3.3	Patterns of Spatial Correlations.....	54
3.3.4	Sources of Spatial Correlations.....	58
3.4	Including Correlations in Building Responses in Regional seismic Loss Assessment.....	60
3.4.1	Regional Seismic Loss Assessment Methods .....	60
3.4.2	Simulating EDPs as Spatially Correlated Fields .....	62
3.4.3	Importance of the IM-EDP Transformations .....	66
3.4.4	Variability in Transformation Between IMs and EDPs .....	67
3.4.5	Adaptation of the Methodology to Include Collapsed Buildings, Multiple EDPs and Multiple Building Types .....	75
3.4.6	Relation to Steps in Regional Loss Assessment Method.....	77

3.5	Conclusions .....	78
3.6	Data and Resources .....	79
3.7	Acknowledgments.....	79
<b>4</b>	<b>A COMPARATIVE EVALUATION OF PROBABILISTIC REGIONAL SEISMIC LOSS ASSESSMENT METHODS, USING SCENARIO CASE STUDIES.....</b>	<b>81</b>
4.1	Reference Article.....	81
4.2	Introduction .....	81
4.3	Overview of Regional Seismic Loss Assessments.....	84
4.3.1	Earthquake Scenarios.....	84
4.3.2	Building Stocks and Test Regions .....	85
4.3.3	Building Representations, Structural Analyses and Loss Assessments.....	88
4.4	Candidate Regional Loss Assessment Methods.....	94
4.4.1	Developing Regional Ground Motion Intensity Maps.....	94
4.4.2	Predicting Building Responses (IDRs) at Each Site .....	98
4.4.3	Computing Losses in Individual Buildings.....	100
4.5	Comparison of Regional Loss Assessment Methods .....	102
4.5.1	Overview .....	102
4.5.2	Comparisons of IM-based and EDP-based Methods for Non-Collapsed Buildings..	104
4.5.3	Comparisons of Methods to Identify Collapsed Buildings .....	108

4.5.4 Sensitivity of Predicted Regional Loss Distributions to Other Methodological Choices	112
4.5.5 Recommended Methods for Computing Regional Building Loss .....	119
4.6 Conclusions .....	123
4.7 Acknowledgments .....	126
<b>5 SUMMARY AND CONCLUSIONS.....</b>	<b>127</b>
5.1 Building Code Development: Accidental Torsion Seismic Design Requirements.....	128
5.1.1 Summary and Implications .....	128
5.1.2 Limitations .....	130
5.1.3 Future Work .....	132
5.2 Regional (Portfolio) Seismic Loss Assessment .....	133
5.2.1 Incorporation of Spatial Correlations Between Building Response Parameters in Regional Seismic Loss Assessment: Summary and Implications.....	133
5.2.2 A Comparative Evaluation Probabilistic Regional Seismic Loss Assessment Methods, Using Scenario Case Studies: Summary and Implications .....	134
5.2.3 Sample Regional Seismic Risk Assessment: Summary and Implications .....	135
5.2.4 Limitations .....	136
5.2.5 Future Work .....	142
<b>6 Appendix: Documentation of Regional (Portfolio) Seismic Risk Analysis .....</b>	<b>143</b>
6.1 Overview .....	143

6.2	Application Software and Organization .....	143
6.3	Define a Region and Building Stock.....	144
6.4	Generating Fault Rupture Scenarios .....	146
6.4.1	Fault Properties .....	146
6.4.2	Sampling Earthquakes for Each Fault.....	146
6.4.3	Matching the 2009 USGS Regional Magnitude-Recurrence.....	149
6.4.4	An Alternative Approach for Generating Random Fault Rupture Scenarios .....	151
6.5	Generating Ground Motion Intensity Maps .....	151
6.5.1	Compute Expected $S_a$ at Each Site from a GMPE .....	152
6.5.2	Generate Residuals and Build the Intensity Maps .....	153
6.5.3	Summary and Validation of Resulting Intensity Maps .....	155
6.6	K-means Clustering of Intensity Maps.....	157
6.6.1	General Description of k-means Clustering.....	158
6.6.2	Clustering Intensity Maps .....	158
6.7	Computing Regional Losses.....	162
6.7.1	Overview .....	162
6.7.2	Computing Losses for Collapsed Buildings.....	162
6.7.3	Computing Losses for Non-Collapsed Buildings .....	163
6.7.4	Computing Regional Losses .....	164
6.8	Compiling the Probabilistic Regional Loss Results .....	164

6.8.1 MRE for Regional Loss ..... 165

6.8.2 Dissecting the MRE Results..... 166

6.9 Summary ..... 171

**7 REFERENCES ..... 173**

**LIST OF TABLES**

Table 2.1 Matrix of 2D Frame Designs for RC OMFs and RC SMFs .....	17
Table 3.1. Earthquake events used in nonlinear time-history analyses. ....	49
Table 3.2. Building models used in nonlinear time-history analyses. ....	50
Table 4.3. Model buildings representing the class of RC moment frames. ....	90
Table 4.4. Collapse capacities of model buildings. ....	93
Table 4.5. Summary of methods compared for different steps in the loss assessment. ....	97
Table 7.1 Summary of Model Buildings Representing Each Structural Class. ....	145
Table 7.2. Annualized Costs by Structural Class.....	171

## LIST OF FIGURES

Figure 2.1	Flow chart of the FEMA P-695 methodology for assessing collapse risk, as adapted for this study. ....	11
Figure 2.2	Plan view of archetype buildings with (a) rectangular frame layouts, (b) I-shape frame layouts, and (c) inherent torsion (offset rectangular) frame layouts.....	15
Figure 2.3	Procedure for calibrating a simplified model to a high-end model of a 2D RC frame. ....	19
Figure 2.4	Illustration of a simplified model of a 2D RC frame.....	20
Figure 2.5	Typical 3D model plan view. ....	21
Figure 2.6	Sample interpolation of nonlinear brace properties for a simplified 2D model. ....	22
Figure 2.7	Illustration of calculation of (a) <i>significance</i> of design accidental torsion requirements and (b) <i>need</i> for design accidental torsion requirements for the four-story low gravity SMF archetype, having a rectangular frame layout and $TIR = 1.5$ .....	27
Figure 2.8	<i>Significance</i> of accidental torsion design requirements for (a) OMF archetypes (SDC B) and (b) SMF archetypes (SDC D). The dashed vertical lines represent ASCE/SEI 7-defined thresholds classifying a building as having horizontal irregularity Type 1a ( $TIR = 1.2$ ) and Type 1b ( $TIR = 1.4$ ). ....	28
Figure 2.9	Collapse capacities for (a) OMF archetypes (SDC B) and (b) SMF archetypes (SDC D). Results are for simulated collapse modes only and analyses with model accidental torsion corresponding to a 5% offset of the center of mass.....	29
Figure 2.10	(a) Comparison of ACMR for the four-story SMF archetype buildings. Results from low gravity archetypes are plotted with blue lines and triangular markers; results from	

high gravity archetypes are plotted with red lines and square markers. (b) Ultimate pushover capacities (normalized) of four-story low gravity SMF archetypes.....	32
Figure 2.11 Binary regression tree for predicting the <i>significance</i> (denoted “Sig”) of design accidental torsion requirements from building characteristics. ....	37
Figure 2.12 (a) Trends in <i>Need</i> with respect to <i>TIR</i> for variations of the four-story low gravity SMF archetype with different torsional periods and frame layouts; (b) Trends in <i>Need</i> with respect to relative frame spacing ( <i>S/L</i> ) for the same four-story archetype, with rectangular and square frame layouts; (c) Comparison of <i>TIR</i> vs. relative frame spacing ( <i>S/L</i> ) for three different frame layouts. ....	40
Figure 3.1. Building 1 vs. Building 1 responses, quantified by $\text{Ln}[IDR]$ , for the Chi Chi earthquake at sites with inter-site distances of $\Delta d$ . ....	52
Figure 3.2. Spatial correlations of $IM = \text{Ln}[Sa(T_I=0.60 s)]$ computed for the Chi Chi earthquake through four different methods, the details of which are described in the text. All of the correlations shown are in terms of <i>absolute</i> rather than <i>residual IM</i> quantities. ....	53
Figure 3.3. Correlations of $\text{Ln}[IDR]$ for Building 1 and Building <i>j</i> (denoted 1, <i>j</i> ) for the Chi Chi earthquake. ....	55
Figure 3.4. Self-correlations of $\text{Ln}[IDR]$ for Building 1 for the four different earthquake scenarios.....	57
Figure 3.5. Map of ground motion intensities (“Intensity map”), quantified by $Sa(T_I=0.6 s)$ and $\text{Ln}[Sa(T_I=0.6 s)]$ , for the ShakeOut and Northridge earthquakes. Areas with high ground motion intensity are circled.....	58
Figure 3.6. Spatial correlations between ground motion intensity measures ( $\text{Ln}[Sa(T_I)]$ ) and building response parameters ( $\text{Ln}[IDR]$ , $\text{Ln}[PFA]$ , $\text{Ln}[BPHR]$ and $\text{Ln}[CPHR]$ ) in the	

Northridge earthquake for: (a) self-correlations for Building 1 and (b) cross-correlations between Buildings 1 and 6, and in the Shakeout earthquake for: (c) self-correlations for Building 1 and (d) cross-correlations between Buildings 1 and 6. .... 59

Figure 3.7. Weighted least-squares linear regression of  $Ln[IDR]$  with  $Ln[Sa(T_1)]$ , based on nonlinear analysis results from building models subjected to the Northridge ground motions for: (a) Building 1 and (b) Building 6 (non-collapse cases only). The standard error interval defines the range in which 68% of the  $EDP$  values are expected to fall (*i.e.*  $\pm 1$  standard deviation)..... 63

Figure 3.8. Intensity and  $EDP$  maps for the Northridge earthquake showing (a)  $Ln[Sa(T_1)]$  (units  $Ln[g]$ ), (b)  $Ln[IDR]$  for Building 6 as predicted from the fitted linear  $IM-EDP$  transformation, (c)  $Ln[IDR]$  as observed in nonlinear time-history analysis of Building 6, and (d) the residual differences between the predicted and observed  $Ln[IDR]$  values, *i.e.*  $Ln[IDR]_{pred} - Ln[IDR]_{obs}$ . .... 65

Figure 3.9. Spatial autocorrelations of the standardized residual differences between the predicted and observed  $Ln[EDP]$  values ( $Ln[EDP]_{pred} - Ln[EDP]_{obs}$ ) using the Northridge results for (a) Building 1 and (b) Building 6..... 66

Figure 3.10. (a)  $IDA$  results in terms of  $IDR$  vs.  $Sa(T_1)$  for Building 6, and (b) the same results recast as  $Ln[IDR]$  vs.  $Ln[Sa(T_1)]$ , showing the fitted  $IM-EDP$  transformations for each record as compared to the Northridge  $IM-EDP$  transformation. .... 69

Figure 3.11. Observed and sampled intercept and slope coefficients of  $IM-EDP$  relationships for Building 6..... 70

Figure 3.12. Acceleration spectra for two records, both with  $Sa(T_1=1.0 s)=1.0g$ ..... 72

Figure 3.13. Scatterplots of slope and intercept coefficients (defining <i>IM-EDP</i> transformations) vs. $\varepsilon$ for Building 6 with correlation coefficients and best-fit lines displayed on the plots. The slopes of the best-fit lines (m) are discussed in a later section.....	72
Figure 4.1. Illustration of probabilistic methods for regional loss assessment. Aspects examined in this study are outlined by the gray dashed box.....	83
Figure 4.2. Small and large regions considered in and around Los Angeles. (Background map from <a href="http://www.findlatitudeandlongitude.com">www.findlatitudeandlongitude.com</a> ).....	86
Figure 4.3. Distribution of RC frame building stock for downtown Los Angeles (small region) by height, occupancy and year of construction.....	87
Figure 4.4. Map of building locations generated for the downtown Los Angeles building stock (small region). Building sizes are shown for illustration, but exaggerated. ....	88
Figure 4.5. Regions considered in Taiwan, together with the approximate fault rupture location (red line) for the Chi Chi earthquake in Taiwan from (Rubin <i>et al.</i> 2001). (Background map from <a href="http://www.findlatitudeandlongitude.com">www.findlatitudeandlongitude.com</a> ).....	89
Figure 4.6. IDA for model building no. 4 computed with the FEMA (2009) far-field ground motions, showing non-collapse structural analysis results, which are inputted into PACT, and the collapse capacity distribution. ....	91
Figure 4.7. Vulnerability functions (VF) for non-collapsed buildings, for structures represented by model building no. 3, with commercial occupancy showing: (a) <i>IDR</i> -based vulnerability function; (b) <i>S<sub>a</sub></i> -based vulnerability function; and (c) <i>S<sub>a</sub>-<math>\varepsilon</math></i> -based vulnerability function. For reference, the median replacement cost of this building is estimated at \$162/ft <sup>2</sup> . ....	92

- Figure 4.8. Illustration of  $Sa$ - $IDR$  transformations showing (a)  $Sa$ - $IDR$  transformations for model building no. 4 obtained from IDA for a general set of ground motions (FEMA 2009) and from the ShakeOut and Chi Chi earthquakes and (b) distribution of  $A_h$  and  $B_h$  coefficients describing the  $Sa$ - $IDR$  transformations that are depicted in (a), with contours representing probability densities of the multivariate normal distribution..... 100
- Figure 4.9. Distributions predicted for  $[RL/TH]$  for the ShakeOut large region and sparse building stock, comparing  $IDR$ -based and  $Sa$ -based methods for loss for all buildings represented by (a) model building no. 1 (28 buildings) and (b) model building no. 2 (16 buildings). ..... 105
- Figure 4.10. Distributions predicted for  $[RL/M,R]$  for the Chi Chi large region 2 and sparse building stock, comparing four  $Sa$ -based methods to an  $IDR$ -based method. .... 107
- Figure 4.11. (a) Distributions predicted for  $[RL/TH]$  for the Chi Chi large region 2 and buildings represented by model building no. 5 in the sparse building stock, comparing methods for identifying which buildings have collapsed, and showing (b) fraction of collapsed buildings computed by the different methods. The annotation of  $Sa$ ,  $\varepsilon$  and  $IDR$  describes the input for determining collapse. .... 110
- Figure 4.12. Fractions of buildings collapsed for the ShakeOut large region and dense building stock, comparing collapse classification methods that consider  $Sa$  vs.  $Sa$ - $\varepsilon$  and those that generate region-wide vs. site-by-site collapse capacities. .... 111
- Figure 4.13. Distributions predicted for  $[RL/M,R]$  for the ShakeOut small region and sparse building stock (18 buildings), comparing methods that incorporate probabilistic and deterministic techniques for computing individual building losses. Losses are computed by G3-E0-V4-C3..... 114

Figure 4.14. Distributions predicted for $[RL/M,R]$ for the Chi Chi large region 1 for sparse building stocks with the same buildings, but different spatial distributions. Losses are computed by G3-E0-V4-C3.....	115
Figure 4.15. Distributions predicted for $[RL/M,R]$ for the ShakeOut small region and dense building stock, examining building height and capacity misclassifications. Losses are computed by G3-E0-V4-C3.....	118
Figure 4.16. Distributions predicted for $[RL/M,R]$ , comparing Simplified and High-end methods for the ShakeOut small region and dense building stock.....	121
Figure 4.17. Distributions predicted for $[RL/M,R]$ , comparing Simplified <sub>3</sub> to the High-end and Simplified <sub>1</sub> methods for buildings for loss from all buildings represented by model building no. 2 in the Chi Chi large area 2 and sparse building stock. ....	123
Figure 7.1 Test region location for the building stock (inventory) example that is considered throughout this chapter. ....	144
Figure 7.2 Map of building locations for the building stock that is analyzed in this example. Building sizes are represented graphically, but differences in size are exaggerated. ....	145
Figure 7.3 Map showing region of interest (red rectangle) and all documented faults within a 200 km (124 mile) radius in Southern California. ....	147
Figure 7.4 Frequency density function for earthquake magnitudes on a selected fault. Partitions are constructed to preferentially sample large magnitudes. ....	148
Figure 7.5 Magnitude-recurrence relationship for the test region, considering only fault ruptures within 200 km (124 miles). Consider adding the other curve for the thesis. ....	150
Figure 7.6 Correlation of residuals as a function of distance for $Sa(T_I=1.0\ sec)$ , computed with the Loth and Baker (2013) spatial correlation model. ....	155

Figure 7.7	Comparison of site hazard with OpenSHA (2013) and the MCS analysis. For this example, the magnitude recurrence is adjusted to match the 2002 USGS mag recurrence, since the 2009 USGS model is not available in OpenSHA. ....	157
Figure 7.8	k-means clustering example. Random data pairs $(X_i, Y_i)$ (a) are grouped into three clusters (b).....	159
Figure 7.9	Sample of intensity maps from three clusters denoted i, j, and k, where maps ‘A’ and ‘B’ are randomly sampled from the group of maps belonging to a given cluster. For this illustration, $S_a$ is $S_a(T_I=0.91 \text{ sec})$ . ....	161
Figure 7.10	Example vulnerability function for structural class 6 (8-story nonductile RC frames), with commercial occupancy. ....	164
Figure 7.11	MRE for the sample building stock for different levels of regional loss. ....	165
Figure 7.12	Deaggregation of costs to show the portions of the loss due to costs for collapsed buildings versus non-collapsed buildings. ....	167
Figure 7.13	“Smooth” Deaggregation of costs to show the portions of the loss that are due to costs for collapsed buildings versus non-collapsed buildings. ....	167
Figure 7.14	Deaggregation of costs to show the portions of the loss that are due to costs for the different structural classes.....	168
Figure 7.15	MRE plot for each structural class, normalized by the cost to replace all of the buildings in the structural class.....	169
Figure 7.16	Visual breakdown of (a) annualized costs and (b) percentage of gross building area by structural class ID.....	171

# 1 INTRODUCTION

This thesis aims to use performance-based earthquake engineering (PBEE) methods to improve the practice and art of earthquake engineering of building structures. The essence of PBEE is to design and build structures that meet the needs and desires of building owners, users, and society. PBEE requires the analyst to quantify seismic demands and building capacities probabilistically, in order to make risk-informed decisions. This thesis applies PBEE to two main areas: (1) making recommendations for building code improvements, in particular focusing on accidental torsion design provisions for buildings, and (2) enhancing tools for probabilistic regional seismic loss assessment. The overall approach to each of these problems is similar. The problem at hand is analyzed with advanced modeling and simulation techniques. Based on the results of robust analyses, simplified methods by which these same problems can be addressed are proposed. The goal of the proposed simplified methods is to require less effort on the part of the analyst, while, at the same time, ensuring a high level of confidence in the end result.

This thesis represents a compilation of articles, each of which relies on PBEE methods to improve building code provisions or methods of seismic loss assessment for communities of buildings. Each of these chapters is a self-contained work, having its own abstract, terminology, methodology, and conclusions. Conclusions and limitations from all of the chapters are recapped in the Summary and Conclusions chapter at the end of this thesis.

Chapter 2, which is based on DeBock et al. (2013), evaluates the importance of seismic accidental torsion design provisions in modern building codes, focusing specifically on ASCE/SEI 7, using collapse capacity as the metric of building performance. In this study, a methodology that was originally developed by the FEMA P-695 project to evaluate the

performance of a class of buildings all having the same seismic lateral force resisting system is adapted to evaluate the collapse performance of buildings designed with and without accidental torsion design requirements for seismic-lateral-force-resisting systems with varying ductility. Results show that the designs that account for ASCE/SEI 7 accidental torsion provisions lead to significant improvements in collapse capacity for buildings that are highly torsionally flexible or asymmetric. However, only inconsequential changes in collapse capacity are observed in the buildings that are both torsionally stiff and regular in plan. Therefore, the study concludes that accidental torsion provisions can be safely omitted from seismic design provisions for buildings without torsional irregularities, which can stem from torsional flexibility or asymmetry. This simplification can reduce designers' effort for buildings in which accidental torsion will not be important.

The rest of the thesis investigates and develops improvements to performance-based earthquake engineering methods for regional seismic loss assessment. The article that makes up Chapter 3, DeBock *et al.* (2014a), focuses on quantifying spatial correlations in building response and implementing a method by which these correlations can be incorporated in a regional loss estimation methodology. Previous research has shown that spatial correlations in ground shaking intensity are important for predicting the distribution of future losses for a geographically distributed stock of buildings. The study shows that buildings located close to each other have highly correlated responses to earthquake shaking; the level of correlation decreases as the building's separation distance increases, mostly because the correlation in ground motion intensity also decreases with distance. Seismic responses of similar buildings (with similar periods and/or ductility capacities) are more correlated than for dissimilar

buildings, and large magnitude earthquakes result in positively correlated building responses at greater distances than smaller earthquakes.

A critical observation is that spatial correlations between engineering demand parameters (*i.e.* *EDPs*, particularly interstory drift) and spectral accelerations at a building's fundamental period ( $Sa(T_1)$ ) exhibit very similar patterns. Building on these findings, a method is proposed for incorporating correlations in building response in state-of-the-art methods for regional seismic loss assessment. In the proposed method, spatially distributed ground motion intensities (*i.e.*  $Sa(T_1)$ ) are generated with existing models. These "intensity maps" are converted to spatial distributions of "*EDP* maps" through transformations that linearly relate ground motion intensity and building response in log space, so-called "*IM-EDP* transformations". The transformations produce unbiased predictions of building responses that capture the expected spatial correlation structure of *EDPs*. The coefficients needed to define such linear transformations are obtained by a priori performing incremental dynamic analysis (IDA) on nonlinear models representing each building type of interest. The range of *IM-EDP* relationships obtained by performing IDA analysis with a suite of earthquake ground motion records is strongly tied to the variability of the ground motion records' spectral shapes. A related observation is that the range of potential *IM-EDP* relationships that we would expect to occur on average throughout a region from the same event is less variable than the *IM-EDP* relationships observed from record to record in different events. Therefore, the distribution of probable *IM-EDP* relationships that is obtained from IDA is modified to estimate the distribution of probable *IM-EDP* transformations for a region by shifting its mean and reducing its variance to account for the spectral shape of the ground motion records that are used for IDA analysis. The *EDP* maps then provide the basis for loss prediction in each building in the portfolio/region.

The proposed enhancement to regional loss assessment methods represents the first time correlations in building responses, in addition to ground motion intensities, are explicitly considered. Since *EDPs* are better predictors of damage/loss than  $Sa(T_1)$ , such a process is expected to improve methods for estimating total losses for building stocks that are distributed throughout a region.

Chapter 4, which is based on DeBock *et al.* (2014b), describes several case-study analyses that are performed in order to compare various regional seismic loss assessment methods on the basis of how well they estimate the median and range of regional seismic losses, given an event, and how difficult they are to execute. The study is performed on multiple stocks of ductile and nonductile RC moment frame buildings. A “high-end” method is identified, which is considered the most robust regional loss assessment method. Furthermore, the article identifies simplified methods that produce distributions of regional losses that are similar to the high-end method. Additional factors affecting regional losses are also explored. The study concludes that the most important factors to consider in probabilistic regional seismic loss assessments are: (1) spatial correlations of ground motion intensity; (2) regional versus site-to-site methods for collapse classification; (3) accurate characterization of building capacity, especially strength and ductility; and (4) spatial clustering of buildings if such clusters exist in the inventory.

Documentation of a Matlab tool for regional seismic loss assessment, accompanied by an example application, is provided as an appendix to this thesis. The purpose of the appendix is two-fold: (1) To provide detailed enough documentation of the regional loss assessment tool to enable analysts to use it with a sufficient level of understanding, expand its applicability to other regions or buildings, or even to recreate their own version of the regional loss assessment tool; (2) To show an example of how the regional loss assessment tool may be used to analyze seismic

risks to communities of buildings in a way that informs decision makers about where to focus their efforts for improving community (or portfolio) resilience to earthquakes.

## 2 IMPORTANCE OF SEISMIC DESIGN ACCIDENTAL TORSION REQUIREMENTS FOR BUILDING COLLAPSE CAPACITY

**ABSTRACT:** Seismic ground motions induce torsional responses in buildings that can be difficult to predict. To compensate for this, most modern building codes require the consideration of accidental torsion when computing design earthquake forces. This study evaluates the influence of ASCE/SEI 7 accidental torsion seismic design requirements on the performance of 230 archetypical buildings that are designed with and without accidental torsion design provisions, taking building collapse capacity as the performance metric. The test-case archetypes include a broad range of heights, gravity load levels, and plan configurations. Results show that the ASCE/SEI 7 accidental torsion provisions lead to significant changes in collapse capacity for buildings that are very torsionally flexible or asymmetric. However, only inconsequential changes in collapse capacity are observed in the buildings that are both torsionally stiff and regular in plan. Therefore, the study concludes that accidental torsion provisions are not necessary for seismic design of buildings without excessive torsional flexibility or asymmetry.

### 2.1 Reference Article

DeBock, D.J., A.B. Liel, C.B. Haselton, J.D. Hooper, and R.A. Henige Jr. (2013), "Importance of seismic design accidental torsion requirements for building collapse capacity." *Earthquake Engineering and Structural Dynamics*. In Press.

## 2.2 Introduction

During an earthquake, torsional deformations in buildings can result from a variety of sources. Here, sources of torsional behavior are separated into two categories: ‘inherent torsion’ and ‘accidental torsion’. Predictable sources, such as asymmetric building geometry, are classified as ‘inherent torsion’. Other sources, such as unaccounted for stiffness contributions from the gravity system or nonstructural components, uneven live load distribution, stiffness degradation of parts of the lateral system, and varying ground motion intensity across the plan of a building, are classified as ‘accidental torsion’ (De la Llera and Chopra 1995). Many building codes, such as ASCE/SEI 7, the Eurocode, the National Building Code of Canada, the New Zealand Standard, and the Model Building Code of Mexico, impose accidental torsion design requirements for buildings with rigid diaphragms (ASCE 2010, Eurocode 8 2004, NRCC 2010, NZS 2004, MOC 2008). These provisions require the designer to introduce an accidental eccentricity ( $e_a$ ) that offsets the line of action for design lateral shear forces,  $V$ , from the center of mass by a fraction ( $\beta$ ) of the building’s plan dimension ( $L$ ) in the direction that is most critical for the design of a seismic force resisting element, *i.e.*  $e_a = \pm \beta L$  (ASCE 2010, Eurocode 8 2004, NRCC 2010, NZS 2004, MOC 2008). Typical values of  $\beta$  are on the order of 0.05 or 0.1; in ASCE/SEI 7,  $\beta = 0.05$  (ASCE 2010). Accidental torsion moments ( $M_{ta}$ ) are computed as  $M_{ta} = Ve_a$ . These moments are resisted by increasing the design lateral shear forces in the lateral resisting system.

This study quantifies the effect of these building code accidental torsion design requirements on building collapse capacity. To this end, approximately 460 three-dimensional (3D) building models are analyzed, representing 230 archetype buildings, each designed with and without accidental torsion requirements, according to the ASCE/SEI 7-10 design provisions. These

analyses are used to evaluate the effectiveness of accidental torsion provisions, as currently implemented in modern codes like in ASCE/SEI 7, in preventing earthquake-induced collapse.

### 2.3 Background

Past research on accidental and inherent torsion in buildings has reached varying conclusions (Anagnostopoulos *et al.* 2010, De Stefano and Pintucchi 2008). Key findings from previous studies are outlined in this section and are organized by the type of simulation model used, as the modeling approach has a bearing on the findings. Three main categories of simulation models have been used to study earthquake-induced torsional response in buildings: (1) linear models, (2) simplified single-story shear-spring models and (3) lumped plasticity nonlinear frame models. For a more detailed literature review, see (De Stefano and Pintucchi 2008).

Early studies of accidental torsion utilized linear models that were capable of representing realistic complex building geometries, but not post-yielding behavior and collapse. Results from linear models have shown that design accidental torsion provisions do not significantly impact building performance under earthquake excitation for many nominally symmetric buildings. However, such provisions may be important for buildings whose torsional periods are either very close to or much larger than their lateral periods (De la Llera and Chopra 1992). Linear models have also been used to develop improved design procedures for dealing with accidental torsion. For example, De la Llera and Chopra (1992) proposed that accidental torsion be dealt with by increasing design forces with amplification factors that are related to the ratio of a building's fundamental torsional and lateral periods of vibration. Such recommendations are outside the scope of our study, as we are concerned with the importance of existing accidental torsion design requirements.

Some of the first nonlinear models used for studying torsion in buildings aggregated the behavior of lateral force resisting systems in single-story bilinear shear-spring models. Both Tso and Smith (1999) and Anagnostopolulos *et al.* (2010) showed that the effects of torsion predicted by such models vary substantially depending on the procedure used to calibrate them. Particularly important is the treatment of the relationship between strength and stiffness when the modeled strength of the simplified model is increased to account for design accidental torsion. Anagnostopolulos *et al.* (2010) found that while shear-spring models calibrated to pushover analysis provided reasonable results (in comparison to multi-degree-of-freedom nonlinear models), those that increase strength independently of stiffness provided inaccurate results that showed qualitatively opposite trends compared to the more complicated models, which were physically unrealistic.

Recent research employed nonlinear frame models to investigate accidental torsion provisions. Stathopoulos and Anagnostopoulos (2010) used one, three and five-story reinforced concrete (RC) space frames with lumped plasticity models of beam and column elements to assess the importance of design accidental torsion, showing that the inclusion of accidental torsion in design does not significantly improve the seismic performance of these buildings. Chang *et al.* (2009) examined six and twenty-story steel space frames and reached the same conclusion. Both of these studies used ductility demand of the beam-column plastic hinges as the primary measure of building performance.

## 2.4 Methodology

The primary goals of seismic provisions in modern building codes are to prevent building collapse and to preserve life safety (BSSC 2009). Therefore, this study evaluates the importance of the ASCE/SEI 7 accidental torsion design requirements by quantifying how these

requirements influence building collapse capacity or collapse risk. To evaluate building collapse capacity, the study employs an adaptation of the FEMA P-695 methodology (FEMA 2009). FEMA P-695 was developed to evaluate seismic design provisions through nonlinear dynamic analysis. FEMA P-695's original intent was for use in determining appropriate building response coefficients (such as the  $R$ -factor in ASCE/SEI 7) for newly proposed lateral systems, in order to ensure that code-permitted seismic-lateral-force-resisting systems have an acceptably low probability of collapse (FEMA 2009). The method requires that a user evaluate a proposed seismic-lateral-force-resisting system by: (1) designing a set of archetype buildings that represent the range of possible features that are expected in the building set of interest (*e.g.* height, gravity load, *etc.*); (2) creating simulation models of the archetype buildings; (3) evaluating the collapse capacities of the building simulation models through nonlinear dynamic analysis; and (4) showing that collapse capacities exceed acceptable levels. In this study, FEMA P-695 methods are adapted to evaluate the collapse performance of buildings designed with and without accidental torsion design requirements for all types of seismic-lateral-force-resisting systems, as shown in Figure 2.1. Differences in collapse capacity of archetype buildings designed with and without accidental torsion serve to quantify the importance of including accidental torsion requirements in code seismic provisions. Although we use FEMA P-695 procedures here, in concept, any systematic method for evaluating collapse capacity could be employed to quantify differences in buildings designed with and without accidental torsion provisions based on a design accidental eccentricity.

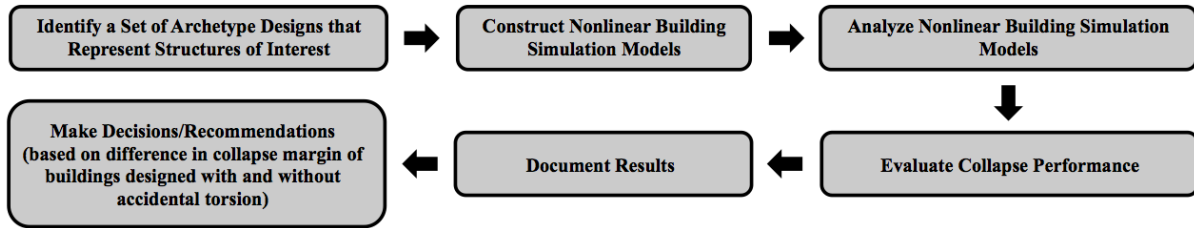


Figure 2.1 Flow chart of the FEMA P-695 methodology for assessing collapse risk, as adapted for this study.

## 2.4.1 Archetype Buildings

ASCE/SEI 7 accidental torsion provisions apply to all types of buildings with rigid floor and roof diaphragms. To systematically evaluate these provisions, a suite of building archetypes is developed to represent a wide variety of structural properties and reflect variation in design characteristics that might affect torsional behavior. The archetype buildings vary in terms of: (1) seismic-lateral-force-resisting system, (2) number of stories, (3) weight/gravity load level, and (4) plan layout. Two versions of each building are designed: one with and one without design accidental torsion force demands.

### 2.4.1.1 Seismic-Lateral-Force-Resisting System

The study is performed in two phases. Phase 1 focuses on buildings in low-seismic regions and analyzes RC Ordinary Moment Frame (OMF) building designs and models. The RC OMFs are designed according to ACI 318-05 (ACI 2005) and ASCE/SEI 7-10 (ASCE 2010) for Seismic Design Category (SDC) B. SDC B encompasses moderate seismic regions in the U.S. By definition, SDC B buildings are those that have design spectral acceleration values of  $0.167 \leq S_{DS} < 0.33 g$  and  $0.067 \leq S_{DI} < 0.133 g$ ; here,  $S_{DS}$  and  $S_{DI}$  are the code-defined design spectral acceleration values at 0.2 second and 1.0 second periods, respectively. Phase 2 focuses on buildings in high-seismic regions, employing RC Special Moment Frame (SMF) designs and models. The RC SMFs are also designed according to ACI 318-05 (ACI 2005) and ASCE/SEI 7-

10 (ASCE 2010), but for Seismic Design Category D. SDC D includes high seismic areas and is defined by design spectral acceleration values  $S_{DS} \geq 0.5 g$  and  $S_{DI} \geq 0.2 g$ . SMFs must satisfy a large number of additional capacity design and detailing requirements.

To make the analysis tractable, these two sets of RC frames are used to represent the building stock more generally. The analysis uses RC frames because their nonlinear behavior is fairly well documented for modeling collapse (Haselton *et al.* 2008, Haselton *et al.* 2011, Liel *et al.* 2011), and they are a common form of building construction. In addition, the most important properties pertaining to collapse capacity, *i.e.* overstrength and deformation capacity, are similar to those of other lateral systems commonly used in areas with similar levels of seismicity. Since the study emphasizes relative comparisons of collapse capacity associated with accidental torsion, the focus solely on RC frames is not expected to bias results.

#### 2.4.1.2 *Building Height*

The archetype buildings have one, four, or ten stories. Past studies have suggested that accidental torsion requirements are less beneficial for taller buildings (five to twenty stories) than single-story buildings (Chang *et al.* 2009, Stathopoulos and Anagnostopoulos 2010). The tallest (10-story) archetype structures are flexible enough to observe higher mode effects.

#### 2.4.1.3 *Gravity Load*

Past research has shown that gravity load levels can significantly affect structural ductility, overstrength, and collapse performance (FEMA 2009, Haselton *et al.* 2011, Liel *et al.* 2011). Therefore, ‘low’ (100 psf) and ‘high’ (200 psf) dead loads<sup>1</sup> are used to design and model the archetype buildings to interrogate the relationship between gravity loading and the importance of

---

<sup>1</sup> Roof diaphragms are often more slender than floor diaphragms, so lower dead loads are used at the roof: 80 psf for ‘low’ gravity designs and 160 psf for ‘high’ gravity designs.

design accidental torsion. Live loads in all cases are assumed to be 20 psf at the roof level and 50 psf at all other floor levels. An additional 15 psf is taken for partition loading.

#### 2.4.1.4 *Building Plan and Frame Layout*

The archetype buildings have rectangular plan dimensions of 100 ft. by 200 ft., with one or two frame lines resisting lateral loads in each orthogonal direction. In design, the center of mass is taken at the center of the plan. The archetype buildings have three different plan layouts of lateral force resisting frames, as shown in Figure 2.2: (1) a symmetric rectangular layout (hereafter called the “rectangular” layout), (2) an I-shape layout, and (3) an offset rectangular layout (referred to hereafter as the “inherent torsion” layout). Only the archetype buildings with the offset rectangular layout have inherent torsion. For each of these groups, the torsional stiffness of the archetype buildings is varied by adjusting the spacing of the lateral force resisting frames ( $S$ ) relative to the building plan dimensions ( $L$ ).

The majority of the archetypes (comprising approximately 80% of the total number of buildings analyzed) use the rectangular layout pictured in Figure 2.2(a). By varying the torsional stiffness of these archetype buildings through adjustment of their frame spacing, they can be used to represent a wide range of symmetric buildings, including both perimeter and space frame systems. Many other buildings, such as parking garage structures, have an I-shape layout like that shown in Figure 2.2(b). In these buildings, torsional motion is resisted primarily by the frames in one orthogonal direction (those oriented along the  $y$ -axis). The impact of the I-shape frame layout on the importance of accidental torsion is investigated through a subset (8%) of the archetype design space. Another subset (12%) of asymmetric one-story archetypes is also

investigated, using the inherent torsion frame layout.<sup>2</sup> Past research showed that accidental torsion requirements are more critical for symmetric buildings, because the requirements lead to larger relative increases in design lateral forces in these structures (De la Llera and Chopra 1995, Stathopoulos and Anagnostopoulos 2010). These findings can be examined through comparison of the asymmetric (inherent torsion layout) and symmetric (rectangular and I-shape layout) archetype buildings.

The FEMA P-695 methodology requires that an archetype design space be comprehensive enough to include a full range of possible building configurations. However, designs whose collapse trends do not control the seismic performance assessment, in our case corresponding to those that do not impact the analysis of the importance of ASCE/SEI design accidental torsion requirements, are excluded from the archetype design space. Consequently, the overall size of the archetype design space is reduced significantly, based on a set of preliminary analyses, resulting in the majority of the archetype buildings having the rectangular frame layout and many having one-story, without compromising the generalizability of our findings.

Torsional stiffness and asymmetry are important building characteristics from the perspective of accidental torsion. Torsionally-flexible archetypes have closely spaced frame lines (small  $S/L$ ), whereas torsionally-stiff models have widely spaced frame lines (large  $S/L$ ).<sup>3</sup> In this study, the torsional characteristics of the archetype buildings are quantified by the torsional irregularity ratio ( $TIR$ ), which is defined in Table 12.3-1 of ASCE/SEI 7 as the ratio of “maximum story

---

<sup>2</sup> Inherent torsion could also be represented by shifting the design center of mass, rather than the location of the frames (*i.e.*, center of stiffness), but it is expected that this approach would result in similar changes in both building design and seismic performance.

<sup>3</sup> For clarity, we note that our concept of torsional stiffness is based on a relative comparison between torsional and lateral periods. A torsionally-stiff building with large  $S/L$  has a fundamental torsional period that is significantly shorter than its fundamental lateral period, whereas a torsionally flexible building with small  $S/L$  has a longer torsional than lateral period.

drift, computed including accidental torsion ... at one end of the structure” to “the average of the story drifts at the two ends of the structure”, where both drifts are computed in the same direction of interest (ASCE 2010). According to this definition, a building with inherent torsion has a larger *TIR*, because the building will rotate under the applied lateral loads at the center of mass. In addition, the moment due to accidental torsion affects the computed drifts, such that even symmetric buildings will have  $TIR > 1$ . The *TIR* essentially combines torsional flexibility and plan asymmetry into a single measure of a building’s torsional characteristics. Since U.S. designers are already required to compute the *TIR* to determine whether a horizontal irregularity exists, it provides a convenient measure of a building’s torsional properties. Measuring torsional flexibility based on frame spacing (*e.g.*  $S/L$ ) becomes impractical for buildings with more than two frame lines in each direction.

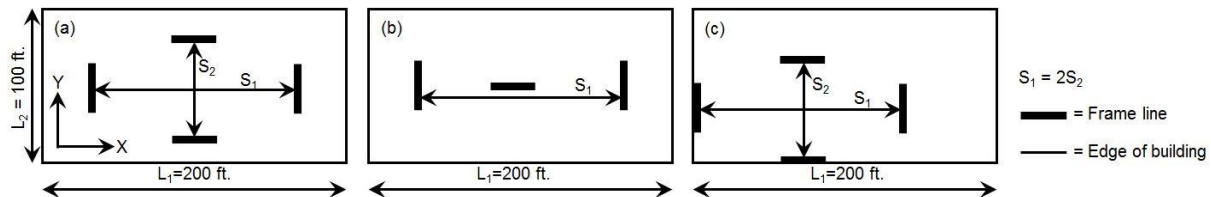


**Figure 2.2** Plan view of archetype buildings with (a) rectangular frame layouts, (b) I-shape frame layouts, and (c) inherent torsion (offset rectangular) frame layouts.

## 2.4.2 Design and Modeling of Archetype Buildings

The archetype design space consists of 460 buildings with varying lateral force-resisting systems, height, gravity loading, and frame layouts. Fully designing 460 buildings (composed of approximately 500 unique frame lines designed for different levels of lateral load) for this assessment is practically infeasible. Instead, only a carefully selected subset of 2D RC frames is fully designed. This subset of frame designs is used to develop 2D RC frame models (referred to as ‘high-end’ models), which provide the basis for calibrating a large number of simplified

nonlinear models. 3D models are created by combining the simplified 2D frame models to represent each of the 460 buildings of interest. This process is described in detail below.

#### 2.4.2.1 Design of the RC Frames

Thirty-two 2D RC frames are designed according to the ACI 318-05 (ACI 2005) and ASCE/SEI 7 (ASCE 2010) design standards, representing each combination of gravity load, building height, and seismic-lateral-force-resisting system: 12 OMFs and 20 SMFs, as listed in Table 2.1. Since different 3D plan layouts result in different design loads, the frame designs span the range of design loads in the archetype design space. For example, the first two rows in Table 2.1 describe the frames that are fully designed for the one-story, low gravity OMF archetypes: frame *O1* is designed for the lowest design base shear of any frame in the 3D OMF buildings with low gravity load and rectangular frame layout (corresponding to a frame in a symmetric building designed without accidental torsion), and frame *O2* is designed for the largest design base shear for any frame of the 3D OMF buildings with low gravity load and rectangular frame layout.

The design base shear for the 2D frames is based on the required seismic loads and the 3D configuration for which it is associated. Seismic design according to Chapter 11 of ASCE/SEI 7 depends on site-specific values of earthquake spectral acceleration. The design short period and one-second spectral accelerations used are the maximum allowable values for SDC B buildings ( $S_{DS} = 0.33 g$  and  $S_{DI} = 0.13 g$ ) and in the upper range of SDC D buildings ( $S_{DS} = 1.0 g$  and  $S_{DI} = 0.6 g$ ). For SDC D buildings (*i.e.* the SMF archetypes), ASCE/SEI 7 also imposes an amplification factor ( $A_x$ ) by which design accidental torsion forces must be multiplied.  $A_x$  varies from 1.0 to 3.0, depending on the frame layout. For this reason, the SMF frames in Table 2.1 have a larger range of design base-shear values.

**Table 2.1 Matrix of 2D Frame Designs for RC OMFs and RC SMFs**

Frame Index	Lateral System	Frame Layout	Building Height (Stories)	Gravity Loads	Relative Design Base Shear <sup>a</sup>	Frame Index	Lateral System	Frame Layout	Building Height (Stories)	Gravity Loads	Relative Design Base Shear <sup>a</sup>
O1 <sup>b</sup>	RC OMF	Rectangular	1	Low	1.00	S1 <sup>d</sup>	RC SMF	Rectangular	1	Low	1.00
O2					1.32	S2					1.20
O3				1.00	S3	1.43					
O4			High	1.32	S4	1.00					
O5				1.00	S5	1.20					
O6			4	Low	1.32	S6			1.43		
O7		1.00			S7	1.00					
O8		High		1.32	S8	1.20					
O9			1.00	S9	1.43						
O10		10	High	1.32	S10	1.00					
O1 <sup>c</sup>				High	1.00	S11		1.20			
O2			1.32		S12	1.43					
O11	I-Shape	1	High	0.50	S13	1.00					
O1				1.00	S14	1.20					
O2				1.32	S15	1.43					
O12	Inherent Torsion	1	High	2.00	S4	1.00					
						S16	1.19				
						S17	1.46				
				S18	0.05						
				S4	1.00						
				S19	1.25						
				S20	2.00						
		I-Shape	1	High				1	High		
		Inherent Torsion	1	High				1	High		

<sup>a</sup>Relative base shear is the design base shear of the 2D frame divided by the design base shear of a 2D frame designed for a nominally symmetric 3D frame layout and without design for accidental torsion.

<sup>b</sup>Ordinary Moment Frames have numbers preceded by the letter "O."

<sup>c</sup>Frames that are identical in design base shear, number of stories, and gravity load are assigned the same index.

<sup>d</sup>Special Moment Frames have numbers preceded by the letter "S."

Each 2D frame is designed for dead, live, and seismic loads using applicable load combinations from ASCE/SEI 7 (ASCE 2010). Snow and wind loads are not considered, but live load reduction factors are applied. Dead loads are based on a two-way flat slab floor system and spans of 30 ft. Story heights are taken as 15 ft. for the first story and 13 ft. for all other stories. For design purposes, frames are modeled in SAP2000 (CSI 2009), and the Equivalent Lateral Force Procedure is used to determine element design loads, story forces, and drifts. Member sizes and reinforcement in the OMFs are force controlled, with the exception of the ten-story frames whose lowest six stories are governed by the stability ( $P-\Delta$ ) requirements. The low base-shear SMF designs are generally controlled by force and joint size requirements. The high base-shear SMFs, which are associated with designs that have amplified accidental torsion, are

typically controlled by drift limits. ASCE/SEI 7 imposes stricter drift requirements on buildings with high *TIR* in SDC D.

#### 2.4.2.2 High-End Models of RC Frames

Each of the RC frames listed in Table 2.1 are modeled as 2D moment frames in *OpenSees* (PEER 2009) in what we refer to as ‘high-end’ models. As illustrated in Figure 2.3(1), columns and beams are modeled using calibrated lumped plasticity elements. Plastic hinges are assigned the hysteretic material developed by Ibarra *et al.* (2005), which is defined by a tri-linear monotonic backbone and incorporates both cyclic and in-cycle deterioration. The negative post-capping slope and deterioration capabilities are particularly important parameters for modeling collapse (Haselton *et al.* 2007). The hysteretic properties of the nonlinear beam-column hinges are computed from empirical relationships developed by Haselton *et al.* (2008) based on the design properties of the beams and columns (*i.e.* concrete strength, element dimensions, axial load ratio, and reinforcement detailing). As a result, element modeling reflects design and detailing differences between frames. Distributed gravity loads are applied to the beams. Gravity loads contributing to seismic mass, but not tributary to the frame, are applied to leaning (*P-Δ*) columns connected to the frame by rigid truss elements. In the design and in the *OpenSees* models, the fixities at the base of the first-story columns are modeled as pinned in the one-story models and fixed for the others. The different fixity assumption with changes in building height is consistent with common design practice.<sup>4</sup>

---

<sup>4</sup> In reality, different foundation conditions may provide different levels of restraint to columns. However, a side study showed that foundation stiffness has only a minor effect on collapse capacity (<5% difference) and a negligible effect on relative changes in collapse performance, the primary interest of this study.

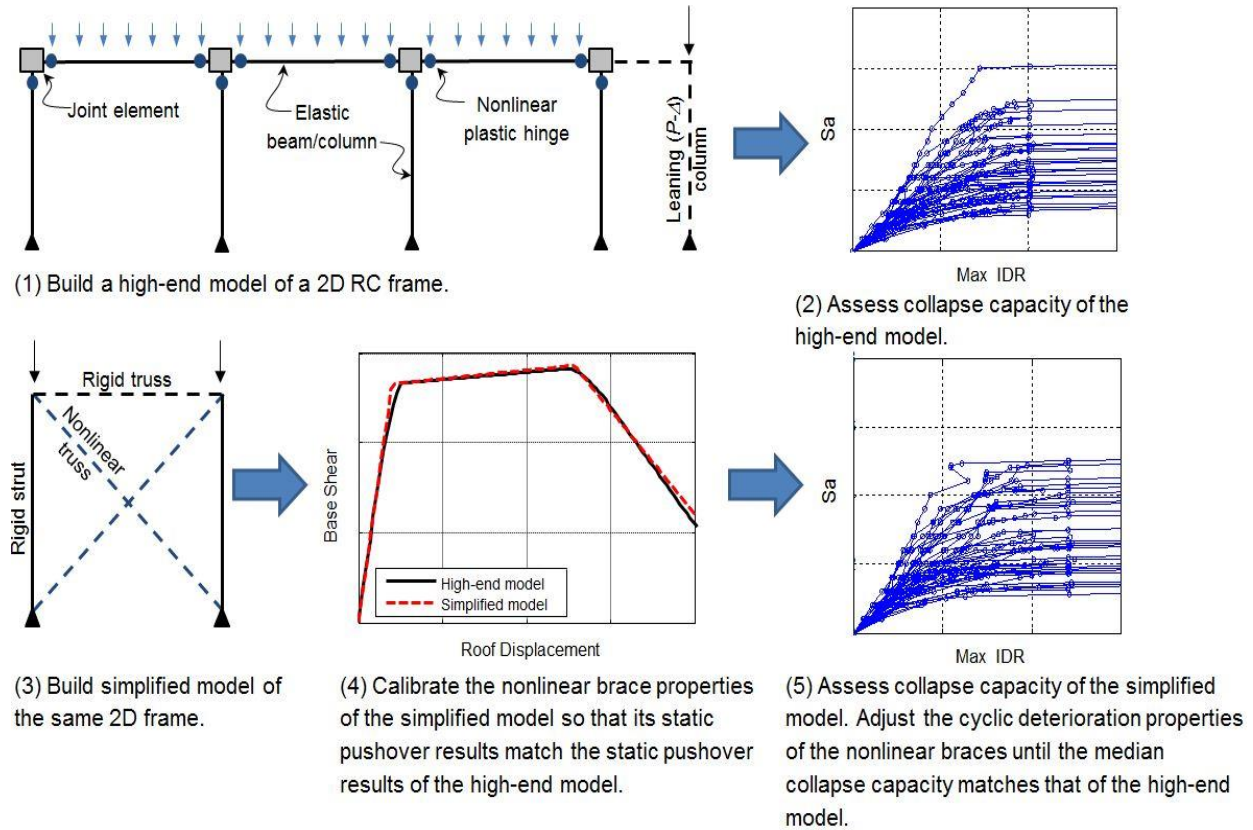


**Figure 2.3 Procedure for calibrating a simplified model to a high-end model of a 2D RC frame.**

### 2.4.2.3 Simplified Model Calibration

A simplified 2D single bay frame model with nonlinear X bracing, as shown in Figure 2.3(3) and Figure 2.4, is calibrated to each of the high-end 2D frame models. The monotonic backbone properties defining the nonlinear brace (truss) elements are calibrated such that the static pushover behavior of the simplified frame matches the pushover results from the corresponding high-end model, as shown in Figure 2.3(4). The cyclic deterioration properties of the simplified models are calibrated such that the median collapse capacities obtained from the high-end models (Figure 2.3(2)) and the simplified models (Figure 2.3(5)) match within 2%. The process for assessing collapse capacity is described in more detail below.

In the simplified models of the multi-story frames, elasto-plastic plastic hinges are added at the joints between stories to transfer moments between adjacent stories. The properties of these hinges are calibrated as well as the properties of the nonlinear truss elements. In doing so, the distribution of damage over the height of the building of the high-end models, as well as the higher mode periods, is matched by the simplified models. As a consequence, the calibration process is able to closely match the deformed shape from pushover. A schematic drawing of the multi-story simplified frame models is depicted in Figure 2.4.

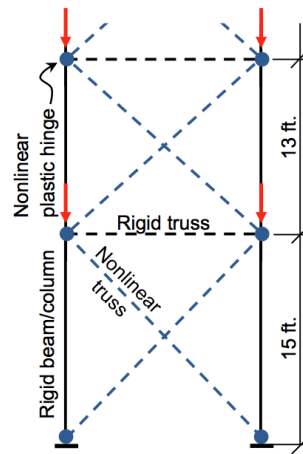


**Figure 2.4 Illustration of a simplified model of a 2D RC frame.**

#### 2.4.2.4 3D Models

The 3D archetype models are constructed from the simplified 2D models based on the plan dimensions and frame layouts shown in Figure 2.2. The plan view of a typical 3D model is presented in Figure 2.5.

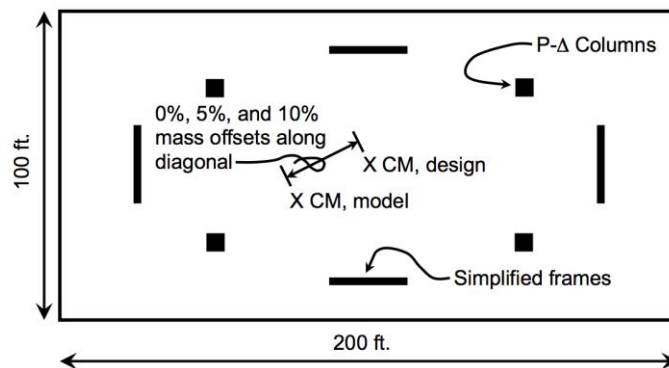


**Figure 2.5** Typical 3D model plan view.

Archetype buildings that are designed for accidental torsion, and those with inherent torsion, may contain frames whose design base shear does not correspond exactly to any of the 32 high-end frames. The modeling properties needed for these frames are obtained by linear interpolation of model properties for frames of the same height, gravity load, and type (OMF or SMF). This interpolation is based on design base shear and applied to determine both cyclic and monotonic properties. For example, Figure 2.6 shows the nonlinear brace properties for three simplified frame models; the top and bottom curves are for simplified models calibrated to match high-end models of 2D frames, as illustrated in Figure 2.3. Consider a third RC frame whose design base shear is between that of the frames corresponding to the two high-end models, but for which a high-end model is not developed. The model properties for this intermediate frame are interpolated from the nonlinear model properties for the other simplified frame models. The consequence of the interpolation process is that changes in design base shear of the 2D frames lead to changes in building model properties (*e.g.* strength, stiffness, *etc.*) that are consistent with those observed in the high-end frame models. These simplified frame models are then combined to create a 3D model.

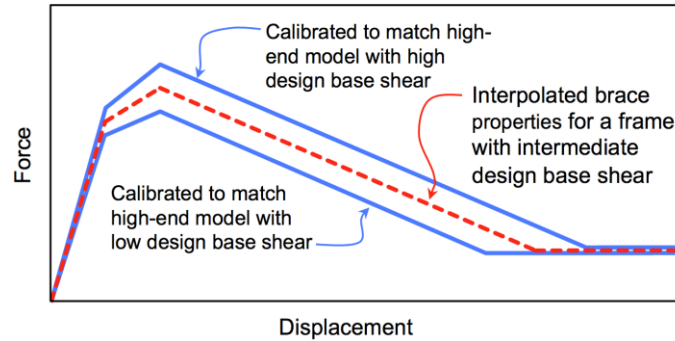


**Figure 2.6 Sample interpolation of nonlinear brace properties for a simplified 2D model.**

The mass of each story in the 3D building models is based on the gravity load level and plan area. The rotational moment of inertia is computed assuming that the mass is evenly distributed across the building floor plan. As a result, the 3D models have inertial and torsional properties that are representative of realistically sized buildings and consistent with the constituent 2D frames. The gravity framing system is not modeled, and, therefore, does not contribute to the strength and stiffness. However,  $P-\Delta$  loads are applied on four leaning columns that are placed at the center of each quadrant of the building footprint, as shown in Figure 2.5.

Since the purpose of this study is to evaluate accidental torsion design requirements, varying levels of accidental torsion are simulated in the 3D archetype models (hereafter referred to as ‘model accidental torsion’) by offsetting the model center of mass from the design center of mass by 0%, 5%, and 10% along the diagonal dimension of the plan of the building, as shown in Figure 2.5. Model accidental torsion is imposed independently of design accidental torsion such that all three levels of model accidental torsion are imposed for all archetypes, whether or not accidental torsion is considered in design. For clarity, we point out that model accidental torsion refers to mass offsets introduced into the 3D models in order to simulate unexpected (*i.e.* accidental) sources of torsion (*e.g.* uneven live-load distribution, *etc.*). Models of buildings with

*inherent torsion* have different centers of rigidity associated with the frame distributions, which are directly accounted for in the design process.

#### 2.4.2.5 *Non-Simulated Collapse Modes*

RC SMFs are subject to a large number of capacity design and reinforcement detailing requirements, such that shear failure of joints and columns is prevented, and beams are expected to yield before columns. The modeling approach described above is capable of simulating the sidesway collapse of these frames. Since there are more limited requirements for seismic detailing of reinforcement for OMFs, other failure modes are also possible. To capture joint shear failure, the OMFs are modeled with nonlinear beam-column joints whose properties are computed based on Altoontash (2004) and Lowes *et al.* (2004). Due to deficiencies in detailing, two additional failure modes are possible for the OMFs: (1) loss of vertical carrying capacity of the gravity system and (2) loss of vertical carrying capacity of the OMF's columns due to shear failure. These failures are not simulated by the models. Gravity system failure is not simulated directly, because columns and beams designed only to carry gravity loads are not included in the models. Real buildings may have no independent gravity system (*e.g.* the lateral system also serves as the gravity system) or a robust separate gravity system (*e.g.* interior gravity-only columns). Since our analyses are intended to broadly represent all of these buildings, no gravity system is modeled. Instead, non-simulated failure modes account for the possibility that the gravity elements may fail before the seismic-lateral-force-resisting-system. Non-simulated gravity system failure is based on interstory drift ratio (IDR) limits that represent the drift capacity at which non-ductile gravity systems (like those found with RC OMFs) are likely to fail. Since the drift capacity of these gravity systems is unknown, two drift thresholds (IDR = 3% and IDR = 6%) are considered, based on a range of potential values identified in ASCE/SEI 41-06

(ASCE 2007). Considering the second possible non-simulated failure mode for OMFs, research is ongoing to directly simulate shear failure of concrete columns (Elwood 2004, Ghannoum and Moehle 2008), but brittle shear failure is not captured by the column hinges used in the high end models. Instead, column shear failure is accounted for through post-processing of dynamic analysis results, comparing the drifts experienced by the structure to the drifts at which columns lose their ability to carry gravity loads due to shear failure. Prediction of the drift capacity of columns associated with this failure mode is based on Aslani (2005). Since we aim to consider as wide a range of buildings as possible, each of these collapse criteria is employed separately in our analyses of OMF buildings to obtain collapse capacities associated with each possible collapse mode.

### **2.4.3 Dynamic Analysis of Archetype Building Models**

The archetype building models are analyzed using incremental dynamic analysis (IDA). In IDA, a building model is subjected to a recorded ground motion in incrementally increasing intensities until collapse occurs, as indicated by interstory drifts increasing without bounds (sidesway collapse). In some cases, non-simulated collapse mechanisms are found to have preceded sidesway collapse through post processing of dynamic analysis results.

Each of the archetype building models is subjected to 22 pairs (44 horizontal components) of far-field strong ground motions from FEMA P-695 (FEMA 2009). These ground motions are recorded from large magnitude events at moderate rupture distances. The same set of ground motions is used to analyze archetypes designed for all seismic design categories, since it provides a consistent ground motion record set or loading protocol to examine relative changes in collapse capacity due to changes in design. This set of ground motions also contains broadband frequency content, which is important for analyzing buildings with varying lateral and

torsional periods.<sup>5</sup> Per FEMA P-695, each ground motion record is normalized by its peak ground velocity and the ‘cloud’ of normalized records scaled together. Ground motion intensity is quantified by the median spectral acceleration of the cloud at the code-specified fundamental period of the building. Since the normalization process preserves variability in spectra, even at the first mode period  $T_1$ , the spectral acceleration of a particular record may be higher or lower than the median spectral acceleration of the cloud.

IDA results characterize the ground motion intensity at which each record causes collapse, serving to quantify the median and variability in the ground motion intensity necessary to cause collapse. In FEMA P-695, the primary statistical measure of collapse performance is the Collapse Margin Ratio (*CMR*) (FEMA 2009). The *CMR* is a sort of capacity to demand ratio computed from the ratio of the median ground motion intensity at which collapse occurs, to the maximum considered earthquake (*MCE*) ground motion intensity. Mathematically,  $CMR = \hat{S}_{CT}/S_{MT}$ , where  $\hat{S}_{CT}$  is the median value of spectral acceleration at the building’s fundamental period of vibration ( $T_1$ ) for which collapse occurs and  $S_{MT}$  is the code-defined MCE spectral ordinate.  $S_{MT}$  is 1.5 times greater than the design spectral acceleration value at the building’s fundamental period, according to ASCE/SEI 7.

A complication arising from use of this general ground motion set (as opposed to ground motions specifically selected for each building and site) is that computed *CMRs* are inherently conservative. This conservatism stems from the ground motion set’s broad range of frequency content, which does not represent rare large ground motions that tend to have spectral peaks, particularly in California (Baker and Cornell 2006, Haselton and Baker 2006). To account for

---

<sup>5</sup> Since the archetype models are 3D, IDA is performed twice for each of the 22 pairs of ground motion components. First, horizontal component 1 is applied along the y-axis of the building and, simultaneously, component 2 applied along the x-axis. In the second analysis, the orientation of the two components is switched.

this effect, FEMA P-695 defines a spectral shape factor (*SSF*), which is multiplied by the *CMR* to obtain an Adjusted Collapse Margin Ratio (*ACMR*). *SSFs* are on the order of 1.5 for SDC D and 1.3 for SDC B and depend on building period and ductility. In addition, the *CMRs* of 3D buildings are also multiplied by a factor of 1.2, per FEMA P-695, making their collapse capacities consistent with their 2D counterparts, which only consider collapse in one direction, rather than both directions simultaneously. The final *ACMR* of 3D building models is computed as  $ACMR = CMR \times SSF \times 1.2$ .

## 2.5 Findings

### 2.5.1 Definition of Terms

This study uses two metrics to evaluate ASCE/SEI 7 accidental torsion provisions and to identify those buildings and sites for which accidental torsion design requirements are important. The primary metric, termed *significance*, is a measure of the decrease in collapse resistance that results if accidental torsion provisions are omitted from the design process:

$$Significance = 1 - \left( \frac{ACMR \text{ of Bldg. } X \text{ designed without accidental torsion}}{ACMR \text{ of Bldg. } X \text{ designed with accidental torsion}} \right) \quad 2.1$$

Large values indicate that design accidental torsion contributes significantly to the collapse resistance of the building. Significance is illustrated in Figure 2.7(a).

A secondary parameter represents the need for design accidental torsion requirements. The premise for this definition is that the most torsionally stiff buildings are not substantially affected by design requirements for accidental torsion, nor are they substantially affected by the impacts of accidental torsion on building dynamic response. To evaluate the need for accidental torsion provisions in design of other buildings, collapse capacities of buildings with various levels of TIR, all of which are designed without considering accidental torsion, are compared to

‘benchmark’ building counterparts. The ‘benchmark’ building corresponds to a perimeter frame building not designed for accidental torsion and having the same height and gravity load as the building of interest. As a consequence of the perimeter frame layout (i.e., lateral resisting frames on the perimeter of the building), the benchmark structures are torsionally stiff. The need is the deviation of their collapse capacity (ACMR) from the collapse capacity of the benchmark building, as shown in Figure 2.7(b). Larger need indicates bigger differences between collapse capacities among buildings with different torsional properties, but all else equal, providing motivation for accidental torsion provisions to preserve more consistent collapse capacities across buildings with different torsional behaviors. Since need is computed from analyses of buildings designed without accidental torsion, it does not depend on how accidental torsion design requirements are implemented in codes. Rather, need indicates the degree to which accidental torsion design requirements, of any kind, are necessary for torsionally sensitive buildings.

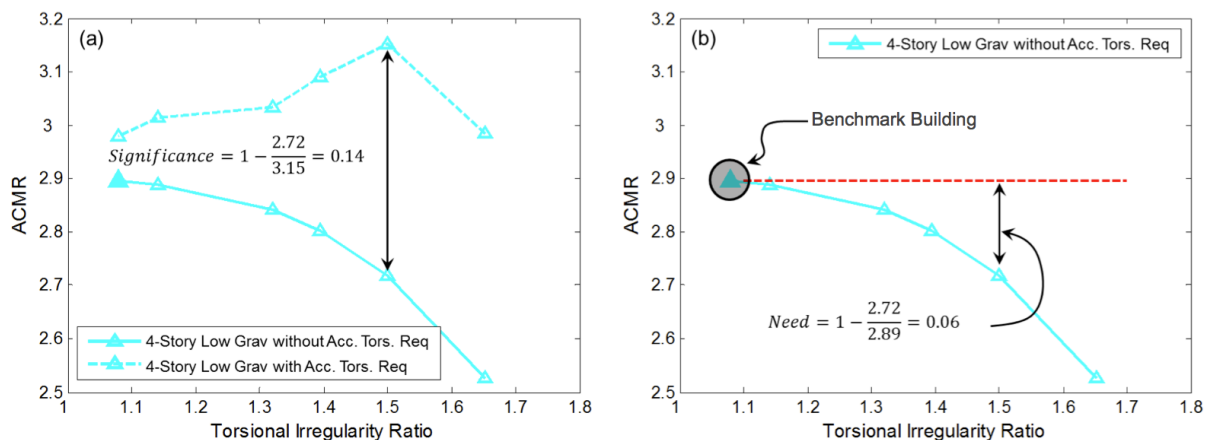


**Figure 2.7** Illustration of calculation of (a) *significance* of design accidental torsion requirements and (b) *need* for design accidental torsion requirements for the four-story low gravity SMF archetype, having a rectangular frame layout and  $TIR = 1.5$

In the sections that follow, *significance* of accidental torsion provisions is reported for all of the buildings, providing the primary basis for the evaluation of design accidental torsion design

provisions. The computation of *need* for accidental torsion provisions supplements these observations.

### 2.5.2 Trends with the Torsional Irregularity Ratio

The archetype buildings vary in terms of height, gravity loading, seismic-lateral-force-resisting-system, frame layout (*i.e.* rectangular, I-shape, or inherent torsion), model accidental torsion, and *TIR*. The results show that *significance* of the ASCE/SEI 7 accidental torsion provisions is strongly influenced by the building's torsional irregularity and flexibility, quantified by the *TIR*. Figure 2.8 plots the *significance* of accidental torsion requirements for different groups of buildings with varying *TIR*, showing that the *significance* of design accidental torsion increases as the *TIR* increases. This result shows that as a building becomes more torsionally flexible or irregular, accidental torsion provisions become increasingly important in design. This finding is confirmed by Figure 2.9, which reports collapse capacities (*ACMRs*) for the archetype buildings that are not designed for accidental torsion. The observed collapse capacities decrease as the *TIR* increases, indicating increasing *need* for accidental torsion in design for all of the archetype buildings considered.

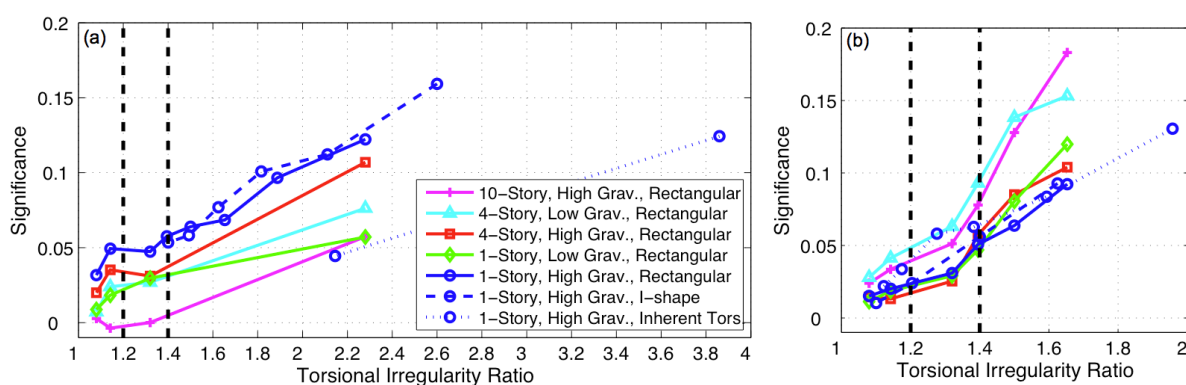


**Figure 2.8** *Significance* of accidental torsion design requirements for (a) OMF archetypes (SDC B) and (b) SMF archetypes (SDC D). The dashed vertical lines represent ASCE/SEI 7-defined thresholds classifying a building as having horizontal irregularity Type 1a ( $TIR = 1.2$ ) and Type 1b ( $TIR = 1.4$ ).

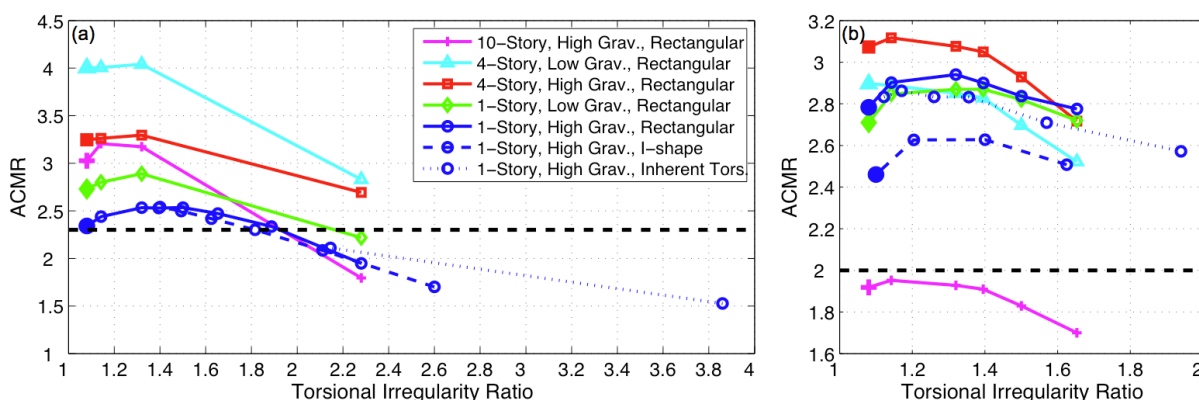


**Figure 2.9 Collapse capacities for (a) OMF archetypes (SDC B) and (b) SMF archetypes (SDC D). Results are for simulated collapse modes only and analyses with model accidental torsion corresponding to a 5% offset of the center of mass.**

Although this study evaluates accidental torsion provisions through relative comparisons of collapse risk, we note that the absolute collapse capacities computed here are consistent with those reported in the OMF and SMF example studies in FEMA P-695. The *ACMR* values that exceed 2.3 for the OMFs or 2.0 for the SMFs (shown by the horizontal dashed lines in Figure 2.9) satisfy acceptable capacity thresholds that are defined by the FEMA P-695 methodology. These thresholds correspond to less than 10% probability of collapse under the MCE level ground shaking (FEMA 2009).

### 2.5.3 Comparison of Significance of Accidental Torsion Requirements for Ordinary and Special Moment Frames

Comparison of Figure 2.8(a) and (b) shows that the *significance* of ASCE/SEI 7 accidental torsion provisions increases faster with *TIR* for the SMF archetype buildings than for the OMFs. The greater *significance* of accidental torsion provisions in SMFs is due to two related design requirements imposed in SDC D by ASCE/SEI 7: (1) the torsion amplification factor ( $A_x$ ), which amplifies design accidental torsion moments by a factor between one and three, depending on a building's *TIR*, and (2) the requirement that drift limits under design seismic load be satisfied at

the building's edges, rather than at the center of mass, for buildings with large  $TIR$ . Since building design is controlled by force demands or drift limits, more stringent requirements for both guarantees that design accidental torsion will play a more significant role for SDC D buildings like the RC SMF archetypes.

To explore the importance of these additional SDC D requirements, Figure 2.10(a) reports the collapse capacities of the four-story SMF archetypes for three sets of design provisions: (1) no design accidental torsion, (2) all current SDC D accidental torsion-related code requirements, including the design accidental torsional moment,  $A_x$ , and drift limits enforced at the building edges, and (3) including the same design accidental torsional moment, but excluding requirements related to  $A_x$  and the additional drift limits. Accidental torsion requirements considered in Set 3 are identical to those applicable in SDC B, *i.e.* for buildings like the RC OMFs. When  $TIR < 1.2$ ,  $A_x$  and the extra drift limits do not apply, and Sets 2 and 3 are the same. The designs for many of the SMF buildings with high  $TIR$ s in Set 2 are controlled by the more stringent drift requirements.

Unsurprisingly, the buildings designed for accidental torsion with the amplification factor and additional drift requirements (Set 2) have higher collapse capacities than those designed only for the unfactored accidental torsion moment (Set 3) for all cases where  $TIR > 1.2$ . Figure 2.10(a) makes it clear that the combined effect of amplifying design accidental torsion moments and satisfying drift limits at building edges is important for preserving collapse capacity as  $TIR$  increases. In fact, Set 3 buildings still have a substantial *need* for accidental torsion provisions, illustrated by the decreasing collapse capacities as  $TIR$  increases, even though the accidental torsional moment is included in the design calculations.

To investigate the relationship between accidental torsion design requirements and lateral strength, Figure 2.10(b) plots the peak (lateral) pushover strength for the four-story low gravity SMF archetypes for buildings in Sets 1, 2 and 3. The pushover was conducted separately in the  $x$  and  $y$  directions using an inverted triangular loading, and results were normalized by the peak pushover strength of the benchmark building. When accidental torsion provisions are not considered (Set 1), the frame designs are all the same, regardless of  $S/L$  and  $TIR$ , since all of the buildings considered in this discussion are symmetric. When design considers accidental torsion, but without amplification or additional drift requirements (Set 3), the ultimate capacity of the frames in the short direction of the buildings (oriented along the  $y$ -axis in Figure 2.2) increases steadily as frame spacing ( $S/L$ ) decreases and  $TIR$  increases, due to the larger design loads associated with the accidental torsion moment. Since the frames oriented along the longer building dimension ( $x$ -direction) are more closely spaced than those along the short direction (*i.e.*  $S_2 < S_1$ ), they are designed to resist a small fraction of the accidental torsion moment and the increases in design loads with  $TIR$  are small. Hence, accidental torsion provisions lead to little change in the ultimate pushover capacity of the frames in the  $x$ -direction. The ultimate pushover strength of the frames in the  $y$ -direction designed with the full SDC D requirements (Set 2) grow substantially larger than the other cases when  $TIR$  is large. The lateral strength apparent in pushover stems from the amplification of the torsional moment and the additional drift limits that apply when  $TIR > 1.2$ . However, even for Set 2, the orthogonal ( $x$ -axis oriented) frames contribute little to the overall torsional resistance, so their pushover strength is not significantly affected. The additional strength that comes with the accidental torsion requirements related to the amplification factor and drift limits contributes to the preservation of collapse capacity with increasing  $TIR$  observed for Set 2 in Figure 2.10(a).

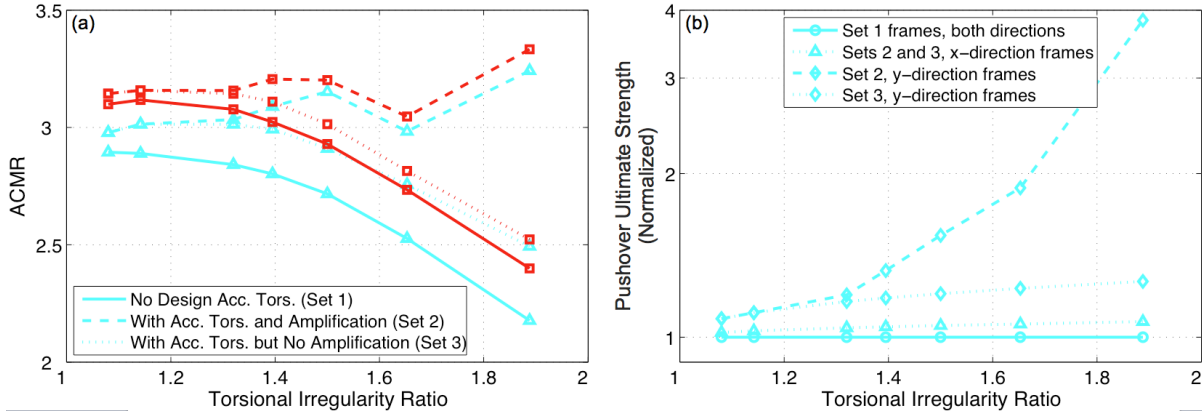


**Figure 2.10 (a) Comparison of ACMR for the four-story SMF archetype buildings. Results from low gravity archetypes are plotted with blue lines and triangular markers; results from high gravity archetypes are plotted with red lines and square markers. (b) Ultimate pushover capacities (normalized) of four-story low gravity SMF archetypes.**

The stringent drift limitations have a particularly large influence on the tallest and most flexible SMFs, accounting for the large *significance* of accidental torsion provisions observed for these buildings in Figure 2.8(b). For the tallest (ten-story) buildings, the large member sizes needed to satisfy drift limits when accidental torsion is included in the design lead to substantial increases in strength, particularly for buildings with large *TIR*. It is well known that stronger columns significantly improve collapse performance (Haselton *et al.* 2011). On the other hand, the ten-story OMF archetypes, which are not required to satisfy the additional drift limits, benefit less from accidental torsion requirements.

#### 2.5.4 Effect of Inherent Torsion

Past research has shown that design accidental torsion is less important for the design of irregular buildings, *i.e.* those with inherent torsion, because torsion is already considered in the design, regardless of whether accidental torsion is also considered. This study considers both symmetric archetypes and asymmetric archetype buildings. The asymmetric buildings are designed with inherent torsion and labeled as such on Figure 2.8 and Figure 2.9.

To examine the effect of inherent torsion in this study, consider first the 1-story high gravity archetype buildings in Figure 2.9(a). Those with inherent torsion tend to have larger *TIRs* and lower collapse capacities than buildings without inherent torsion. However, examining two buildings with the same *TIR* (e.g.  $TIR = 2.2$ ), we note that the collapse capacities are very close to the same for the torsionally flexible, but symmetric buildings (e.g. 1-story high gravity with rectangular frame layout), and the torsionally stiff, but asymmetric buildings (e.g. the 1-story high gravity archetypes with inherent torsion). Examining directly the *significance* of design accidental torsion provisions as a function of *TIR*, Figure 2.8(a) shows the accidental torsion provisions are less significant for the one-story buildings with inherent torsion, compared to the other one-story high gravity OMF archetypes, which do not have inherent torsion. Consider, however, if the relative frame spacing ( $S/L$ ) is taken as the independent variable rather than *TIR* on the x-axis. Although not shown, in this case, the curves representing *significance* are very similar for OMF archetypes with and without inherent torsion. Frame spacing is directly related to *significance* of design accidental torsion provisions, because the increases in design base shear due to design accidental torsion are a function of the frame spacing. This result suggests that torsional flexibility (*i.e.* frame spacing), not inherent torsion, is the primary variable of importance in predicting the *significance* of accidental torsion provisions for the OMF archetype buildings.

The story is a little different for the SMF archetypes; the archetype buildings with inherent torsion follow the same general trend for *significance* of design accidental torsion as their corresponding symmetric SMF archetypes in Figure 2.8(b). Both of the additional design requirements for accidental torsion in SMFs are strongly tied to *TIR*:  $A_x$  is proportional to  $TIR^2$  (within the bounds of  $1.0 \leq A_x \leq 3.0$ ) and the *TIR* is a function of the drifts at the building edges.

As a result, for the SMFs, the increases in design forces due to accidental torsion are more strongly related to *TIR* rather than frame spacing, and buildings with the same *TIR* have approximately the same computed *significance*, regardless of whether it stems from irregularity (*i.e.* inherent torsion) or torsional flexibility. As with the OMFs, Figure 2.9(b) shows that the collapse capacities of the SMFs with inherent torsion are on par with those that do not have inherent torsion, given that they have the same *TIR*.

### 2.5.5 Trends with Other Building Characteristics

Gravity load, frame layout, and building height (or number of stories) are not important predictors of the *significance* of ASCE/SEI 7 accidental torsion provisions. The *significance* of design accidental torsion is insensitive to the level of gravity load, because the relative changes in lateral design forces associated with accidental torsion requirements depend on plan configuration, not gravity load level. Neither is building height identified as a major factor affecting the *significance* of design accidental torsion, primarily because the height of a frame also does not affect the relative changes of design forces due to accidental torsion. Nevertheless, it is worth noting that the absolute collapse capacities of the archetypes do vary notably with building height. In particular, the four-story buildings typically have higher collapse capacities, because they tend to experience the most even distribution of damage over building height (*i.e.* more multi-story mechanisms).

The results also show that, for buildings without torsional irregularities (*i.e.* low *TIR*), the *significance* of design accidental torsion is insensitive to model accidental torsion, which is introduced through center of mass offsets modeled in dynamic analyses. Increasing model accidental torsion does lower the absolute collapse capacity of the buildings. However, for buildings with  $TIR < 1.6$ , this difference is relatively consistent across all of the archetype

buildings, in that 10% center of mass offsets result in a 3% to 10% reduction in collapse capacity. As a result, offsetting the center of mass reduces the collapse capacities of buildings designed with and without accidental torsion by the same amount, so the computed *significance* is unaffected. The *significance* of design accidental torsion is insensitive to model accidental torsion for buildings with  $TIR < 1.6$ , because the responses of such buildings are dominated by lateral motion. Therefore, amplifying the torsional response by adding model accidental torsion has little impact on building performance, because the torsional response is still small compared to the lateral motion. In contrast, buildings with  $TIR > 1.6$  tend to have much larger torsional responses to earthquake ground motions, because they are more torsionally sensitive (*i.e.* torsionally flexible and/or asymmetric). As a result, the increases in torsional responses of torsionally sensitive models that result from model accidental torsion have a much greater impact on the total response, so the accidental torsion provisions intended to resist them become more significant. For simplicity, the significance values that are presented in Figure 2.8 are averages over the three levels of model accidental torsion (*i.e.* 0%, 5%, and 10% mass offsets), even though this does not tell the entire story for buildings with  $TIR > 1.6$ .

One other characteristic of the building models that deserves consideration is the criteria for evaluating non-simulated collapse modes of the OMF buildings. Recall that, in addition to sidesway collapse, which is simulated directly by the nonlinear models, two non-simulated collapse modes representing possible failures of the gravity system are considered, and one non-simulated collapse mode considers shear failure of columns, for a total of four different collapse modes. Which, if any, of the collapse modes should be considered depends on characteristics of the building that are not represented in the nonlinear simulation models, such as the detailing of the gravity system or shear reinforcement in columns. Accordingly, all collapse modes are

treated as equally likely representations of behavior of the real building stock. Therefore, the *significance* of accidental torsion design requirements for the OMF buildings is computed considering each collapse mode individually, for a total of four computations of *significance* for each archetype building. The values of the *significance* of design accidental torsion are similar, regardless of the collapse mode considered, so the final *significance* results presented in Figure 2.8(a) are an equally weighted average of all four.

### 2.5.6 Verification of Observations by Statistical Analysis

To support the observations above, the influence of each of the different building characteristics on the *significance* of ASCE/SEI 7 design provisions for accidental torsion is evaluated using the statistical computing program *R* (Therneau and Atkinson 2010). The analysis employs a binary regression tree (Hastie *et al.* 2008). The regression tree is constructed by computing the mean and variance in the dependent variable (*i.e.* the *significance* of design accidental torsion) for all buildings. Then, the analysis examines all possible criteria for splitting the data into two subgroups based on the identified predictors (*i.e.*, building characteristics), selecting the split that results in the lowest complexity of the two groups. The complexity is related to variance of the dependent variable in the resulting groups. At each level, the split indicates which building characteristic has the greatest influence on the *significance* of design accidental torsion.

As shown in Figure 2.11, the regression tree identifies *TIR* as the most significant predictor, because it accounts for the largest portion of the complexity in the *significance* among the entire group of archetype buildings. Therefore, it separates the data into two subgroups based on the value of the building's *TIR*. The threshold value of  $TIR = 1.50$  is selected because that split minimizes the computed complexity of the data. This process is repeated for the resulting

subgroups until the binary regression tree grows to what is shown in Figure 2.11; normalized values representing the variance of each group or “leaf” show the reduction in variance achieved by each branching of the tree.

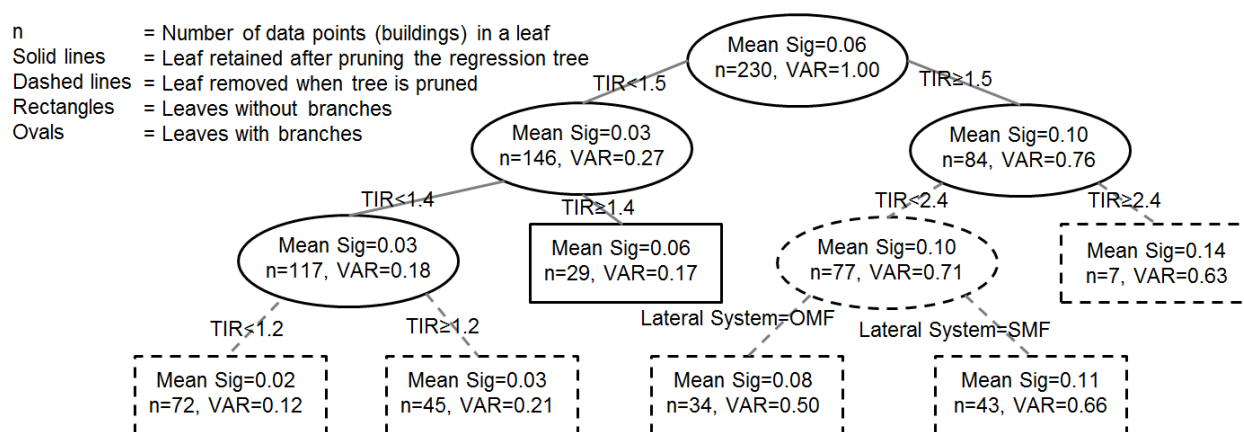


**Figure 2.11 Binary regression tree for predicting the *significance* (denoted “Sig”) of design accidental torsion requirements from building characteristics.**

Theoretically, the binary regression tree could be grown until each leaf contains only one data point and, hence, the variance of each group is zero. However, to avoid overfitting the regression, only those leaves that meaningfully improve the model’s ability to predict the *significance* of design accidental torsion are retained, and the other branches are “pruned”. To prune the tree, a randomly selected 10% of the data points are dropped and the regression tree is refitted to the remaining data. Then, in a process known as cross-validation, the refitted model is used to predict the *significance* of design accidental torsion for the buildings in the dropped data set. When a binary regression model is used as a predictive tool, the prediction is taken as the mean *significance* for the leaf with the same properties as the building of interest. The difference in predicted *significance* for the dropped data and the actual observed *significance* from dynamic analysis provides a measure of the predictive ability of the regression tree. Only splits that

improve the prediction quality (*i.e.* reduce the cross-validation error) are retained, as shown by the solid lined portions of Figure 2.11. The  $R^2$  value of the pruned regression tree is 0.61.

The branches remaining in the pruned tree are all based on *TIR*, indicating that it is the building characteristic that most strongly predicts the *significance* of design accidental torsion. Although not shown here, a similar tree confirms that *TIR* is also the best predictor of the *need* for accidental torsion design requirements.

## 2.5.7 Additional Parametric Studies

### 2.5.7.1 Effect of Torsional Period

A peculiarity observed in Figure 2.9 is that the collapse capacities of the archetypes designed without accidental torsion provisions tend to increase slightly from the benchmark for small *TIR* before showing a decrease in collapse capacity with increasing torsional irregularity and flexibility. The largest collapse capacities are typically observed for  $1.2 < TIR < 1.4$ . As *TIR* increases, the torsional period increases. When *TIR* is small, this increase in torsional period moves torsional response out of the period range for which the ground motion set has strongest spectral content and into a range for which the ground motions have weaker spectral content. Taking the four-story low gravity SMF archetypes as an example, when the *TIR* increases from 1.1 to 1.3, the period of the first torsional mode increases from 0.80 sec to 1.6 sec., and the median spectral acceleration of the normalized ground motion set at the torsional period decreases from 0.46g to 0.21g, a reduction of more than 50%. As a result, the buildings with a little more torsional flexibility often outperform the more torsionally rigid structures (resulting in negative *need*). This occurs because the torsional modes are more excited in the torsionally stiff (short-torsional-period) archetypes.

To examine whether there may be buildings designed according to ASCE/SEI 7 requirements for which this benefit from an increase in torsional period is not present, additional permutations of the four-story low gravity SMF archetypes designed without accidental torsion requirements are analyzed with artificially altered torsional periods. Shortening (or elongation) of the torsional periods in real buildings could result from changes in the size of a buildings' plan dimensions, because changes in plan dimensions do not affect torsional stiffness and torsional mass equally. In the first group, the modeled rotational inertia of the floor slabs in each of the four-story low gravity SMF archetypes is reduced such that their resulting fundamental torsional periods range from 0.25 to 0.80 sec. In the second group, the rotational inertia of the same archetypes is increased such that their fundamental torsional periods range 1.6 to 4.3 sec. No changes are made to the frames themselves, so the period of the first lateral mode is the same for all cases (1.4 sec). Figure 2.12(a) shows that the *need* for accidental torsion design provisions in archetypes whose torsional periods are altered to be very short increases more rapidly with *TIR* than those with realistic or artificially lengthened torsional periods. *Need* arises at smaller *TIR* results because the ground motion spectra have a lot of energy in the range of the shorter torsional periods and the increase in period with increasing *TIR* is not enough to move the buildings out of this range. Nonetheless, when the *TIR* is less than 1.2, there is low *need* for accidental torsion design requirements (less than 0.10), regardless of the torsional period. The torsional periods induced in the short-torsional-period models are an extreme case and not necessarily realistic.

#### 2.5.7.2 *Effect of Plan Configuration*

A second parametric study investigates a four-story low gravity SMF archetype that is square in plan and frame layout, rather than rectangular or I-shape. The results in Figure 2.12(a) show that the archetypes that are square in plan develop need for accidental torsion requirements at

lower TIRs than rectangular archetypes. Figure 2.12(b) shows that the collapse capacities of versions with square and rectangular frame layouts begin to deviate from the benchmark building's collapse capacity, developing need, at the same relative frame spacing ( $S/L$ ).

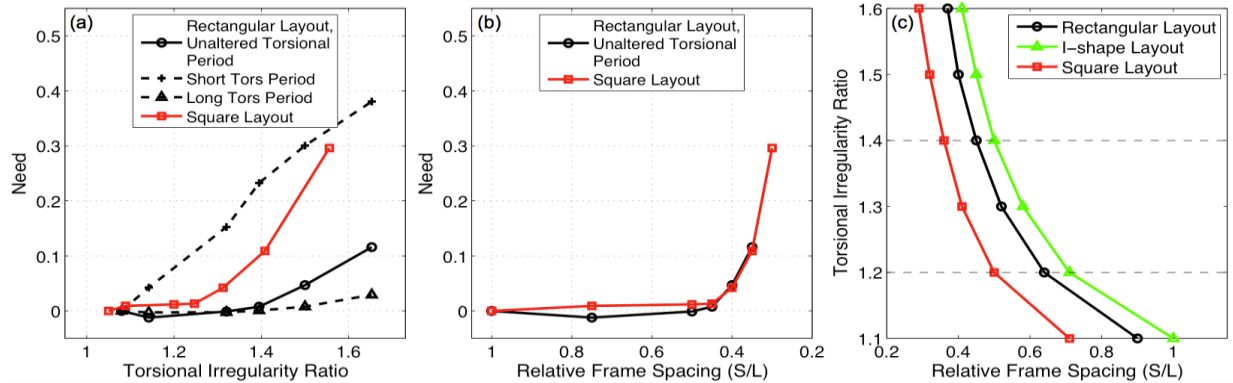


**Figure 2.12** (a) Trends in *Need* with respect to *TIR* for variations of the four-story low gravity SMF archetype with different torsional periods and frame layouts; (b) Trends in *Need* with respect to relative frame spacing ( $S/L$ ) for the same four-story archetype, with rectangular and square frame layouts; (c) Comparison of *TIR* vs. relative frame spacing ( $S/L$ ) for three different frame layouts.

Square layouts have the smallest TIRs for the same relative frame spacing ( $S/L$ ), as shown in Figure 2.12(c). Consequently, buildings with square layouts develop need for accidental torsion design requirements at lower TIRs than those with rectangular frame layouts.

## 2.5.8 Limitations

This study attempts a comprehensive assessment of accidental torsion provisions in design, involving 460 3D models, composed of over 500 unique 2D frame models, and requiring over 500,000 nonlinear dynamic time-history analyses. Nevertheless, the analysis results are contingent on limitations in the modeling and assessment procedure.

The 460 archetype buildings are intended to represent the range of buildings that are affected by accidental torsion provisions and their influence on design and seismic response. However, the archetype design space cannot possibly contain every potential building. The archetype design space has been carefully selected to include the most important building characteristics

from the perspective of understanding accidental torsion, but it is by no means exhaustive. In particular, the buildings represented here have less redundancy than some common systems (*e.g.* space frames), because they have only two frame lines in each orthogonal horizontal direction. Therefore, the collapse capacities of the buildings computed here may be more sensitive to changes in *TIR* than some buildings, such that our observations may be conservative for more redundant buildings. However, since the simplified models of the 2D frames are calibrated to match the aggregate behavior of high-end models of RC frames, they do deteriorate in a manner consistent with a moment frame system that has the redundancy of three bays in series.

Other limitations stem from the nonlinear simulation models that are used to predict building collapse. The rigorous calibration procedure that is used for creating the simplified models of the 2D frames is robust enough to capture the most important properties of the high-end frame models, *i.e.* strength, stiffness, damage concentration, deformation capacity, deterioration properties,  $P-\Delta$ , and higher mode effects. However, the macro-nature of the simplified models prohibits them from predicting behavior on a micro level (beam plastic hinge rotations, for example, are not simulated by the simplified models). In addition, the high-end models have their own set of limitations, specifically: (1) the high end models aggregate nonlinear behavior into plastic hinges; (2) they are unable to simulate column shear failure directly; (3) they neglect the strength and stiffness contributions from the gravity system; (4) they do not capture overturning effects; (5) they do not capture soil-structure interaction effects such as foundation translation and rotation, which essentially elongate the period of the building. Each of these limitations affects the accuracy of our collapse capacity predictions, however they are not expected to significantly impact the relative comparisons in which we are interested (*i.e.* *significance* and *need* of accidental torsion design requirements).

## 2.6 Summary and Recommendations

The primary goal of this study is to quantify when accidental torsion requirements are necessary in the seismic design of building structures in order to ensure adequate safety against building collapse and, conversely, to determine when such requirements may be safely omitted in the seismic design process. Like most other modern codes, ASCE/SEI 7 deals with accidental torsion by requiring the designer to consider an eccentricity in the applied lateral force, even for nominally symmetric buildings. The importance of design provisions for accidental torsion design is evaluated from two viewpoints: the *significance* of the requirements (comparing the collapse capacities of buildings that are designed with and without ASCE/SEI 7 accidental torsion provisions, as in Figure 2.8) and the *need* for the requirements (comparing collapse capacities of buildings designed without accidental torsion to those of torsionally-stiff buildings, *i.e.* perimeter frame buildings, as in Figure 2.9). The Torsional Irregularity Ratio (*TIR*) is employed to quantify the level of torsional sensitivity in the building, accounting for both asymmetry and torsional flexibility. The *TIR* is defined in ASCE/SEI 7 as the ratio of the maximum story drift at one end of the structure to the average of the story drifts at the two ends of the structure, where both drifts are computed in the same direction of interest. The drifts for computing the *TIR* include a 5% offset of the line of action for seismic forces (relative to a building's dimensions) in the most critical direction to account for accidental torsion.

This study finds that the ASCE/SEI 7 accidental torsion design requirements are only *significant* (*i.e.* affecting collapse capacity by 5% or more) for Seismic Design Category (SDC) B buildings with  $TIR > 1.4$  and for SDC D buildings with  $TIR > 1.2$ , as shown in Figure 2.8. When viewed in terms of *need*, this study found that accidental torsion design requirements are typically not needed (*i.e.*  $need < 5\%$ ) for any SDC until  $TIR > 1.4$  (see Figure 2.9), although

some buildings with shorter fundamental torsional periods or square plan layouts may develop *need* when at smaller *TIR*, *i.e.*  $1.2 < TIR < 1.4$ .

Comparing the impacts of the accidental torsion design requirements for two Seismic Design Categories, this study finds that the additional requirements in SDC D, namely the torsional amplification factor,  $A_x$ , and drift limits enforced at the building edges, successfully prevent the collapse capacity from degrading as torsional irregularity and flexibility increase (Figure 2.10). The absence of such requirements in SDC B is the primary reason that accidental torsion design requirements are less significant for SDC B as compared to SDC D buildings with large *TIR*.

The expressed goal of the ASCE/SEI 7 Standard is to provide adequate safety against structural collapse. If the ASCE/SEI 7 code provisions as a whole are assumed satisfactory for meeting this goal, then the findings of this study demonstrate that this collapse safety goal can be achieved without requiring consideration of accidental torsion in design, for SDC B buildings with a  $TIR \leq 1.4$  and for SDC D buildings with a  $TIR \leq 1.2$ . In ASCE/SEI 7, these limits correspond to the definitions of horizontal irregularity Type 1a ( $TIR > 1.2$ ) and Type 1b ( $TIR > 1.4$ ). Therefore, the findings support a proposed modification to the ASCE/SEI 7 Standard whereby the accidental torsion design provisions are only required in SDC B if the building has a Type 1b horizontal irregularity, and are only required in other Seismic Design Categories (SDC C and above) if the building has a Type 1a (or worse) horizontal irregularity. We reiterate here that even a nominally symmetric building may have a Type 1 horizontal irregularity if it is torsionally flexible. This change would eliminate the need for accidental torsion design requirements for many buildings, saving engineers the associated time needed to implement them in design, since they are not necessary for ensuring adequate building collapse safety. It could be argued that other types of accidental torsion requirements beyond the computation of an

accidental eccentricity could be employed in building design and may better predict actual seismic demands in structures due to accidental torsion. Such a change in approach to designing for accidental torsion could increase the significance of accidental torsion in design. Even so, the values of *need* obtained in this study still stand, providing little justification that such an approach is warranted for buildings with low *TIR*.

## **2.7 Acknowledgements**

This study was supported by the Federal Emergency Management Agency, through its funding of the National Institute of Building Sciences and the Building Seismic Safety Council to develop improved seismic design provisions for Seismic Design Category B. Any opinions, findings, and conclusions expressed in this paper are those of the authors and do not necessarily reflect those of the funders. The authors also acknowledge the helpful contributions from Drs. Robert Hanson and Michael Mehrain and two anonymous reviewers.

### 3 INCORPORATION OF SPATIAL CORRELATIONS BETWEEN BUILDING RESPONSE PARAMETERS IN REGIONAL SEISMIC LOSS ASSESSMENT

**ABSTRACT:** There have been a number of recent advances in probabilistic assessment of seismic-induced losses for individual buildings. However, the possible losses for a portfolio of buildings are of interest for insurance and reinsurance companies, developers, and policy makers. Probabilistic estimates of earthquake-induced losses to portfolios of buildings require quantifying correlations between losses of the different buildings comprising the building stock. This article examines spatial correlations in building seismic responses, showing that correlations are significant for closely spaced buildings (*i.e.* with site separation distances of up to 25-65 km, depending on the earthquake) and for buildings with similar first-mode periods. The results demonstrate that correlation patterns in building response parameters are closely linked to a linear ground motion intensity measure, spectral acceleration measured at buildings' first-mode periods. Based on this finding, enhancements are proposed to state-of-the-art methods for regional loss assessment to account for correlations in building response. These enhancements define a transformation between ground motion intensity and building response that preserves the expected correlation for building responses. These building responses then provide the basis for computation of earthquake-induced losses in the regional building stock.

### 3.1 Reference Article

DeBock, D.J., J.W. Garrison, K.Y. Kim, and A.B. Liel (2014a), “Incorporation of spatial correlations between building response parameters in regional seismic loss analysis.” *Bulletin of the Seismological Society of America*. In Press.

### 3.2 Introduction

During an earthquake, sites in close proximity to each other will experience ground motion time histories with similar shaking intensities, as well as similar frequency content. These similarities are due to ground motions originating from the same source, and seismic waves traveling over paths with shared geologic features. Researchers have quantified the similarities in ground shaking intensity at nearby sites by computing the correlation of ground motion intensity as a function of inter-site distance (Wesson and Perkins 2001, Wang and Takada 2005, Goda and Hong 2008b, Goda and Atkinson 2009, Jayaram and Baker 2009, Sokolov *et al.* 2010, Esposito and Iervolino 2011, Loth and Baker 2013, Du and Wang 2013), showing that closely spaced sites have correlated intensities. Precisely speaking, these correlations are computed in terms of the residual intensity, *i.e.* the difference between the ground motion intensity at a site and the mean (expected) intensity from a ground motion prediction equation or GMPE for that site (*e.g.* Boore and Atkinson 2008), such that shaking at nearby sites tends to be both higher or lower than expected for a given earthquake.

These spatial correlations in shaking intensity are important for quantifying earthquake-induced damage and losses experienced by a group of spatially-distributed buildings. This group of buildings may represent a community’s building stock, or a portfolio of privately-owned structures, and the group’s combined earthquake-related losses are referred to here as “regional losses”. Mathematically, the regional loss ( $RL$ ) experienced by a spatially-distributed portfolio of buildings in an earthquake event is a random variable that is the sum of random variables, each representing the earthquake-induced loss for the  $i^{th}$  building ( $l_i$ ):

$$RL = \sum_i l_i \quad 3.1$$

Accordingly, the expected regional loss,  $E(RL)$ , is a the sum of the expected losses for each building,  $E(l_i)$ . However, the variance of the sum depends not only on the mean of the underlying random variables, but also the variance of the underlying random variables,  $V(l_i)$ , and the correlation between these variables,  $\rho(l_i, l_j)$ . Correlation represents the degree to which the value of random variable  $l_i$  is (linearly) related to the value of random variable  $l_j$ . As shown in Equation 3.2 (Montgomery and Runger 2007), the variance of the regional loss,  $V(RL)$ , increases when the underlying random variables have greater positive correlation (or covariance):

$$V(RL) = \sum_i V(l_i) + 2 * \sum_{i < j} \sum_j \rho(l_i, l_j) * \sqrt{V(l_i) * V(l_j)} \quad 3.2$$

As may be expected from Equations 3.1 and 3.2, past research has shown that neglecting spatial correlations in ground motion intensity and, by extension, building damage, leads to underestimation of the value of rare (large) regional losses and overestimation of the value of frequent (small) regional losses (*e.g.* Bazzurro and Luco 2005, Lee and Kiremidjian 2007, Park *et al.* 2007, Goda and Hong 2008a, Jayaram and Baker 2010). In other words, regional losses have greater variance in reality than that predicted when spatial correlations are neglected.

Spatial correlations in ground motion intensity measures (*IMs*) have been studied by a number of researchers, and different models have been developed to represent regional correlations in ground motion shaking intensities (*e.g.* Wesson and Perkins 2001, Wang and Takada 2005, Goda and Hong 2008b, Goda and Atkinson 2009, Jayaram and Baker 2009, Sokolov *et al.* 2010, Esposito and Iervolino 2011, Loth and Baker 2013, Du and Wang 2013). These mathematical models predict spatial correlations between ground motion intensity residuals as a function of inter-site distance. These correlation models can then be used to

generate maps of ground motion intensities in a scenario event that have realistic spatial correlations.

This study begins by quantifying spatial correlations between building responses and describing the nature of these correlations as they relate to properties of the buildings, the building response parameter of interest, and previously observed correlations of *IM*. In this article, *IM* is quantified by spectral acceleration at a building's first-mode period,  $Sa(T_1)$ . Building response is quantified by engineering demand parameters (*EDPs*), such as story drifts and floor accelerations, which are strongly related to individual building losses. Two types of spatial correlations in building response are computed. The correlations between responses of the same building, but at different sites, are referred to as "self-correlations". These are autocorrelations (Bennett 1979). The second type, cross-correlations, represents correlation between responses of different (non-identical) buildings at different sites. Cross-correlations are important, because building stocks are typically composed of buildings with widely varying characteristics. Second, the study proposes a method to account for these correlations in building response in the context of regional seismic loss assessment. The proposed approach employs existing GMPEs and models for spatial correlations in *IM* to predict spatial distributions of building responses that have realistic correlation patterns.

### **3.3 Spatial Correlations in Building Responses**

This study quantifies building response correlations by simulating nonlinear structural response when building models are subjected to ground motion time histories from both historical and hypothetical (simulated) earthquakes. The approach is pursued because it is infeasible to compute correlations for real buildings in earthquake events due to the scarcity of response measurements from instrumented buildings.

### 3.3.1 Earthquake Scenarios and Building Simulations

Spatial correlations in building responses are investigated in four seismic events listed in Table 3.1, consisting of two historical and two hypothetical earthquake scenarios. The historical events are the 1994 Northridge (California) and 1999 Chi Chi (Taiwan) earthquakes. For each, a relatively large number of ground motion recordings are available, which were downloaded from the NGA strong motion database (Chiou *et al.* 2008). The simulated events represent two plausible Southern California earthquake scenarios: a Puente Hills fault rupture, and the “ShakeOut” rupture of the San Andreas fault. For these scenarios, Graves *et al.* (2005; 2008) modeled ground motion time histories at a large number of sites through broadband physics-based simulations of fault rupture and seismic wave propagation. The physics-based simulations produce computed ground motion time histories at a large number of closely spaced sites, making them ideal for computing spatial correlations.

Table 3.1 reports key characteristics of the earthquakes, site and ground motion time histories. In particular, note that the ground motion time histories obtained for both the recorded and simulated earthquake events depend on the site soil conditions. The range of site soil conditions for each event, quantified by the average shear-wave velocity in the top 30 meters of the soil ( $V_s^{30}$ ), is included in Table 3.1.

**Table 3.1. Earthquake events used in nonlinear time-history analyses.**

	Earthquake	Magnitude ( $M_w$ )	No. sites for which time histories are used	Min. $V_s^{30}$ (m/s)	Max. $V_s^{30}$ (m/s)	Min. PGA (g)	Max. PGA (g)	Site spacing (km)	Max. inter-site distance (km)
<b>Historical (Recorded)</b>	Northridge	6.7	157	161	2016	0.028	1.78	Irregular	275
	Chi Chi	7.6	420	124	1526	0.005	1.16	Irregular	378
<b>Hypothetical (Simulated)</b>	Puente Hills	7.2	875	165	1000	0.097	1.45	3	124
	ShakeOut	7.8	734	165	1000	0.009	1.31	10	460

To capture behavior indicative of a range of building types, building response is predicted from dynamic analysis of six building models, described in Table 3.2. The building models range in height from two to eight stories. Models represent both modern ductile and older nonductile reinforced concrete (RC) moment frame buildings and have varying strength, ductility capacity and other characteristics. A two-dimensional model of each building has been generated in *OpenSees* by Haselton *et al.* (2011) and Liel *et al.* (2011), incorporating material and geometric nonlinearities. Table 3.2 also reports first-mode periods of the buildings, which are estimated from eigenvalue analysis of the model assuming cracked concrete sections (corresponding to approximately 35-80% of the gross section, depending on axial load). In the regional seismic loss assessment that follows, each of these buildings is taken to represent a subclass of RC frames. As will be described later, variability in the structural characteristics could be considered, but is neglected in this illustration.

**Table 3.2. Building models used in nonlinear time-history analyses.**

	Building ID	No. of Stories	First-Mode Period (s)*	Ductility Capacity <sup>†</sup>
Modern (ductile)	1	2	0.60	15.0
	2	4	0.91	10.7
	3	8	1.81	6.0
Older (nonductile)	4	2	1.03	3.3
	5	4	1.92	2.3
	6	8	2.23	2.3

\*Due to the use of cracked concrete sections in the calculations, these periods are longer than those that have been measured under minor to moderate shaking (Goel and Chopra 1997). However, neither the building responses nor the correlations are highly sensitive to the estimated first-mode period of the buildings, given that the period is not grossly misestimated

<sup>†</sup> Determined by nonlinear static pushover analysis as described in FEMA (2009). There are many methods for computing ductility, so these values are provided for relative comparisons among the building models used in this study.

Each of the aforementioned building models is subjected to the ground motion time histories recorded or simulated at each site for each of the earthquake scenarios (Rowe, 2011). Nonlinear response history data is used to quantify *EDPs* including: interstory drift ratio (*IDR*),

peak floor accelerations (*PFA*), and beam and column plastic hinge rotations (*BPHR*, *CPHR*). *EDPs* have been shown to be highly correlated to damage and repair costs for buildings and building components (Porter *et al.* 2007). The *EDP* for each building at each site is defined as the maximum of that *EDP* from the separate application of the two orthogonal (horizontal) ground motion components to the 2D building model. Likewise,  $Sa(T_1)$  is computed as the geometric mean of the intensities from the two ground motion components at each site. *EDPs* are quantified as the maximum value of each parameter for all locations in the building over the entire duration of shaking. Collapse occurs when drifts increase without bounds due to lateral instability, *i.e.* sidesway collapse (Haselton *et al.* 2011). If this happens, *EDP* data are not recorded because the values are not meaningful.

### 3.3.2 Computation of Spatial Correlations in Earthquake Scenarios

Spatial correlations between ground motion intensities (quantified by  $\text{Ln}[Sa(T_1)]$ ) and between building responses (quantified by  $\text{Ln}[EDP]$ ) in each scenario are analyzed using the nonlinear time-history analysis results. Correlation coefficients,  $\rho$ , for each parameter of interest are computed as a function of inter-site distance ( $\Delta d$ ). The distance between each pair of sites is calculated from their latitude and longitude coordinates (Weisstein 2012). Data pairs from nonlinear analysis results, representing computed  $\text{Ln}[EDP]$  (or  $\text{Ln}[Sa(T_1)]$ ) values at two different sites, are binned by inter-site distance. In each bin, data pairs are separated into two vectors,  $X$  and  $Y$ , such that the vectors represent the same random variable (*e.g.*  $\text{Ln}[IDR]$ ), but computed at sites separated by a distance  $\Delta d$ . The correlation between  $X$  and  $Y$  is therefore:

$$\rho_{X,Y}(\Delta d) = \frac{E[(X-\mu_X)(Y-\mu_Y)]}{\sigma_X\sigma_Y}, \quad 3.3$$

where  $X$  and  $Y$  have mean values  $\mu_X$  and  $\mu_Y$  and standard deviations  $\sigma_X$  and  $\sigma_Y$  (Montgomery and Runger 2007). The computation of correlation coefficients is repeated for different inter-site

distances, as illustrated in Figure 3.1. Each data bin is associated with a range of inter-site distances  $d_{LB} < \Delta d < d_{UB}$ . To ensure that bins contain a sufficient number of data pairs for computing correlation coefficients, typical bin sizes (*i.e.*,  $d_{UB} - d_{LB}$ ) range from five to ten kilometers, depending on the event and number of recordings available. Correlations are computed for inter-site distances up to one third of the spatial range of the data for each earthquake event, according to standard geostatistical practice (David 1977). Similar trends would be observed if semivariograms, rather than correlations were used to analyze the spatial variability in the data (Houlding 2000).

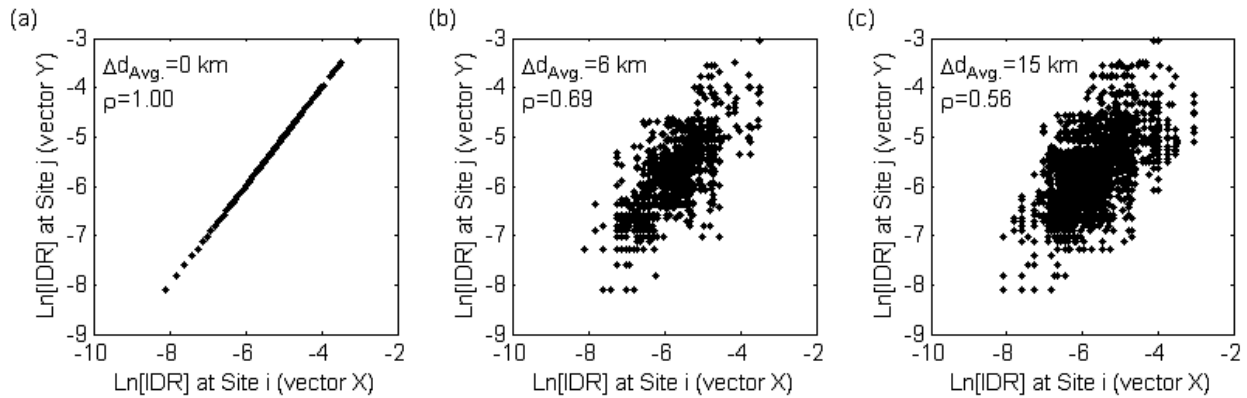


**Figure 3.1. Building 1 vs. Building 1 responses, quantified by  $\text{Ln}[IDR]$ , for the Chi Chi earthquake at sites with inter-site distances of  $\Delta d$ .**

### 3.3.2.1 Non-Stationarity of the Spatial Correlation Computations

The correlations computed in this study illustrate spatial trends in building responses. However, the correlations are fundamentally different from those of previous studies, in that they are computed for absolute values of  $\text{Ln}[Sa(T_1)]$  and  $\text{Ln}[EDP]$ , rather than for their residuals. This difference is illustrated in Figure 3.2, which displays spatial correlations in absolute  $IM$  computed for the Chi Chi earthquake using four different methods. In the first case, correlations are computed from the  $IMs$  recorded in the earthquake. In the second case, correlations are computed by combining expected  $IMs$  from the Boore and Atkinson (2008) GMPE with

residuals predicted using the Loth and Baker (2013) spatial correlation model. The third case is similar to the second, except the residuals are random and uncorrelated. In the fourth, the GMPE is combined with perfectly correlated residuals. Loth and Baker (2013) estimate that spatial correlations of residual  $IM$  are negligible at a distance of 35 km. However, the situation is clearly different for correlations in absolute  $IM$  in Figure 3.2, which shows a correlation of 0.4 at 35 km.

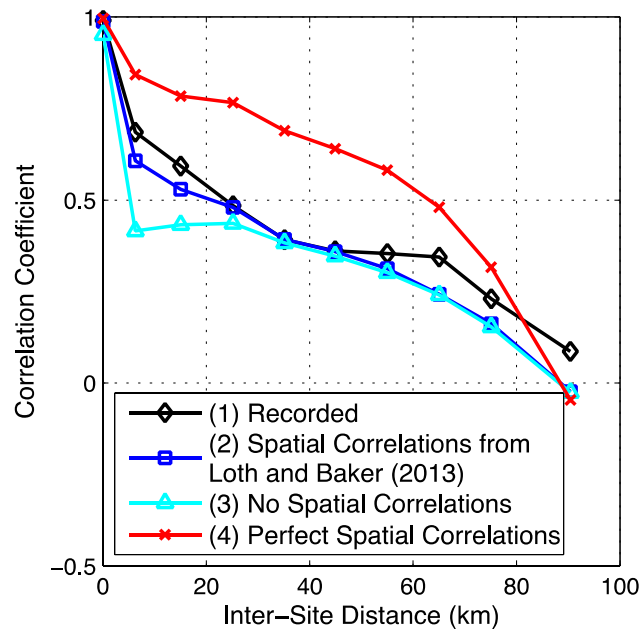


**Figure 3.2. Spatial correlations of  $IM = Ln[Sa(T_1=0.60 s)]$  computed for the Chi Chi earthquake through four different methods, the details of which are described in the text. All of the correlations shown are in terms of *absolute* rather than *residual*  $IM$  quantities.**

Computing the spatial correlations from absolute rather than residual quantities introduces important limitations. In particular, Equation 3.3 assumes second-order stationarity, that is that correlations are independent of (1) location, *i.e.* the position of sites  $i$  and  $j$  relative to the fault rupture and (2) direction, *i.e.* the orientation of the vector describing the distance between  $i$  and  $j$  relative to a reference coordinate system (Goovaerts 1997). However, Garrison (2012) showed that correlations computed from absolute quantities of  $Ln[Sa(T_1)]$  and  $Ln[EDP]$

depend on the location and orientation of the two sites relative to the fault and the size of the sample region because of their sensitivity to the intensity of shaking and proximity to the fault. As a result, the random variables of interest here are non-stationary.

The quantification of correlation in building response parameters is based on the absolute *EDPs* rather than residual quantities, because computing *EDP* residuals would require *EDP*-equivalents to GMPEs to predict *EDPs* as a function of location and building characteristics, which are not part of current earthquake engineering practice. In addition, the article shows later that unbiased predictions of *EDPs* can be computed from existing models for  $Sa(T_1)$ , based on these observations of correlation of absolute quantities, and without the need for *EDP* prediction equations. Although comparisons of correlations computed between one earthquake and another should be made with caution due to the non-stationarity, comparisons of spatial correlations computed for same event are insensitive to region size and locations.

### **3.3.3 Patterns of Spatial Correlations**

Self-correlations and cross-correlations of *EDP* are computed for each of the buildings and earthquake scenarios of interest, generating results like those shown in Figure 3.3. These correlations reflect similarities in the intensity of ground shaking, as well as similarities in building properties. Due to the strong spatial nature of correlations in the ground motion intensity, results consistently show a decrease in correlation as the site separation distance increases, but the pattern differs depending on the buildings and earthquake scenario under consideration.

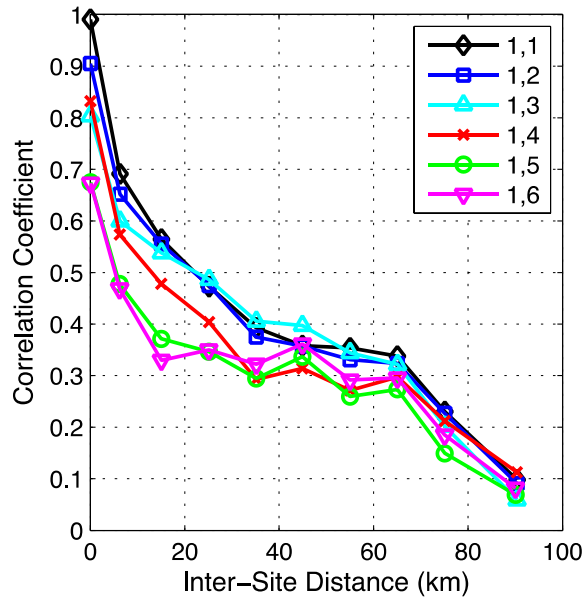


**Figure 3.3. Correlations of  $\ln[IDR]$  for Building 1 and Building  $j$  (denoted 1,  $j$ ) for the Chi Chi earthquake.**

### 3.3.3.1 Effect of Building Characteristics

Figure 3.3 displays spatial correlation patterns representing both self-correlations and cross-correlations. The results show that the same spatial correlation patterns that are present in self-correlations (the line labeled 1,1) are also observed among cross-correlations of non-identical buildings. As may be expected, the results indicate that responses of more similar buildings are more highly correlated than those of more dissimilar buildings. Looking at the entire range of inter-site distances, cross-correlations between the responses of Building 1 and the responses of Buildings 2 and 3 (the other two ductile buildings) are very similar to Building 1's self-correlations. Cross-correlations between buildings with very different ductility capacities (*e.g.* Building 1 compared to Buildings 4-6) are lower than cross-correlations between buildings with more similar nonlinear deformation characteristics. Moreover, cross-correlations are also higher for buildings with more similar first-mode periods (*e.g.* Buildings 1 and 4) than those with very different periods (*e.g.* Buildings 1 and 5). The trends show that similarities in both period

and ductility capacity impact cross-correlations, although period seems to be the more important factor. In addition, correlations for longer period buildings are slightly larger than for shorter period buildings, because high frequency seismic waves tend to scatter more than low frequency waves (Der Kiureghian 1996).

### 3.3.3.2 *Effect of Earthquake Event Characteristics*

Trends in spatial correlations in building response parameters also depend on a number of characteristics of the earthquake scenario, as made apparent in Figure 3.4. In particular, the larger magnitude events (ShakeOut and Chi Chi) produce positive correlations in building response for larger inter-site distances. Figure 3.5 depicts why this occurs: the larger magnitude ShakeOut event produces larger isoseismic zones as compared to the smaller magnitude Northridge event, such that greater correlations in responses are observed across longer distances. Spatial correlations of absolute measures of response, as in Figure 3.4, are also impacted by spatial correlations of site conditions, quantified here by the  $V_s^{30}$  parameter. Specifically, earthquake scenarios with larger correlation of site  $V_s^{30}$  have higher correlations among response parameters, as expected. For the regions considered in this study, spatial correlations of  $V_s^{30}$  become negligible at inter-site distances of 5-25 km. Du and Wang (2013) observed that spatial correlations of residuals are also impacted by spatial correlations of  $V_s^{30}$ .

Some of the differences in correlation patterns between events can also be attributed to the methods used in computing building responses and correlations. It is worth considering, for example, that the simulated nature of the ground motion data for the ShakeOut and Puente Hills earthquakes may affect the results of a spatial correlation analysis. In fact, the authors found that spatial correlations of ground motion intensity residuals for the simulated events are for the most part larger than those predicted by correlation models developed from historical events. This

observation is consistent with Baker and Jayaram (2007)'s study of the Puente Hills simulation, which attributed the correlation bias to excessively correlated ground motion time histories at soft-soil sites. Star et al. (2011) showed that the residual terms in ground motion intensity agree with historical events, provided that the GMPE predictions attenuate at the same rate as the simulated ground motion intensities.

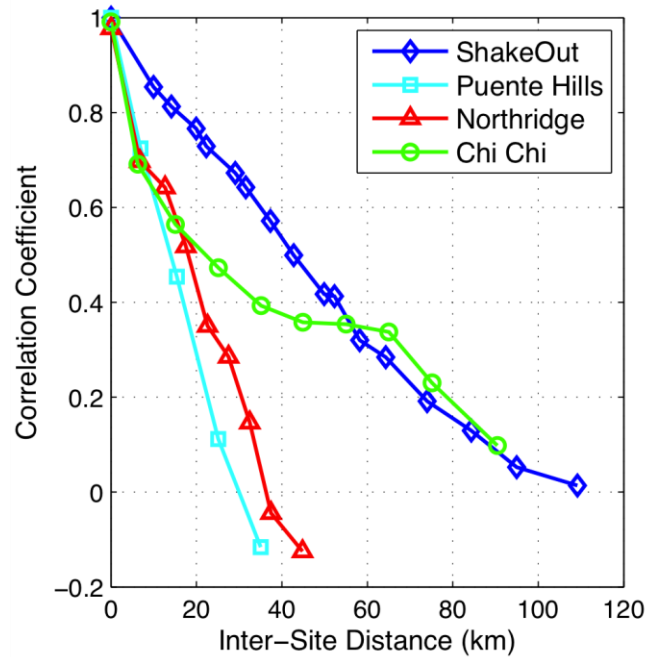


**Figure 3.4. Self-correlations of  $\ln[IDR]$  for Building 1 for the four different earthquake scenarios.**

Moreover, the variability in spatial correlation patterns for the different earthquake events is an indicator of the non-stationarity of the spatial correlations computed based on absolute, rather than residual, response quantities. For example, the negative correlations that are observed at moderate inter-site distances in the Puente Hills and Northridge earthquakes are due to the size of the affected area and the locations of the sites; for these scenarios, many of the site pairs that are spaced more than 50 kilometers apart have one site near to and one far from the fault rupture, such that the pair will consist of one large and one small response, producing a negative

correlation and violating stationarity. The sensitivity of the correlations to the size of the event (shown in Figure 3.5) result from using absolute response quantities in correlation computations.

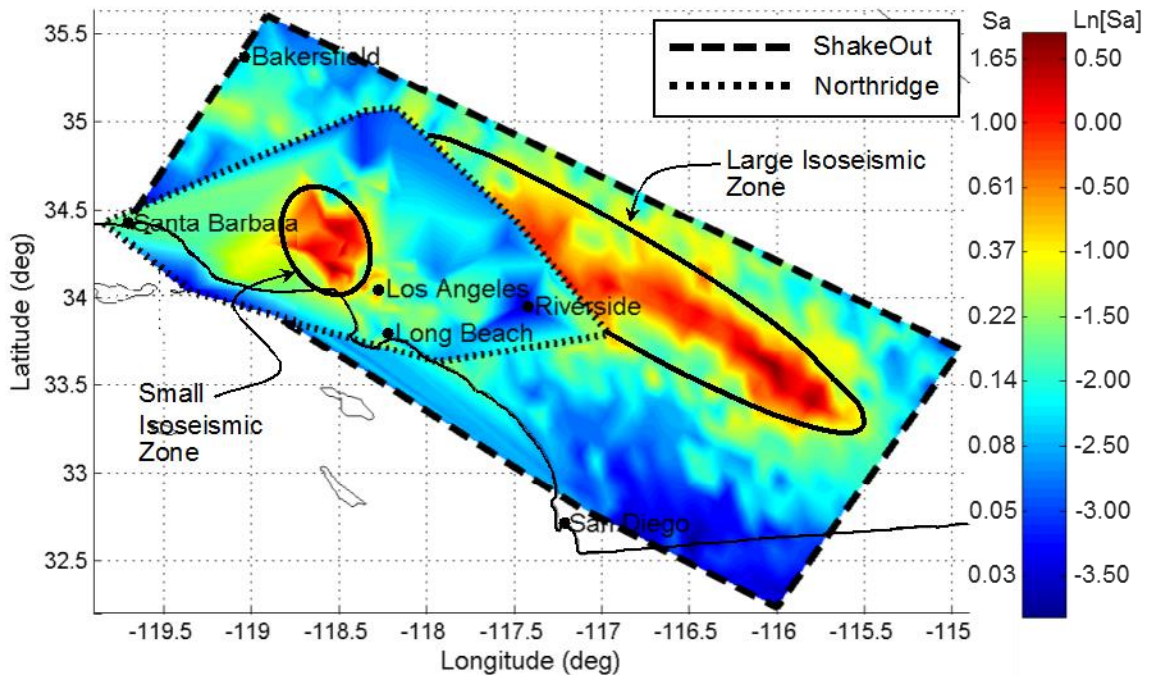


**Figure 3.5.** Map of ground motion intensities (“Intensity map”), quantified by  $Sa(T_1=0.6\text{ s})$  and  $\text{Ln}[Sa(T_1=0.6\text{ s})]$ , for the ShakeOut and Northridge earthquakes. Areas with high ground motion intensity are circled.

### 3.3.4 Sources of Spatial Correlations

A central question pertaining to correlations in building response relates to the sources of the correlation: are correlations explained by spatial correlations in ground motion intensity, other characteristics of the ground motion (*e.g.* duration, frequency content, *etc.*), characteristics of the building, geology and site conditions, or a combination of these? To examine this question, Figure 3.6 compares correlations in building response to correlations of  $\text{Ln}[Sa(T_1)]$ , where  $Sa(T_1)$  is computed directly from a ground motion time history. In particular, Figure 3.6, shows the striking similarity in correlations of building response parameters,  $\text{Ln}[EDP]$ , to correlations of  $IM$ ,  $\text{Ln}[Sa(T_1)]$ . Spatial correlations and cross-correlations for  $\text{Ln}[Sa(T_1)]$  and for  $\text{Ln}[IDR]$  are similar to one another in every case observed in this study, even for quite dissimilar

buildings. For other *EDPs*, the results also showed that  $Ln[EDP]s$  had remarkably similar correlation patterns to  $Ln[Sa(T_1)]$ . Figure 3.6(d) shows an exceptional case, in which cross-correlations for *EDPs* other than *IDR* are quite different from the correlations in  $Ln[Sa(T_1)]$ . This exception was observed only for a few buildings, in the simulated events, as in Figure 3.6(d).

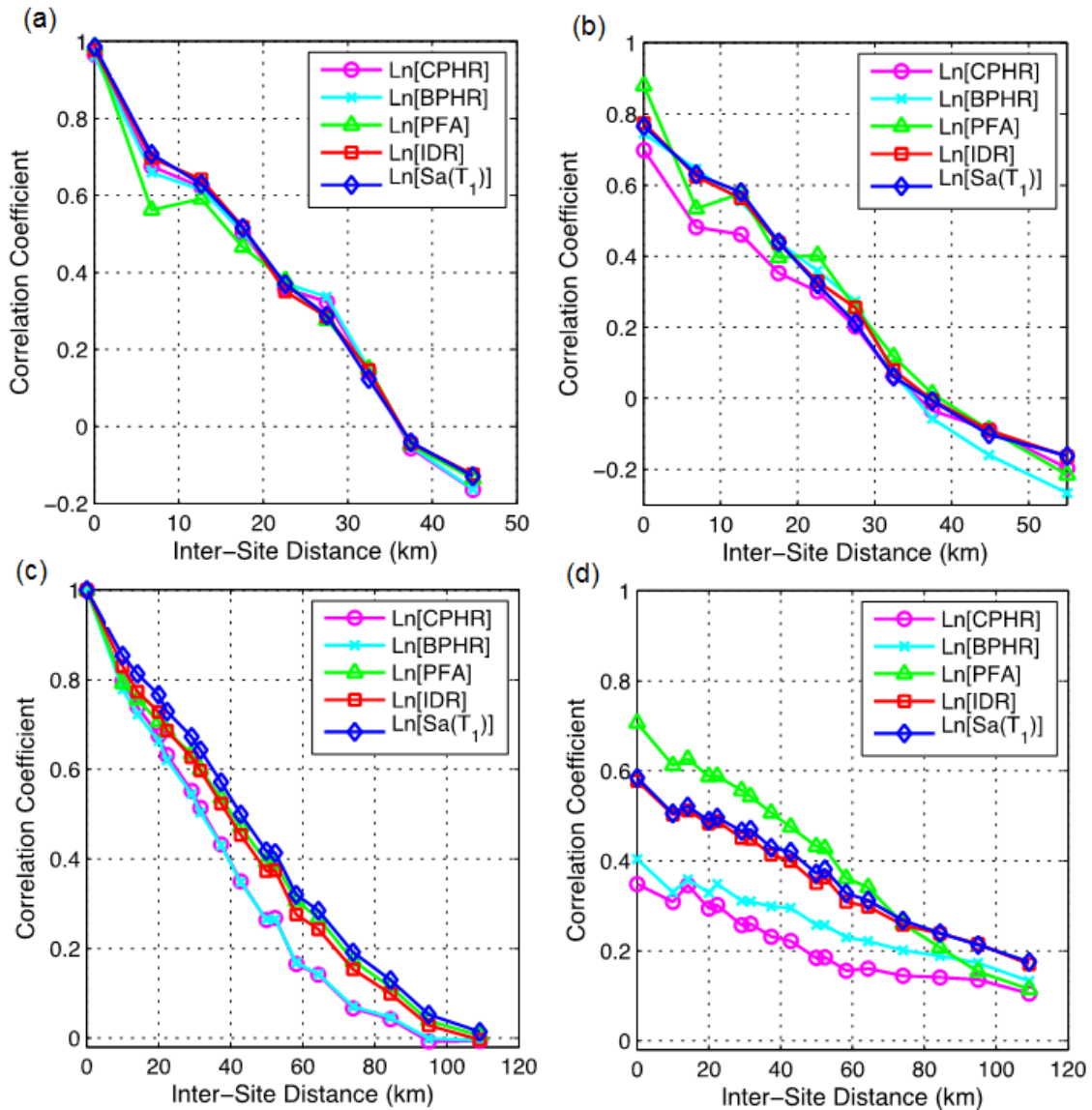


Figure 3.6. Spatial correlations between ground motion intensity measures ( $Ln[Sa(T_1)]$ ) and building response parameters ( $Ln[IDR]$ ,  $Ln[PFA]$ ,  $Ln[BPHR]$  and  $Ln[CPHR]$ ) in the Northridge earthquake for: (a) self-correlations for Building 1 and (b) cross-correlations between Buildings 1 and 6, and in the Shakeout earthquake for: (c) self-correlations for Building 1 and (d) cross-correlations between Buildings 1 and 6.

The observation that the correlations between  $\ln[Sa(T_1)]$  and  $\ln[EDP]$  are similar is important. In particular, it suggests that the ground motion intensity at a site, paired with a single building property, the first-mode period, provides critical insight into spatial correlations in response. The correlations in  $\ln[Sa(T_1)]$  at the two different periods are good predictors of the correlations in building response even in the case of cross-correlations. Correlation patterns are generally similar regardless of which  $EDP$  is used to quantify building response.

The importance of correlations in  $\ln[Sa(T_1)]$  in explaining correlations in  $\ln[EDP]$  provides the basis for proposals to improve the regional loss assessment methodology, which is described in the second part of the paper.

### **3.4 Including Correlations in Building Responses in Regional seismic Loss Assessment**

#### **3.4.1 Regional Seismic Loss Assessment Methods**

The goal of regional loss assessment is to quantify the distribution of seismic-induced losses a spatially-distributed portfolio of buildings or infrastructure may experience. State-of-the-art methods for loss assessment typically proceed by predicting losses for the region in a number of possible scenario earthquakes. The losses computed for each scenario are weighted by the likelihood of that scenario occurring to compute the likelihood of experiencing a particular level of losses over time. These assessments rely heavily on Monte Carlo-based simulation methods, which are used to generate a set of realizations of a random variable, or set of random variables, that are consistent with predefined probability distributions (Fishmen 2006). Other researchers (*e.g.* Crowley and Bommer 2006) have demonstrated that such methods are superior to those that perform probabilistic loss analysis separately for each building in the portfolio and then sum the obtained loss distributions.

This study considers a regional seismic loss assessment method with the following steps:

1. Generate a set of possible future earthquake scenarios that are consistent with assumed seismic sources and seismological models.
2. For each scenario, compute the expected value and standard deviation of the ground motion intensity ( $IM$ ) at each building site in the region using one or more GMPEs.
3. Generate a realization of the residual  $IMs$  at each site with Monte Carlo simulation. At this stage, spatial correlations of  $IM$  residuals can be considered if the residuals are represented as jointly distributed. The sum of the residual  $IM$  and the expected  $IM$  (Step 2) provides a predicted  $IM$  value for each site (*i.e.* a map of ground motion intensities for the scenario).
4. Estimate dollar losses for every building in the region, based on the mapped intensity at each building's location. Losses are typically estimated with what is referred to here as an  $IM$ -based vulnerability function (VF), which defines the relationship between  $IM$  and the expected damage factor for a particular building type. The damage factor expresses the loss as a fraction of the total replacement cost of the building (*e.g.* ATC 1985). VFs are predefined based on gross building characteristics (*e.g.* height, structural system, occupancy *etc.*).
5. Sum the losses from each building (Step 4) to compute the losses for the group of buildings.
6. Repeat Steps 2-5 for additional realizations of the same scenario event, and for other events. The losses predicted can then be used to estimate mean annual frequencies of exceeding different levels of regional loss.

Improved representation of building response correlations can be incorporated in the regional loss assessment. Specifically, we propose to split Step 4 into two parts:

- 4a. Develop spatial distributions of  $EDPs$  that are probabilistically consistent with observed patterns of correlations in building response. *The remainder of this paper is dedicated to*

*developing a methodology for developing these spatial distributions.*

- 4b. Estimate losses as a function of *EDP* for each building. These loss predictions employ *EDP*-based VFs. The *EDP*-based VFs are similar to *IM*-based VFs, but predict loss for a building from a maximum building response, *i.e.* *EDP*, rather than directly from an *IM*.

The revisions to Step 4 improve regional seismic loss assessment for two reasons. First, Step 4a ensures that the proposed method directly considers spatial correlations in building response in a probabilistically robust manner. Secondly, Step 4b is expected to improve loss predictions, because *EDPs* are better predictors of structural loss and damage than  $Sa(T_1)$ . Methods for estimating seismic-induced losses to individual buildings increasingly rely on *EDPs* to predict damage and losses (*e.g.* Ramirez and Miranda 2009).

### **3.4.2 Simulating EDPs as Spatially Correlated Fields**

#### *3.4.2.1 Spatial Correlations based on a Linear Transformation between IM and EDP*

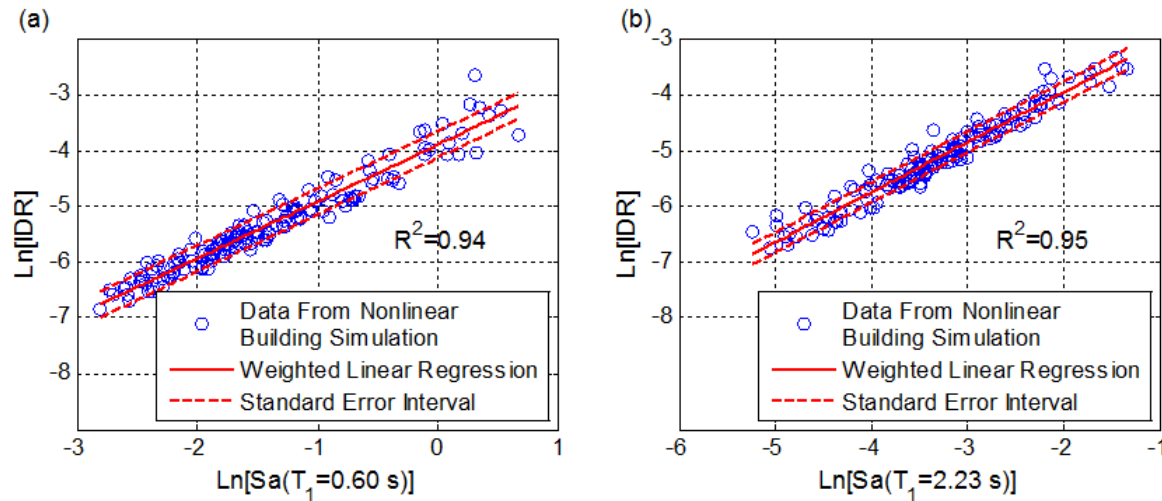
The findings presented previously suggest that spatial correlations of  $\text{Ln}[EDP]$  and of  $\text{Ln}[Sa(T_1)]$  have similar patterns. These similarities may be indicative of an underlying mathematical relationship between  $\text{Ln}[Sa(T_1)]$  and  $\text{Ln}[EDP]$ . To explore this relationship, Figure 3.7 shows the results of a weighted least-squares linear regression between  $\text{Ln}[Sa(T_1)]$  and  $\text{Ln}[IDR]$ , where  $\text{Ln}[Sa(T_1)]$  is the independent variable, for the Northridge ground motions. Large *IDR* values, indicative of highly nonlinear response, occurred less frequently than smaller *IDRs*, and are therefore assigned higher weights in the regression to compensate for having fewer data points in that range. Collapse cases are excluded from the regression.

Figure 3.7 reveals that the relationships between  $\text{Ln}[Sa(T_1)]$  and  $\text{Ln}[IDR]$  are highly linear. Goodness-of-fit is quantified by the coefficient of determination ( $R^2$ ), which represents the fraction of the total variance that is captured by the linear regression model.  $R^2$  values close

to 1 indicate that most of the variance of  $\text{Ln}[IDR]$  is explained by the linear relationship with  $\text{Ln}[Sa(T_1)]$ . Although not presented here, relationships between  $\text{Ln}[Sa(T_1)]$  and  $\text{Ln}[EDP]$  for the other buildings, earthquakes, and  $EDP$  measures, such as  $PFA$ , are found to be highly linear as well, but typically have lower  $R^2$  values for  $EDPs$  other than  $IDR$ . These linear relationships (hereafter “ $IM$ - $EDP$  transformations”) are of the form

$$\text{Ln}[EDP] = A + B * \text{Ln}[Sa(T_1)] \quad 3.4$$

which leads to a nonlinear functional form in non-log space of  $EDP = a * Sa(T_1)^b$ . Cornell (2002) and others have previously fit the same functional form to  $IM$  and  $EDP$  data.



**Figure 3.7.** Weighted least-squares linear regression of  $\text{Ln}[IDR]$  with  $\text{Ln}[Sa(T_1)]$ , based on nonlinear analysis results from building models subjected to the Northridge ground motions for: (a) Building 1 and (b) Building 6 (non-collapse cases only). The standard error interval defines the range in which 68% of the  $EDP$  values are expected to fall (*i.e.*  $\pm 1$  standard deviation).

It is easily shown that two variables that are linearly related, as in Equation 3.4, have identical autocorrelation patterns. Therefore,  $EDPs$  estimated based on a linear  $IM$ - $EDP$  transformation will have identical correlations to those of  $\text{Ln}[Sa(T_1)]$ . The similarity in the spatial correlations of  $\text{Ln}[Sa(T_1)]$  and of  $\text{Ln}[EDP]$  thus obtained is appropriate given the strong resemblance between the two, as observed in Figure 6.

### 3.4.2.2 EDP Estimation Using the Linear IM-EDP Transformation

This article proposes to predict *EDPs* from linear *IM-EDP* transformations (Equation 3.4) for the purpose of regional loss assessment (*i.e.* Step 4a). This approach requires the analyst to first generate region-wide values of  $Sa(T_1)$  (intensity maps) using GMPE(s) and already developed spatial correlation models for *IM* (*e.g.* Loth and Baker 2013); these maps represent the completion of Steps 1-4 described above. Then, *EDPs* are predicted at each site, based on an established linear relationship between  $Ln[Sa(T_1)]$  and  $Ln[EDP]$  for a given building type, generating a map of predicted *EDP* values (*i.e.* “*EDP* map”) that represents the *EDPs* in each building in the portfolio. The predicted building responses are denoted  $Ln[\widehat{EDP}]$ . This linear transformation accomplishes two goals. First, it preserves the similarities in spatial correlation structures of  $Ln[Sa(T_1)]$  and  $Ln[EDP]$  by implying that the correlation structures of  $Ln[EDP]$  and  $Ln[Sa(T_1)]$  are, in fact, identical. Second, it can be shown to lead to predictions of  $Ln[\widehat{EDP}]$  that are unbiased with regard to  $Ln[Sa(T_1)]$ , as discussed below.

In order to examine the implications of the linear transformation (Equation 3.4) for regional loss assessment, we focus on the results of nonlinear simulation for Building 6 (similar findings are also observed for the other buildings). Consider the distribution of ground motion intensities recorded in the Northridge earthquake shown in Figure 3.8(a), quantified by  $Sa(T_1)$  where  $T_1$  is the first-mode period of Building 6. If Building 6 responses are predicted from a linear *IM-EDP* transformation, provided in Figure 3.7(b), an *EDP* map is computed, as shown in Figure 3.8(b) (assuming Building 6 is located at every site in the region). The spatial distribution of  $Ln[Sa(T_1)]$  shown in Figure 3.8(a), and the corresponding predicted spatial distribution of  $Ln[\widehat{EDP}]$  shown in Figure 3.8(b), which is a linear transformation of  $Ln[Sa(T_1)]$  at each site, would not actually occur simultaneously, due to uncertainties in the *IM-EDP* prediction.

However, because of their identical spatial correlation structures, the likelihood of the spatial distribution of  $\text{Ln}[\widehat{EDP}]$  occurring for a given earthquake scenario is equal to the likelihood of the spatial distribution of  $\text{Ln}[Sa(T_1)]$  occurring if the *IM-EDP* transformation is unbiased.

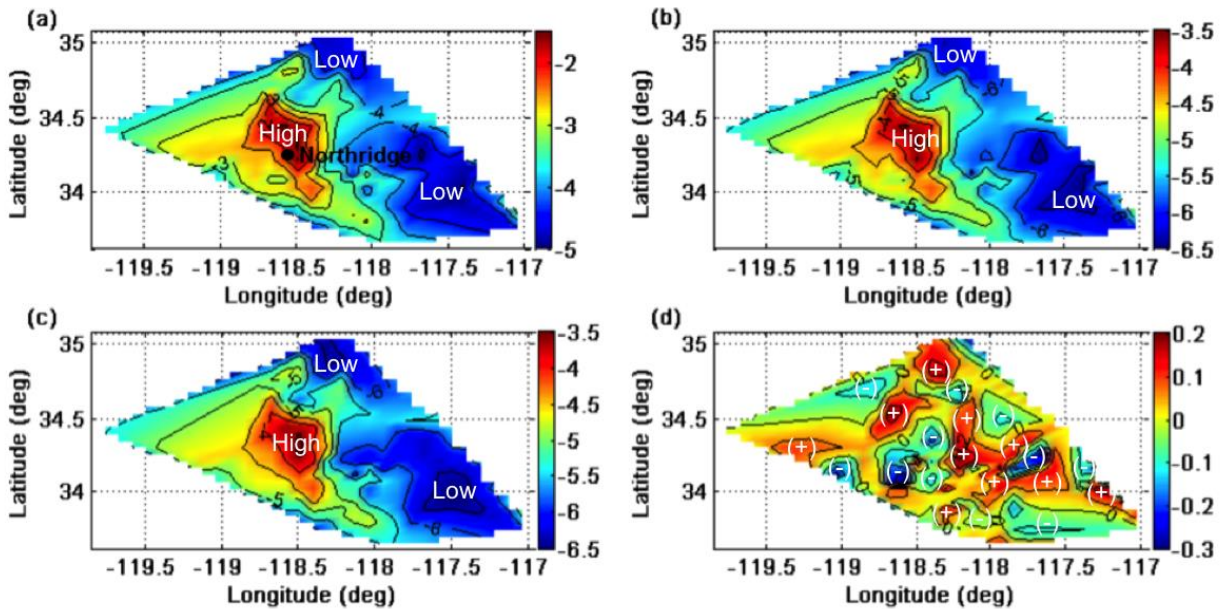


**Figure 3.8.** Intensity and *EDP* maps for the Northridge earthquake showing (a)  $\text{Ln}[Sa(T_1)]$  (units  $\text{Ln}[g]$ ), (b)  $\text{Ln}[\widehat{IDR}]$  for Building 6 as predicted from the fitted linear *IM-EDP* transformation, (c)  $\text{Ln}[IDR]$  as observed in nonlinear time-history analysis of Building 6, and (d) the residual differences between the predicted and observed  $\text{Ln}[IDR]$  values, i.e.  $\text{Ln}[IDR] - \text{Ln}[\widehat{IDR}]$ .

An unbiased *IM-EDP* transformation requires that the differences between the predicted *EDPs*, i.e.  $\text{Ln}[\widehat{EDP}]$ , and the observed *EDPs*, i.e.  $\text{Ln}[EDP]$ , are non-systematic. The observed *EDPs*, obtained through nonlinear dynamic analysis of the model of Building 6 on being subjected to the Northridge ground motions, are shown in Figure 3.8(c). The differences between the observed  $\text{Ln}[EDP]$  and predicted  $\text{Ln}[\widehat{EDP}]$  are mapped in Figure 3.8(d). The spatial distribution of the residuals appears to be non-systematic. This visual observation is supported by examining the results of regression analysis (Figure 3.7) to show that the residual differences between the observed and predicted *IDRs* are homoscedastic and normally distributed. Figure 3.9 further supports the observation that the distribution of the residuals is non-systematic by

showing that spatial autocorrelations of the residuals are less than 0.2 for all non-zero inter-site distances.

Since the residual differences between  $\text{Ln}[\widehat{EDP}]$  and  $\text{Ln}[EDP]$  are non-systematic, the proposed method proceeds by converting a spatial distribution of  $\text{Ln}[Sa(T_1)]$  to  $\text{Ln}[\widehat{EDP}]$  through a linear *IM-EDP* transformation that preserves spatial correlations. This approach circumvents the need to develop *EDP* prediction equations and a correlation model for their residuals, because the  $\text{Ln}[\widehat{EDP}]$ s so obtained are unbiased, and robust models have already been developed for generating intensity maps that consider spatial correlations of residuals.

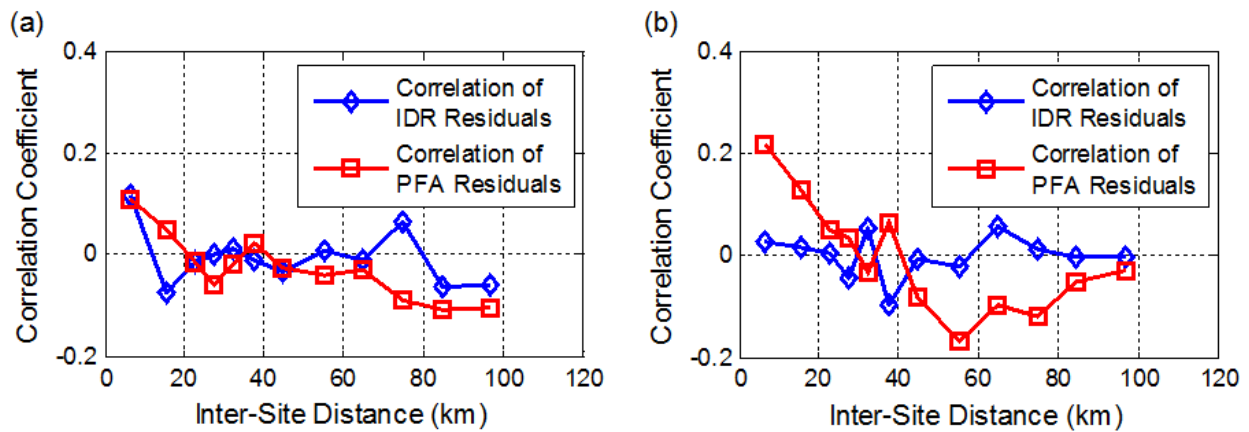


Figure 3.9. Spatial autocorrelations of the standardized residual differences between the predicted and observed  $\text{Ln}[EDP]$  values ( $\text{Ln}[EDP] - \text{Ln}[\widehat{EDP}]$ ) using the Northridge results for (a) Building 1 and (b) Building 6.

### 3.4.3 Importance of the IM-EDP Transformations

Given the similarity in spatial correlation patterns observed between  $\text{Ln}[Sa(T_1)]$  and  $\text{Ln}[EDP]$ , it is tempting to conclude that loss assessment methods that appropriately consider spatial correlations solely in ground motion intensity would provide good estimations of building response. However, the linear *IM-EDP* transformation is needed to preserve spatial correlations in building response, even in this case.

Consider, for example, a method that considers spatial correlations in ground motion intensity, but not in building response. Equation 3.5 computes the losses at each site, employing an *IM*-based *VF*.

$$l_i = VF(IM_i) \quad 3.5$$

Equation 3.5 essentially has a built-in relationship between *IM* and *EDP*. If the built-in relationship between *IM* and *EDP* happens to be linear, then the correlation of *EDPs* is preserved, if the equation is applied deterministically at every site. However, no variation in the *IM-EDP* relationship is considered, leading to underestimation in the variance of the losses. On the other hand, if the application of Equation 3.5 considers uncertainty in the *VF*, and uncertainty of the *IM-EDP* relationship by extension, randomness is introduced and the spatial correlations of *EDPs* are artificially reduced.

To preserve the correlation and the variance in *EDPs* and losses, this article proposes a method to generate *IM-EDP* transformations such that losses are computed as:

$$l_i = VF(\widehat{EDP}_i) \quad 3.6$$

$\widehat{EDP}$  is obtained from a linear *IM-EDP* transformation, preserving correlation. At the same time, the coefficients defining the *IM-EDP* transformation are randomized (from one event to the next) such that variability in *IM-EDP* transformations (and, by extension, regional loss) is reasonable.

### 3.4.4 Variability in Transformation Between IMs and EDPs

#### 3.4.4.1 Sensitivity of *IM-EDP* Transformation to Ground Motion Characteristics

For a given building, the intercept and slope coefficients defining the linear *IM-EDP* transformation depend on the characteristics of the ground motions used to develop the relationship. To quantify the variability in these coefficients for a selected building model,

incremental dynamic analysis (IDA) is carried out with a set of ground motion time histories that differ significantly in terms of frequency content and other characteristics. IDA is conducted by analyzing the response of the structure under a ground motion of interest. Then, the ground motion is scaled to larger intensities, each time analyzing the structure and simulating *EDPs* and recording its response, and repeating this process for higher ground motion intensities until collapse occurs (Vamvatsikos and Cornell, 2002).

Example IDA results for Building 6, and the implications in terms of variability of the *IM-EDP* transformation for a single building, are shown in Figure 3.10. For purposes of illustration, the ground motions used in this example are the FEMA (2009) far-field ground motion set, which is comprised of 22 pairs of ground motions. Each curve in Figure 3.10(a) is the result of IDA for a single record, which has unique frequency content, duration, and other characteristics, scaled to different levels. As a result, each of the records leads to a distinct *IM-EDP* transformation, as shown by the *IM-EDP* transformations fitted separately to individual IDA analyses in Figure 3.10(b). Results from the Northridge earthquake (from Figure 3.7) have been overlaid on Figure 3.10(b), showing that the observed linear relationship between  $\ln[IDR]$  and  $\ln[Sa(T_1)]$  for the Northridge scenario lies within the range of transformations obtained with the general ground motion set. Recall that the Northridge scenario includes results from ground shaking at 245 sites, each with unique ground motion time histories, but from the same earthquake.

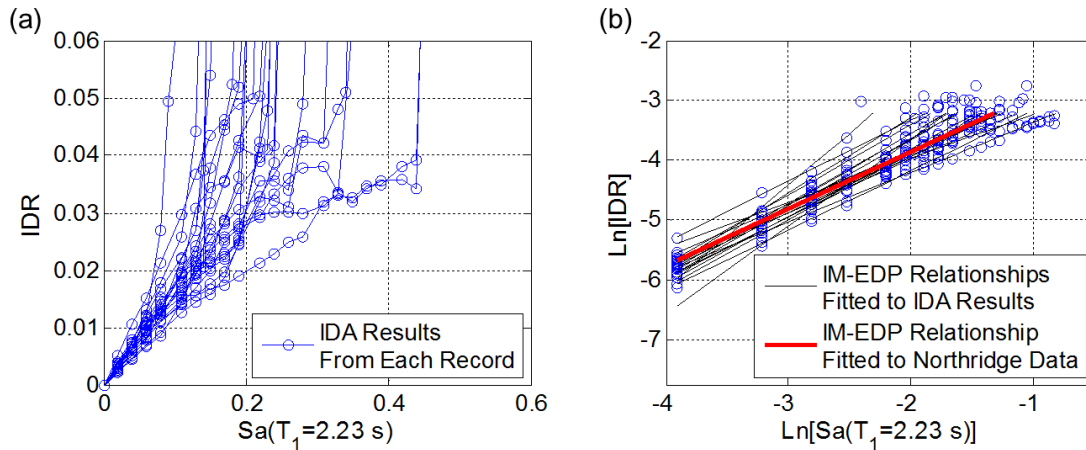


**Figure 3.10.** (a) *IDA* results in terms of *IDR* vs.  $Sa(T_1)$  for Building 6, and (b) the same results recast as  $\text{Ln}[IDR]$  vs.  $\text{Ln}[Sa(T_1)]$ , showing the fitted *IM-EDP* transformations for each record as compared to the Northridge *IM-EDP* transformation.

The *IM-EDP* relationships can be defined by the intercept and slope coefficients defining the fitted line (denoted  $A$  and  $B$ , as in Equation 3.4). The values of the intercept and slope coefficients extracted from results in Figure 3.10(b) are plotted in Figure 3.11. By observation,  $A$  and  $B$  are clearly related. In fact, the Henze-Zirkler (1990) and Royston (1983) multivariate normality tests show that  $A$  and  $B$  follow a multivariate normal distribution. Since the true *IM-EDP* transformation for a future earthquake is uncertain, Monte Carlo simulation can be used to sample intercept and slope coefficients, based on the multivariate normal distribution. The parameters defining the multivariate normal distribution, including the means of the coefficients,  $\mu_A$  and  $\mu_B$ , and their covariance matrix,  $COV(A,B)$ , are computed from *IDA* results. This process is illustrated for Building 6 in Figure 3.11, for which  $A$  and  $B$  are sampled randomly 100 times to define coefficients for possible *IM-EDP* transformations.

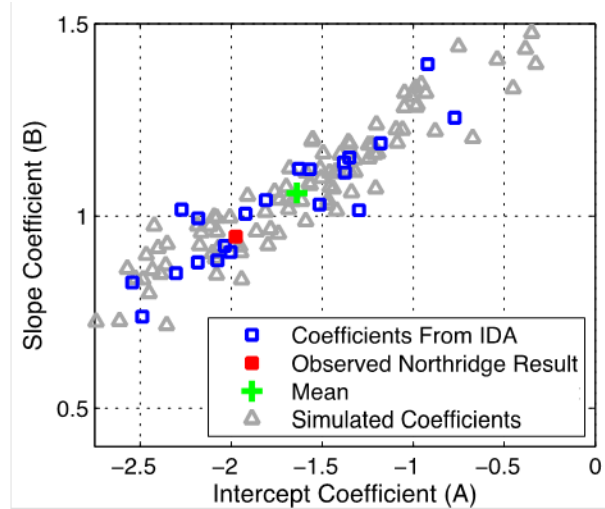


**Figure 3.11. Observed and sampled intercept and slope coefficients of *IM-EDP* relationships for Building 6.**

The strong correlation between intercept and slope coefficients for *IM-EDP* transformations is due to the intercept (*A*) being extrapolated using the slope (*B*), as can be seen in Figure 3.10(b). Since the y-axis of the coordinate system does not pass through the data, the intercept coefficient is highly sensitive to the value of the slope coefficient. By introducing a third term, *C*, Equation 3.4 can be re-written:

$$\ln[EDP] = A + B * (\ln[Sa(T_1)] + C) \quad 3.7$$

In Equation 3.7, the addition of the variable *C* is analogous to translating the coordinate system so that the y-axis passes through a location  $x=-C$ . Therefore, there is no longer a need to extrapolate the intercept coefficient from data that lie far away from the y-axis. Optimizing the variable *C* such that the intercept and slope coefficients have zero correlation results in values of *C* ranging from  $-3.5 < C < -1.0$  for the different buildings in this study. *IM-EDP* transformations of the form shown in Equation 3.7 would be advantageous for cases in which the analyst desires to generate slope and intercept coefficients independently, however, it requires that the variable *C* be determined through optimization.

#### 3.4.4.2 Effect of $\varepsilon$ on Structural Response EDPs

The method described in the previous section for randomly generating coefficients to define *IM-EDP* transformations neglects the impacts of spectral shape on *IM-EDP* transformations. It is well established that, among ground motion records with the same  $Sa(T_1)$ , variation in spectral shape may lead to significant differences in structural response. We now examine the effects of spectral shape on *EDPs*, with the goal of modifying the procedure for sampling coefficients to define the *IM-EDP* transformations.

The residual *IM* can be quantified by the number of standard deviations between the expected *IM* from a GMPE and the observed site *IM*, producing a parameter referred to as epsilon.  $\varepsilon$  is a proxy for spectral shape and depends on the period of interest,  $T$ . Large positive  $\varepsilon$  indicate that the spectral acceleration at period  $T$  is significantly larger than the expected value. These positive  $\varepsilon$  generally correspond to peaks in the acceleration spectrum, because it is unlikely that spectral accelerations at all other periods are also significantly larger than their expected values (Baker and Cornell 2005). The relationship between  $\varepsilon$  and spectral shape is illustrated in Figure 3.12, in which the record with positive  $\varepsilon(T_1=1s)$  has relatively lower spectral accelerations for  $T \neq T_1$  than a record with negative  $\varepsilon(T_1=1s)$ , but the same  $Sa(T_1=1s) = 1.0g$ . Nonlinear multi-degree-of-freedom buildings are sensitive to ground motion intensity at a range of periods, so the record with the greater positive  $\varepsilon$  tends to induce smaller *EDPs*, because it has smaller spectral accelerations at periods other than  $T_1$  (Baker and Cornell 2005; Haselton *et al.* 2011).

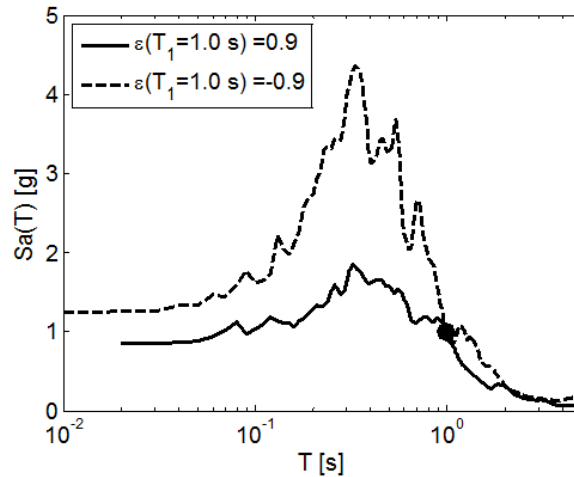


Figure 3.12. Acceleration spectra for two records, both with  $Sa(T_1=1.0\text{ s})=1.0\text{g}$ .

Figure 3.13 depicts the relationship between the  $\varepsilon$  of each of the ground motions in the FEMA record set (evaluated for illustration at the first-mode period of Building 6) and the intercept and slope coefficients for the *IM-EDP* transformations associated with each record. Both coefficients are negatively correlated with  $\varepsilon$ , having correlation coefficients ( $\rho$ ) ranging from -0.20 to -0.65 for the building models under consideration. This correlation is a direct consequence of the records with larger  $\varepsilon$  inducing smaller *EDPs*.

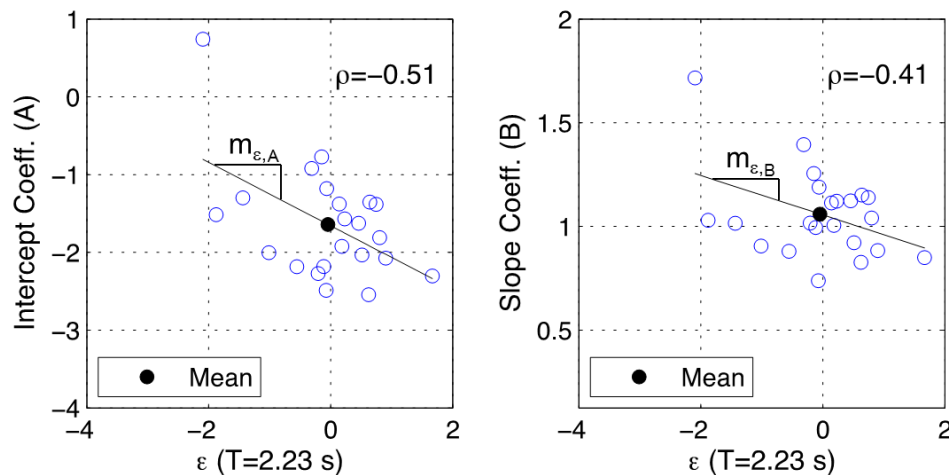


Figure 3.13. Scatterplots of slope and intercept coefficients (defining *IM-EDP* transformations) vs.  $\varepsilon$  for Building 6 with correlation coefficients and best-fit lines displayed on the plots. The slopes of the best-fit lines ( $m$ ) are discussed in a later section.

### 3.4.4.3 Method for Incorporating $\varepsilon$ in Computing Regional *IM-EDP* Transformations

It is clear from the previous discussion that deviations of the observed ground shaking from the expected ground shaking at a particular site, quantified by  $\varepsilon$ , affect the development of an appropriate *IM-EDP* transformation. However, to preserve the spatial correlation structure in the conversion from an *IM* map to an *EDP* map for a given building type, the same linear *IM-EDP* relationship must be used at all of the sites. In this study, we propose to resolve these somewhat competing objectives by developing an approach that uses the average  $\varepsilon$  of ground motions over the region to develop an *IM-EDP* transformation that is applicable for a particular building type at all sites in the region. The additional information obtained from the average regional  $\varepsilon$  is used to shift the mean and reduce the variance of the multivariate distribution defining the distribution of *IM-EDP* coefficients. In the regional loss assessment methodology, the  $\varepsilon$  values are already known, having been generated to make the intensity map in Step 3.

Before describing the details of this approach, it is necessary to characterize the parameter  $\varepsilon$  more fully. In particular,  $\varepsilon$  at any period can be decomposed into an inter-event term and an intra-event term (*e.g.* Campbell and Bozorgnia 2007), as shown here:

$$\ln(Sa) - E[\ln(Sa)] = \varepsilon * \sigma = \varepsilon_{inter} * \sigma_{inter} + \varepsilon_{intra} * \sigma_{intra} \quad 3.8$$

In Equation 3.8, intra-event terms ( $\varepsilon_{intra}$  and  $\sigma_{intra}$ ) quantify variability among different sites in a given event and the inter-event terms ( $\varepsilon_{inter}$  and  $\sigma_{inter}$ ) quantify variability between different events. In a given earthquake event, all sites have the same  $\varepsilon_{inter}$  (at a given period), but different  $\varepsilon_{intra}$ . Therefore, the average  $\varepsilon$  in an event ( $\varepsilon_{avg}$ ) is computed by Equation 3.9:

$$\varepsilon_{avg} \cong \frac{\varepsilon_{inter} * \sigma_{inter}}{\sigma} \quad 3.9$$

Equation 3.9 is exact if the GMPE used has constant  $\sigma$  and  $\sigma_{inter}$  at all sites for a given period (as in Boore and Atkinson 2008). It can also be shown that the distribution of  $\varepsilon$  values occurring across a region in a given scenario has smaller variance than the distribution of  $\varepsilon$  values occurring across multiple events (*e.g.* Campbell and Bozorgnia 2007).

The known value of  $\varepsilon_{avg}$  in the region for a given scenario and period of interest can be used to modify the multivariate distribution that defines the coefficients for the *IM-EDP* transformation. First, the mean coefficients ( $\mu_A$  and  $\mu_B$ ) of the *IM-EDP* relationship are adjusted for each building based on the difference between the average  $\varepsilon$  of the intensity map realization of a given scenario and period of interest ( $\varepsilon_{avg,map}$ ) and the average  $\varepsilon$  of the ground motion set used to develop the original distribution of coefficients through IDA, evaluated at the same period) ( $\varepsilon_{avg,IDA}$ ). This adjustment follows the best-fit regression line developed between  $\varepsilon$  and the intercept and slope coefficients,  $A$  and  $B$ :

$$\mu_{A,corrected} = \mu_{A,sampled} + (\varepsilon_{avg,map} - \varepsilon_{avg,IDA}) * m_{\varepsilon,A} \quad 3.10$$

In this equation,  $m_{\varepsilon,A}$  is the slope of the best-fit line between  $\varepsilon$  and the coefficient  $A$ , as shown in Figure 3.13. A similar equation can be developed for the slope coefficient,  $B$ .

$\varepsilon$  explains a significant portion of the variance in the coefficients defining the *IM-EDP* transformations, as indicated by the large correlation coefficients found in Figure 3.13. In order to sample coefficients for *IM-EDP* relationships for the case in which the average  $\varepsilon$  is known, only the portion of the variance that is not accounted for by  $\varepsilon$  is retained in the multivariate distribution. Since the slope and intercept coefficients are jointly distributed, the portion of their covariance that is not explained by  $\varepsilon$  can be represented by Equations 3.11 and 3.12 (Montgomery and Runger 2007). The diagonal terms of the covariance matrix can be written as:

$$COV(A, B)_{i,i_{remaining}} = COV(A, B)_{i,i} * (1 - \rho_i^2) \quad 3.11$$

Similarly, the off-diagonal terms can be taken as:

$$COV(A, B)_{i,j_{remaining}} = COV(A, B)_{i,j} * \sqrt{(1 - \rho_i^2) * (1 - \rho_j^2)} \quad 3.12$$

where  $\rho_i$  and  $\rho_j$  are the correlations of coefficient  $i$  and coefficient  $j$  with  $\varepsilon$ , respectively.

The modified multivariate distribution, described by corrected mean values of the coefficients,  $\mu_A$  and  $\mu_B$ , and reduced variance  $[COV(A, B)]_{remaining}$ , can be used to sample the coefficients  $A$  and  $B$  for defining *IM-EDP* relationships to account for the shared  $\varepsilon$  characteristics of a given scenario event. The obvious advantage of the proposed modification is that it accounts for the spectral shape of the records in the prediction of building responses. This modification is important, because  $\varepsilon$  influences the *IM-EDP* relationship, and its inclusion will reduce potential bias in the loss assessment procedure. Additionally, because the same *IM-EDP* transformation for a particular building is used at every site, correlations of *EDP* are still guaranteed to be identical to those of *IM*.

### 3.4.5 Adaptation of the Methodology to Include Collapsed Buildings, Multiple EDPs and Multiple Building Types

The methodology developed thus far can predict *EDP* maps through *IM-EDP* transformations for a given building type. For cases where the building does not collapse, losses can be predicted from the *EDP* maps utilizing *EDP*-based VFs. Losses for collapsed buildings are based on their estimated replacement costs. This study proposes to identify collapsed buildings if the  $Sa(T_1)$  at the site exceeds the collapse capacity, also quantified in terms of  $Sa(T_1)$ , and denoted  $Sa(T_1)_{Collapse}$ . Results for the six building models in this study revealed that  $Ln[Sa(T_1)_{Collapse}]$  is negatively correlated (on the order of -0.7 to -0.9) with the slope and

intercept coefficients of *IM-EDP* transformations, indicating that larger *A* and *B* coefficients are related to lower  $Sa(T_1)_{Collapse}$ , as expected. Furthermore, it is found that the all three variables, *A*, *B*, and  $Ln[Sa(T_1)_{Collapse}]$ , follow a multivariate normal distribution. Therefore,  $Sa(T_1)_{Collapse}$  should be sampled at the same time as the *IM-EDP* transformation from a common multivariate distribution

The methodology can also be easily extended to several *EDPs* and building types. The steps are the same, except that they are performed for multiple building types and *EDPs*. First, the analyst needs to perform IDA for models representing each building type that is contained within the portfolio. As described previously, IDA is carried out using a suite of ground motions. Ground motions should be carefully selected for use in determining a range of probable *IM-EDP* transformations by IDA analysis, in particular ensuring: (1) that the ground motion set contains a wide variety of spectral shapes, and (2) that the ground motions represent the tectonic environment of the region of interest. Linear *IM-EDP* transformations for each building type and *EDP* of interest, as well as  $Sa(T_1)_{Collapse}$ , are fitted to the IDA results for each ground motion record and building type. The parameters of a multivariate normal distribution are then computed from the coefficients defining the *IM-EDP* transformations and the  $Ln[Sa(T_1)_{Collapse}]$  values. It is important to develop a joint distribution representing the coefficients associated with all of the buildings and *EDPs*, because cross-correlations are not preserved if their distributions are assumed to be independent.

For the purposes of illustration, imagine a building portfolio wherein each building is represented by one of the six building types in this study. Imagine also that losses in each building are predicted from two structural response parameters: *IDR* and *PFA*. In this case, one would perform IDA for all six model buildings. *IM-EDP* transformations for each IDA curve and

each building are obtained by fitting linear regressions between  $\text{Ln}[IDR]$  and  $\text{Ln}[Sa(T_1)]$ , and  $\text{Ln}[PFA]$  and  $\text{Ln}[Sa(T_1)]$ , results. Based on the suite of *IM-EDP* relationships and  $\text{Ln}[Sa(T_1)_{Collapse}]$  values obtained from the IDA results, a joint distribution of intercept and slope coefficients and collapse capacities is constructed. For this example, the joint distribution defines five random variables (*i.e.* two linear regression coefficients per *EDP* x two *EDPs* +  $\text{Ln}[Sa(T_1)_{Collapse}]$ ) for each of the six building types, resulting in 30 random variables. Slope and intercept coefficients of *IM-EDP* relationships and  $\text{Ln}[Sa(T_1)_{Collapse}]$  for all of the building types are sampled from the 30 variable multivariate distribution. A new set of relationships would be sampled from the same multivariate distribution before creating each new *EDP* map.

One remaining complication related to the prediction of *EDPs* in the proposed regional loss assessment method is the representation of a class of buildings by a single model. This representation of a class of buildings with a single model or capacity curve is a limitation to virtually all regional loss assessment methods, due to the infeasibility of individually characterizing each building in a region. The variability in structural characteristics and response among archetype buildings of the same type could be estimated and incorporated in the methodology, but it is not the focus of this article. It is expected that including this source of variability in the loss estimation method would result in a small and likely realistic reduction of the correlation, because it introduces more randomness into the loss assessment.

### **3.4.6 Relation to Steps in Regional Loss Assessment Method**

The proposed methodology prescribes a set of steps for simulating *EDPs* (*i.e.*  $\widehat{EDPs}$ ) for spatially-distributed building stocks, based on spatial distributions of  $Sa(T_1)$  (intensity maps). Previous studies have recommended simulating  $n$  combinations of earthquake magnitudes and locations on each known fault in a region and generating at least  $p = 50$  intensity maps per

earthquake simulation to develop probabilistic predictions of losses (Jayaram and Baker 2010). In addition,  $q$  realizations of spatially-distributed  $\widehat{EDP}$ s (*EDP* maps) are required for each intensity map, for a total of  $n$  scenarios  $\times$   $p$  intensity maps/scenario  $\times$   $q$  *EDP* maps/intensity map. Further studies are needed to recommend an appropriate value of  $q$ . For each realization, the expected loss of individual buildings is computed from *EDP*-based VFs and the regional loss is obtained by summing the individual losses. Importance sampling techniques (*e.g.* Jayaram and Baker 2010) are likely critical to make this procedure more computationally tractable.

### 3.5 Conclusions

Considering spatial correlations in ground motion intensity improves regional seismic loss assessments, particularly for rare, high consequence events. This study examines spatial correlations between building response parameters. Results show that correlations in building response are more significant for more similar buildings and closely spaced sites. A critical observation is that spatial correlation patterns between engineering demand parameters (*i.e.* *EDPs*, particularly interstory drift) and spectral accelerations at a building's first-mode period ( $Sa(T_1)$ ) are similar, when evaluated in natural log space.

Building on these observed patterns of spatial correlations, the authors propose a method for incorporating correlations in building response in regional seismic loss assessment procedures. In the proposed approach, maps of correlated ground motion intensities are generated with existing models. These “intensity maps” are used to predict spatial distributions of *EDPs* through linear *IM-EDP* transformations. The transformations produce building responses that capture the expected spatial correlation structure of *EDPs*. The distribution of coefficients for defining such transformations is obtained by performing incremental dynamic analysis (IDA) on nonlinear models representing each building type of interest. The distribution

of probable *IM-EDP* relationships that is obtained from IDA is modified to estimate the distribution of probable *IM-EDP* transformations for a region based on regional seismicity. This addition to regional loss assessment methods represents the first time correlations in building responses, in addition to ground motion intensities, are explicitly considered.

Since *EDPs* are better predictors of damage and loss than  $Sa(T_1)$ , such a process is expected to improve methods for estimating losses for a region. Future studies will evaluate the proposed regional loss assessment method to investigate the significance of including building response correlations in the regional loss assessment, providing the basis for development of simplified methods to account for these correlations.

### 3.6 Data and Resources

Ground motion time histories for the Northridge, Chi Chi, and Loma Prieta earthquakes came from the PEER ground motions database, available at [http://peer.berkeley.edu/peer\\_ground\\_motion\\_database](http://peer.berkeley.edu/peer_ground_motion_database) (last accessed February 2012). Ground motion time histories for the simulated earthquakes, ShakeOut and Puente Hills, were provided by Robert Graves.

Building models are analyzed with *OpenSees* (Open System for Earthquake Eng. Simulation), available at [OpenSees.berkeley.edu](http://OpenSees.berkeley.edu) (last accessed January 2011).

### 3.7 Acknowledgments

This research was supported by the Southern California Earthquake Center (SCEC). SCEC is funded by NSF Cooperative Agreement EAR-0529922 and USGS Cooperative Agreement 07HQAG0008. The SCEC contribution number for this paper is 1743. The authors would like to acknowledge Curt Haselton for providing the modern building models, Kristen Rowe for conducting some of the nonlinear dynamic time-history analyses and Jack Baker, Holly

Bonstrom, Ross Corotis, and Keith Porter for their discussions of the study. We are also grateful for the thoughtful comments of two anonymous reviewers.

## 4 A COMPARATIVE EVALUATION OF PROBABILISTIC REGIONAL SEISMIC LOSS ASSESSMENT METHODS, USING SCENARIO CASE STUDIES

**ABSTRACT:** This study compares current and developing probabilistic regional (portfolio) loss assessment methods. These comparisons are carried out for two scenario earthquake events. Of particular interest are: the impact of directly considering building responses versus basing losses on ground motion intensity; identifying best practices for predicting collapsed buildings; and examining the sensitivity of loss assessments to other methodological decisions related to building stock classification and exposure and key sources of uncertainty. On the basis of the identified strengths and weaknesses of the different regional loss assessment techniques, high-end and simplified methods are recommended for computing probabilistic regional seismic losses.

### 4.1 Reference Article

DeBock, D.J. and A.B. Liel (2014b), “A comparative evaluation of probabilistic seismic loss assessment methods, using scenario case studies.” *Journal of Earthquake Engineering*. Under Review.

### 4.2 Introduction

Performance-based earthquake engineering (PBEE) is intended to enable risk-informed decision-making. To date, much of the research related to PBEE has focused on quantifying the possible risks to individual buildings. However, parties interested in a group of geographically-distributed buildings, such as policy makers, insurers, and real-estate developers, need to make risk-informed decisions on a regional or portfolio, rather than an individual building, basis (Liel

and Deierlein 2012). For this reason, over the past decade, researchers have developed methods to extend PBEE to assess the risk of earthquake-induced losses for groups of buildings (hereafter referred to as “regional losses”). These methods predict the expected loss, as well as the variation therein, recognizing that risk-informed decision-making depends upon quantifying the likelihood of experiencing rare, but catastrophic levels of loss (Haimes 1998).

There are many sources of uncertainty affecting the prediction of earthquake-induced regional losses, including those associated with the characteristics of future earthquakes, the properties of ground shaking at different sites, building response and capacity, the fragility of building components, and the costs of repairing damage, to name a few. Due to these uncertainties and the lack of closed-form solutions available to propagate these uncertainties through the loss assessment, state-of-the-art methods for probabilistic regional seismic loss assessment (Bazzurro and Luco 2005, Crowley and Bommer 2006, Lee and Kiremidjian 2007, Park *et al.* 2007, Goda and Hong 2008a, Jayaram and Baker 2010, Vaziri *et al.* 2012, DeBock *et al.* 2013) rely heavily on Monte Carlo-based simulation methods (Fishman 2006). This amounts to repeating the loss assessment for different sets of probabilistically characterized input random variables to develop a suite of “regional loss realizations” from which statistics for the mean and variance in regional loss can be obtained. Figure 4.1 describes the major steps comprising these Monte Carlo-based regional loss assessment methods.

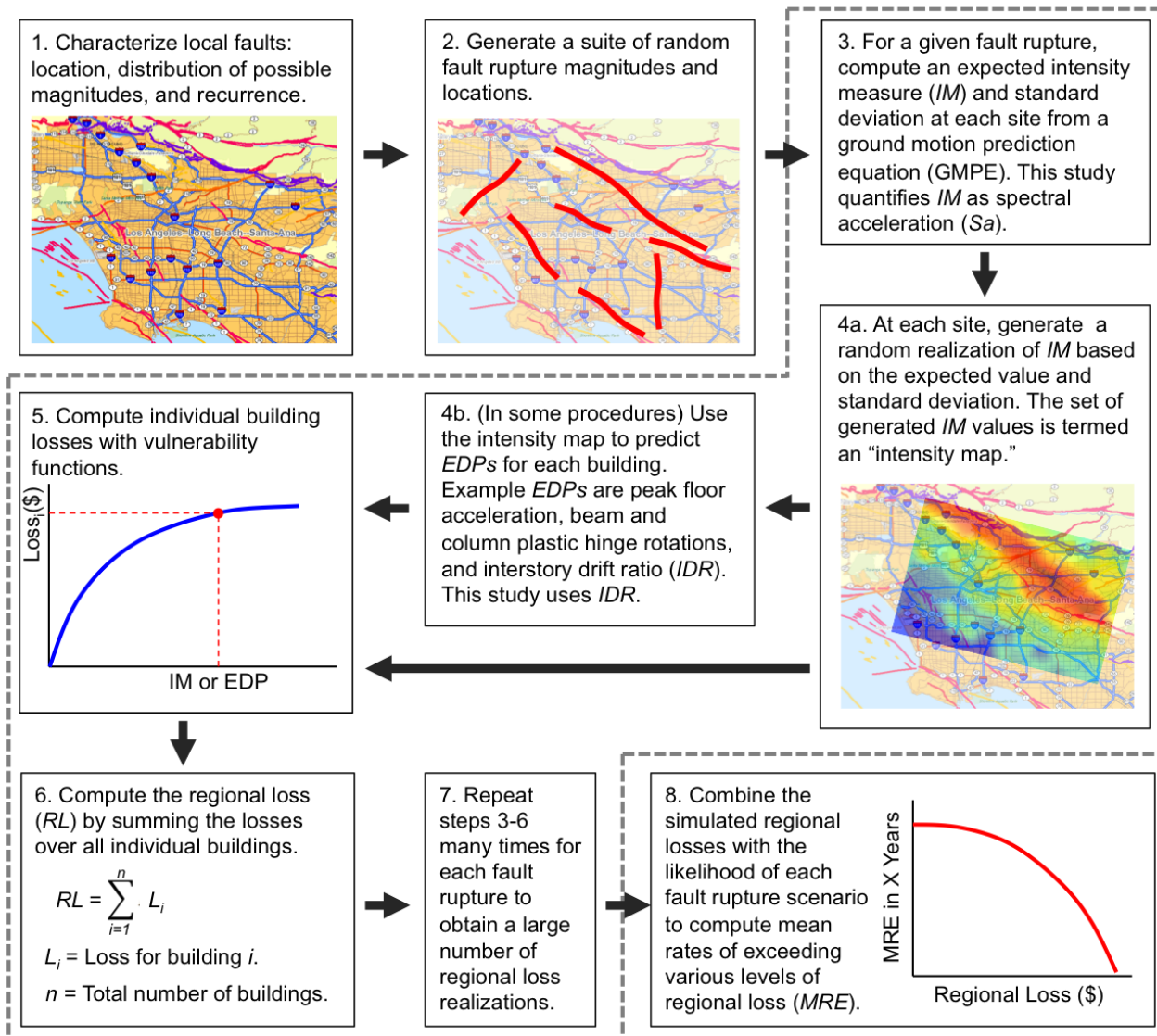


**Figure 4.1. Illustration of probabilistic methods for regional loss assessment. Aspects examined in this study are outlined by the gray dashed box.**

This article investigates alternative regional seismic loss assessment methods. The evaluation is conducted by assessing regional losses by different methods for multiple building stocks for two earthquake scenarios (corresponding to the Steps 3-7 in Figure 4.1, outlined in gray). The predictions for the median and distribution of the regional loss obtained from the different methods are compared with the aim of satisfying four primary objectives. The first objective is to evaluate the effectiveness of  $IM$ -based loss assessment methods (Step 4a) as compared to  $EDP$ -

based loss assessment methods (Step 4b) for non-collapsed buildings. In this study,  $IM$  is the spectral acceleration at a building's first-mode period ( $Sa(T_1)$  or  $Sa$ ) and the  $EDP$  considered is interstory drift ratio ( $IDR$ ), so  $IM$ -based and  $EDP$ -based methods are hereafter referred to as  $Sa$ -based and  $IDR$ -based for clarity. The second objective is to explore alternative methods for dealing with collapsed buildings in the loss assessment. The third objective is to identify those sources of variability and uncertainty in Steps 3-7 of the loss assessment that have the largest influence on the regional loss results.<sup>6</sup> These findings are then used to propose methods for completing Steps 3-7 of the loss assessment procedure that are simple, yet provide robust predictions of the median and distribution of possible earthquake-induced losses in a region.

### 4.3 Overview of Regional Seismic Loss Assessments

#### 4.3.1 Earthquake Scenarios

Regional losses are quantified for two earthquake scenarios, representing two realizations of Steps 1 & 2 in Figure 4.1. The first scenario considered is the “ShakeOut”  $M_w$  7.8 south-to-north rupture on the southern San Andreas fault. The ShakeOut is a hypothetical earthquake, for which Graves *et al.* (2008) modeled ground motion time histories throughout the southern California region with physics-based simulations of the fault rupture and seismic wave propagation. The ground motions and data quantifying site conditions are available for a large number of uniformly spaced sites (at 1.2 mile intervals) over the southern California region. The ShakeOut scenario is analyzed here because of the high spatial resolution of the time-history data available.

---

<sup>6</sup> Due to our focus on Steps 3 -7, a significant source of uncertainty that is excluded from discussion in this article is variability in fault seismicity properties (*e.g.* magnitude, locations of fault ruptures, and seismic rates). Aslani *et al.* (2012) develops a method for incorporating uncertainty in seismic rates into regional seismic loss assessments, showing they may have a significant influence on the variability of the losses.

The second scenario is the historical 1999  $M_w$  7.6 Chi Chi, Taiwan earthquake. Chi Chi ground motion recordings for more than 400 sites, together with site soil properties, are available from the PEER NGA strong motion database (Chiou *et al.* 2008). The high density of sites with recordings along the west coast provides good spatial resolution of ground motion characteristics in that region. Since the time histories from Chi Chi are recorded from a historical event, it provides a check against the simulated ShakeOut results.

### **4.3.2 Building Stocks and Test Regions**

#### *4.3.2.1 Downtown Los Angeles RC Moment Frame Building Stock*

The building stocks constituting the regional exposure to seismic losses in this study are based on the reinforced concrete (RC) building stock in and around southern downtown Los Angeles. The study focuses on RC moment frames, because these buildings are expected to represent a significant part of the regional loss exposure in Los Angeles (Lynch *et al.* 2010, Comerio and Anagnos 2012), and because we have access to robust nonlinear simulation models for nonductile and ductile RC frame buildings. The Los Angeles RC moment frame building stock is inventoried for an area encompassing five downtown zip codes (90071, 90013, 90014, 90015, and 90021), which is labeled in Figure 4.2 as “small region”. The gross building square footage and year of construction is estimated from HAZUS (FEMA 2003) and height distribution is estimated by visual review of the inventory with Google (2013) Streetview. On the basis of these observations, the area is estimated to have about 175 RC moment frame buildings, totaling approximately 7 million gross square feet. These buildings are further categorized by occupancy, height, and year of construction. Three different types of occupancies are considered: (1) residential (apartments/condos), (2) commercial (office/retail), and (3) hospitality (hotels). Buildings heights are classified as: (1) low-rise (1-2 stories), (2) mid-rise (3-6 stories), and (3)

high-rise (>6 stories). In addition, buildings are divided by year of construction to distinguish between nonductile (pre-1980) and ductile (post-1980) structures. The distribution of buildings by gross square-footage, height and occupancy are summarized in Figure 4.3. The building stock is intended to be realistic, but a precise representation of Los Angeles's building inventory is not possible and the exact location of each building is unknown. Accordingly, buildings are randomly assigned locations within their respective zip codes, the outcome of which is shown in Figure 4.4. For the purpose of the loss assessment, each building is mapped to the closest point on a grid with 0.3 mile spacing. The estimated building stock shows good agreement with findings of Comerio and Anagnos (2012) in terms of height and occupancy distribution of the older concrete buildings.

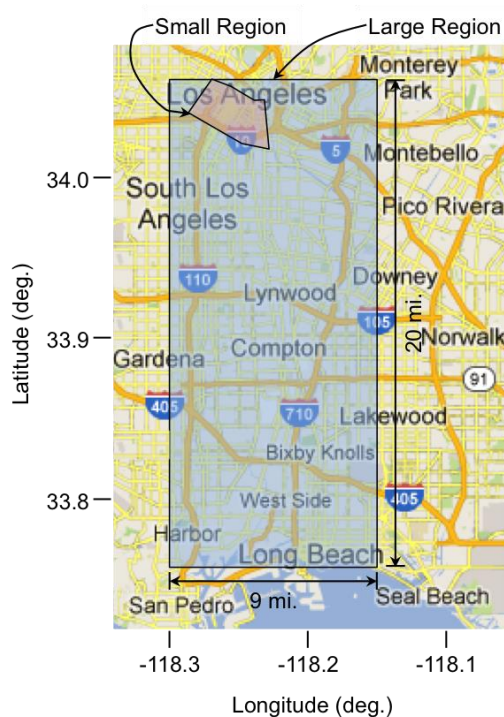


**Figure 4.2. Small and large regions considered in and around Los Angeles. (Background map from [www.findlatitudeandlongitude.com](http://www.findlatitudeandlongitude.com)).**

#### 4.3.2.2 Additional Building Stocks

Additional hypothetical building stocks occupying different regions and/or having different building densities are considered. A “large” region in the Los Angeles metro area is shown in Figure 4.2, encompassing roughly thirty times the area of the small region. For each region, two versions of the building stock are considered: (1) a “dense” building stock that has the same number of RC frame buildings per square mile as estimated based on the downtown Los Angeles RC building stock, and (2) a “sparse” building stock that has one-tenth the building density. Only the small region with dense building stock is a realistic representation of Los Angeles RC frame buildings; the others are considered to examine how region size and building stock variability affect regional loss assessments. The Los Angeles regions are analyzed for the ShakeOut earthquake scenario.

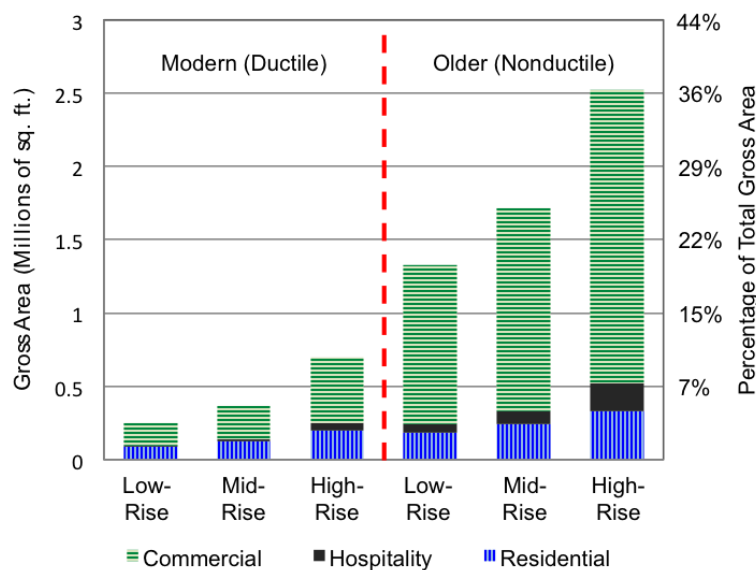


**Figure 4.3. Distribution of RC frame building stock for downtown Los Angeles (small region) by height, occupancy and year of construction.**

Two large regions are also analyzed for the Chi Chi, Taiwan earthquake scenario, as shown in Figure 4.5. No attempt is made to inventory the actual Taiwanese building stock and

the dense and sparse Los Angeles building stocks are artificially transported to Taiwan for comparison purposes and assigned random locations within the regions. A sensitivity study presented later in the article also concentrates buildings into different sub regions (shown in Figure 4.5) within one of the large regions.

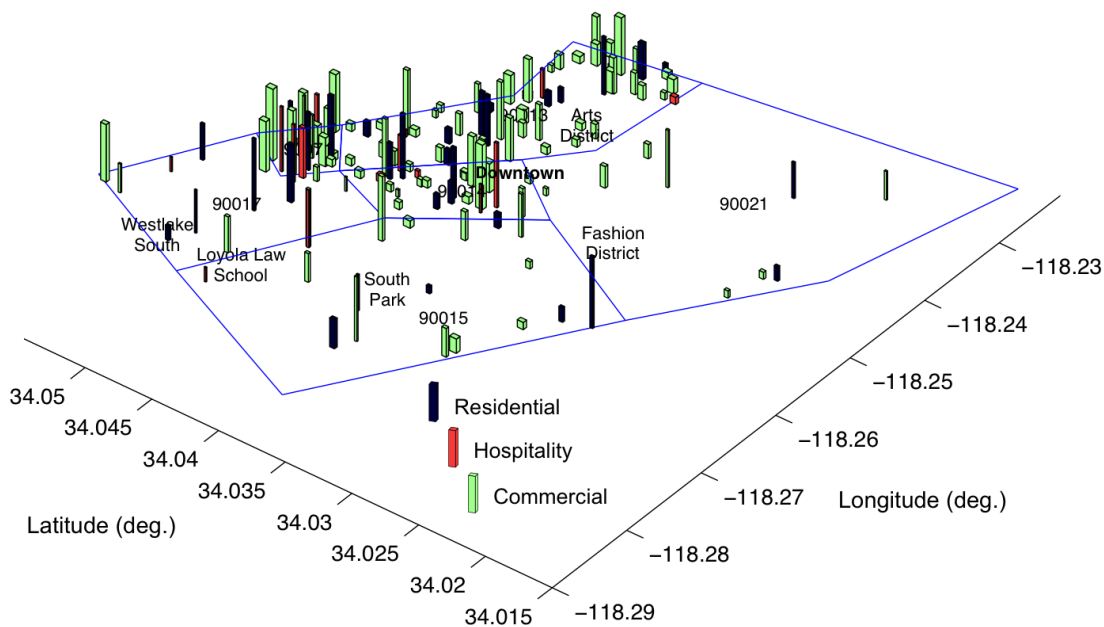


**Figure 4.4.** Map of building locations generated for the downtown Los Angeles building stock (small region). Building sizes are shown for illustration, but exaggerated.

### 4.3.3 Building Representations, Structural Analyses and Loss Assessments

#### 4.3.3.1 Classification of Building Inventory through Model Buildings

For the purpose of regional loss assessment, it is computationally prohibitive to individually model and assess the losses for each building. Instead, each RC frame building in the building stock is represented by one of a group of six robust multiple-degree-of-freedom nonlinear simulation models that is most similar to the structure of interest on the basis of height and year

built. The model buildings are ductile and nonductile moment resisting frames, and range in height from two to eight stories. Each model building is simulated in 2D (Haselton *et al.* 2011a, Liel *et al.* 2011) with *OpenSees* (PEER 2013). Material nonlinearities are represented by lumped plasticity beam and column elements and inelastic joint shear springs. Geometric ( $P-\Delta$ ) effects are also considered. Table 4.3 summarizes the model buildings' characteristics.

Losses for non-collapsed buildings are predicted with vulnerability functions. The vulnerability functions are either  $Sa$ -based, taking  $Sa$  as input, or  $IDR$ -based, taking  $IDR$  as an input, and output the predicted building loss (in dollars). Vulnerability functions are developed by fitting regression models to suites of loss data that are obtained for each combination of model building and occupancy category. The loss data are obtained with the Performance Assessment Calculation Tool, PACT (FEMA 2012).

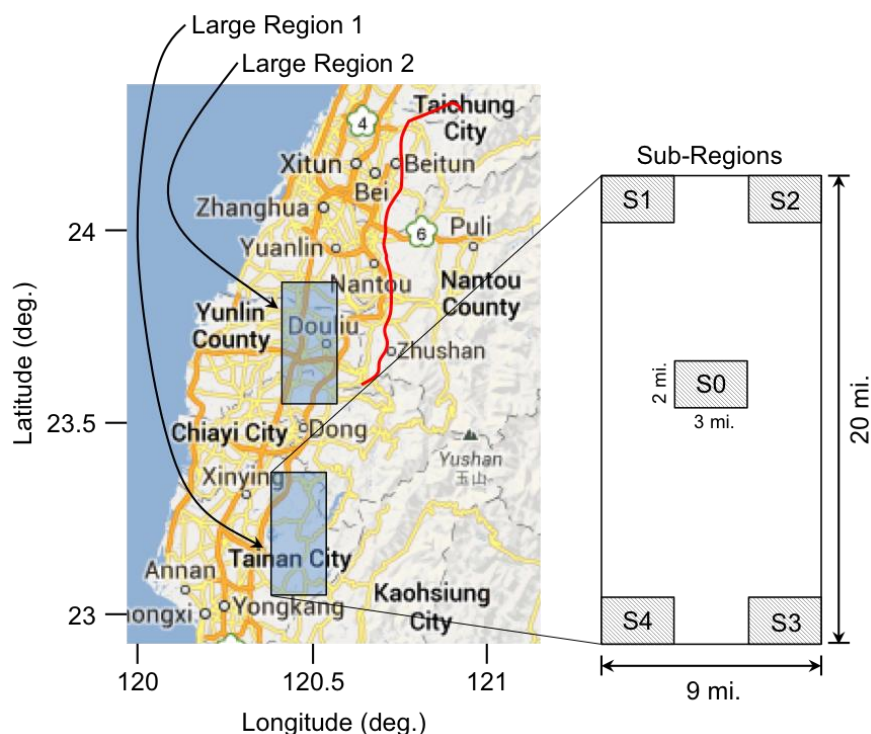


**Figure 4.5. Regions considered in Taiwan, together with the approximate fault rupture location (red line) for the Chi Chi earthquake in Taiwan from (Rubin *et al.* 2001). (Background map from [www.findlatitudeandlongitude.com](http://www.findlatitudeandlongitude.com)).**

**Table 4.3. Model buildings representing the class of RC moment frames.**

Model Bldg. No.	Model Bldg. Description	No. of Stories	First-Mode Period (T1) (s)*	Ductility Capacity†
1	Low-rise, new (Ductile)	2	0.60	15.0
2	Mid-rise, new (Ductile)	4	0.91	10.7
3	High-rise, new (Ductile)	8	1.81	6.0
4	Low-rise, old (Nonductile)	2	1.03	3.3
5	Mid-rise, old (Nonductile)	4	1.92	2.3
6	High-rise, old (Nonductile)	8	2.23	2.3

\* Determined from eigenvalue analysis assuming cracked concrete sections of about 35% of the gross properties, depending on axial load. As a result, these periods are longer than those that have been measured in moderate shaking events (Goel and Chopra 1997).

† Determined by nonlinear static pushover analysis as described in FEMA (2009). There are many methods for computing ductility, so these values are provided for the purpose of comparing deformation capacity of the model buildings.

To predict building losses in PACT, the user inputs structural analysis data quantifying *EDPs*. For the purpose of this study, the model buildings are subjected to the ground motions of the FEMA (2009) far-field set and scaled to several different intensity levels through incremental dynamic analysis (IDA), as illustrated in Figure 4.6. The predicted nonlinear dynamic response serves as the *EDP* input to PACT. The far-field set<sup>7</sup> contains ground motions with a broad range of spectral content, recorded at moderate distances for shallow crustal events of the type that may occur in Southern California. For each intensity level of interest, PACT then generates random realizations of building response based on the inputted structural response data. For each realization, the predicted damage and loss for each component in the building (*e.g.* partitions, plumbing, etc.) is generated with a fragility function which takes an *EDP* at the location of the component as its input, and returns a random realization of component damage and losses, *i.e.* repair or replacement cost. The damage states in different components are assumed to be

---

<sup>7</sup> This set consists of 22 ground motion pairs. For each pair, the ground motion intensity is taken as the geometric mean of *S<sub>a</sub>* of the two horizontal components. *IDR* is the maximum *IDR* occurring from separate application of the two components, in order to quantify the maximum response of a 3-D building.

uncorrelated. The inventory of components in a building depends on the size and occupancy type of the building and assumed architectural and content characteristics associated with that occupancy. PACT provides estimates of the quantities of different components typically found in buildings of different types. The total building loss is the sum of the losses for all of a building's components. PACT is able to account for those components that past research (*e.g.* Beck *et al.* 2002) has shown to be responsible for the majority of earthquake losses, such as dry-wall partitions and columns. For a given intensity input, PACT is used to generate multiple realizations of building loss, considering uncertainties in structural response, component fragilities, and quantities of building components.

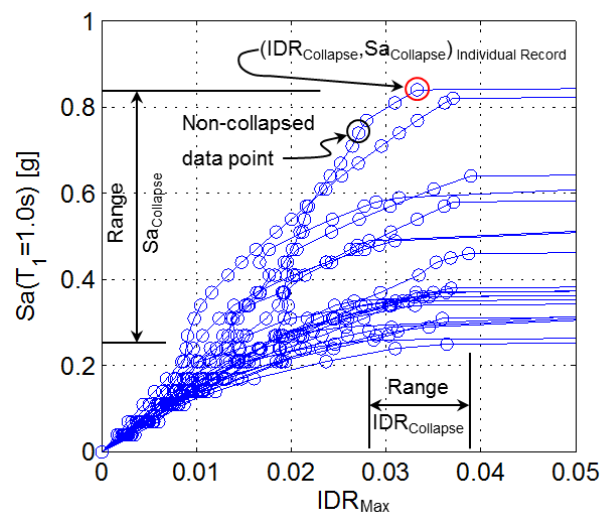


**Figure 4.6. IDA for model building no. 4 computed with the FEMA (2009) far-field ground motions, showing non-collapse structural analysis results, which are inputted into PACT, and the collapse capacity distribution.**

Vulnerability functions are created here using PACT to generate a suite of 4000 realizations of losses for each model building and occupancy category (18 total combinations). The losses cover the range of ground shaking intensity considered in the structural analysis. Vulnerability functions are fitted to the building loss data through local polynomial regression analysis (Fan

and Gijbels 1996). Local polynomials are a moving weighted regression in which the regression at each point weights the remaining data points according to their relative distance to the point of reference. The use of local polynomials is appealing because it captures the expected value and variance in the data, even for data sets that do not satisfy homoscedasticity. The vulnerability functions can be fitted with respect to  $Sa$  or  $IDR$ , as illustrated in Figure 4.7(a)-(b).<sup>8</sup> Although other approaches for developing vulnerability functions exist (e.g. Porter et al. 2001, FEMA 2003, Mitrani-Reiser 2007, Ramirez and Miranda 2009), we develop ours “in house” to ensure that the different versions of the vulnerability functions (e.g.  $Sa$ -based vs.  $IDR$ -based) are computed consistently from the same data and by the same methods.

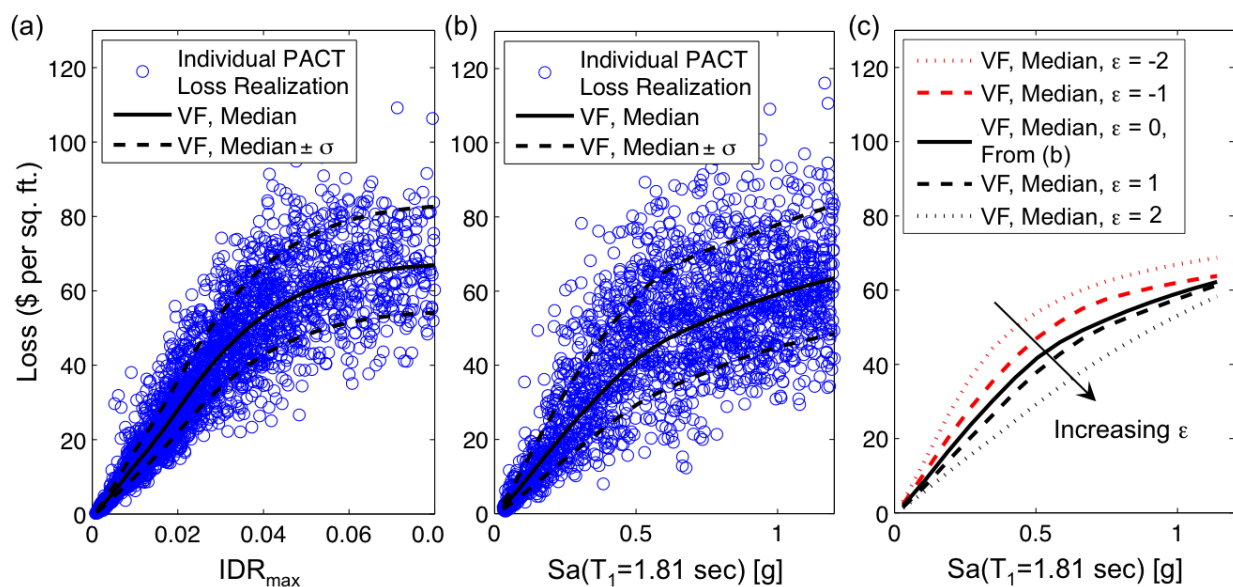


**Figure 4.7. Vulnerability functions (VF) for non-collapsed buildings, for structures represented by model building no. 3, with commercial occupancy showing: (a)  $IDR$ -based vulnerability function; (b)  $Sa$ -based vulnerability function; and (c)  $Sa$ - $\epsilon$ -based vulnerability function. For reference, the median replacement cost of this building is estimated at \$162/ft<sup>2</sup>.**

<sup>8</sup> We also developed a second set of  $EDP$ -based vulnerability functions, which take a vector of  $IDR$  and  $PFA$  as input, but these proved to be no better, in terms of their predictive ability, than those based simply on  $IDR$ .

Losses to collapsed buildings are based on the building replacement cost. Expected replacement costs are estimated from RSMMeans (2009) and range from \$160 to \$200 per gross square foot in 2009 dollars, depending on building height and occupancy type. Replacement cost is assumed to be lognormally distributed with a logarithmic standard deviation of 0.3. This value is based on construction cost data analyzed by Ramirez and Miranda (2009), assuming a low level of correlation in subcontractor costs.

The principal challenge associated with predicting losses in the collapsed buildings is determining whether or not a building collapsed. The collapse capacity of each model building can be determined from IDA, as illustrated in Figure 4.6. The collapse capacity may be quantified in terms of  $S_a$  or  $IDR$  and is the intensity (*i.e.*  $S_a$ ) or response (*i.e.*  $IDR$ ) after which the building becomes unstable. Following Vamvatsikos and Cornell (2002), collapse is approximated as the point at which the slope of curve relating  $S_a$  to maximum  $IDR$  reduces to less than 20% of its initial slope, indicating a small increase in  $S_a$  produces a large increase in response. For each model building, distributions of  $S_{a,collapse}$  and  $IDR_{collapse}$  are computed from IDA using the FEMA (2009) ground motions, and summarized in Table 4.4.

**Table 4.4. Collapse capacities of model buildings.**

Model Bldg. No.	$S_{a,collapse}$		$IDR_{collapse}$	
	Median	$\beta^*$	Median	$\beta^*$
1	2.42	0.50	0.068	0.20
2	1.52	0.43	0.071	0.17
3	0.57	0.41	0.050	0.20
4	0.37	0.35	0.033	0.11
5	0.25	0.32	0.059	0.26
6	0.22	0.42	0.042	0.23

In addition to the  $S_a$ -based and  $IDR$ -based vulnerability functions and collapse capacities, vulnerability functions and collapse capacities that consider  $S_a$  and an additional ground motion

parameter, epsilon ( $\varepsilon$ ), are developed for so-called  $Sa$ - $\varepsilon$ -based assessments.  $\varepsilon$  is a property of the ground motion that is computed as the difference between the ground motion intensity observed at a site and the expected intensity from a ground motion prediction equation, quantified by the number of standard deviations the observation lies away from the expected intensity.  $\varepsilon$  is a proxy for spectral shape and is a significant predictor of building  $EDP$  responses, given  $Sa$  (Baker and Cornell 2005). The  $Sa$ - $\varepsilon$ -based vulnerability functions are computed from the same data and by the same approach as the other vulnerability functions. However, the local polynomial regression is carried out with respect to both the  $Sa$  and the  $\varepsilon$  of the ground shaking causing each PACT loss realization, such that a vulnerability function surface taking  $Sa$  and  $\varepsilon$  as input is produced. Collapse capacity distributions that are a function of  $\varepsilon$  are computed by regressing the natural logarithm of  $Sa_{collapse}$  for each record with  $\varepsilon$ . Figure 4.7(c) illustrates the effect of  $\varepsilon$  on the vulnerability function for one of the model buildings. Vulnerability functions conditioned on higher  $\varepsilon$  tend to have lower losses because of the peaked, less damaging spectral shape that is associated with high  $\varepsilon$  ground motions. The collapse capacity distribution also is increased for higher  $\varepsilon$  ground motions (Haselton *et al.* 2011b).

#### 4.4 Candidate Regional Loss Assessment Methods

This section describes the different methods by which the various steps in the loss assessment are performed. These methods are summarized in Table 4.5.

##### 4.4.1 Developing Regional Ground Motion Intensity Maps

We first consider alternative methods for producing intensity maps for the scenario of interest, completing Steps 3 & 4a (Figure 4.1) in the loss assessment. Most of these methods employ a GMPE. GMPEs predict the median ground motion intensity at site  $i$  for intensity map

realization  $j$ ,  $\widehat{Sa}_{ij}$ , and quantify the uncertainty in that prediction. The spectral acceleration is then represented by Equation 4.1,

$$\text{Ln}(Sa_{ij}) = \text{Ln}(\widehat{Sa}_{ij}) + \sigma_{ij}\epsilon_{ij} + \tau_j\eta_j = \text{Ln}(\widehat{Sa}_{ij}) + \sqrt{\sigma_{ij}^2 + \tau_j^2} * \epsilon_{ij} \quad 4.1$$

where  $\sigma_{ij}$  and  $\tau_j$  are standard deviations representing intra-event and inter-event variability, and  $\epsilon_{ij}$  and  $\eta_j$  are the intra-event and inter-event residuals of  $Sa_{ij}$ .  $\epsilon_{ij}$  is  $\epsilon$  for site  $i$  and intensity map realization  $j$  and represents the total (intra plus inter-event)  $Sa$  residual. All of the parameters in Equation 4.1 are defined at the period of interest, which is first-mode period of the model building  $h$  located at that site ( $T_{1,h}$ ). The intra-event  $Sa$  residual varies between sites, representing uncertainties in site response and source-to-site path affects. The inter-event  $Sa$  residual is constant at all sites for a given intensity map and period, representing uncertainty due to fault rupture characteristics and regional effects. Both residual terms ( $\epsilon_{ij}, \eta_j$ ) are normally distributed with mean of 0 and standard deviation of 1. In the methods that follow, it is sometimes convenient to refer also to the total  $Sa$  residual for an earthquake, averaged over all sites,  $\epsilon_{avg,j}$ .

Since the  $\epsilon_{ij}$  residual has a mean of zero for intensity map  $j$ ,  $\epsilon_{avg,j}$  is given by Equation 4.2:

$$\epsilon_{avg,j} \approx \frac{\tau_j\eta_j}{\sqrt{\sigma_{ij}^2 + \tau_j^2}} \quad 4.2$$

Equation 4.2 is exact if the GMPE used has constant  $\tau_j$  and  $\sigma_{ij}$  at all sites for a given period, as in Boore and Atkinson (2008).

Two sources of correlation affect the spatial distribution of  $Sa_{ij}$ . First, intra-event  $Sa$  residuals at nearby sites  $i$  and  $k$  (*i.e.*,  $\epsilon_{ij}$  and  $\epsilon_{kj}$ ) are known to be correlated, due to their geographic proximity, such that  $Sa_{ij}$  and  $Sa_{kj}$  will tend both to be either higher or lower than the average GMPE prediction. The degree of correlation in intra-event  $Sa$  residuals depends strongly

on site separation distance, but also on period and soil conditions (Wesson and Perkins 2001, Wang and Takada 2005, Goda and Hong 2008b, Goda and Atkinson 2009, Jayaram and Baker 2009, Sokolov *et al.* 2010, Esposito and Iervolino 2011, Loth and Baker 2013, Du and Wang 2013). Second, inter-event  $Sa$  residuals for two periods  $T_1$  and  $T_2$  (*i.e.*,  $\eta_j(T_1)$  and  $\eta_j(T_2)$ ) will be correlated. In this case, the degree of correlation depends on the relative values of  $T_1$  and  $T_2$ , since if ground motion intensity is higher than average at  $T_1$ , it is also likely to be higher than average at other periods close to  $T_1$  (Baker and Cornell 2006).

In this study, an intensity map  $j$ , which represents  $Sa_{ij}$  for all sites in the earthquake of interest  $j$ , is computed by several different approaches, which are summarized in Table 4.5(a). All approaches use the Boore and Atkinson (2008) GMPE to compute  $\widehat{S}a_{ij}$ ,  $\sigma_{ij}$  and  $\tau_j$ . Methods G1-G3 compute  $\widehat{S}a_{ij}$  from the GMPE and obtain  $Sa_{ij}$  through Equation 4.1. However, the method of randomly generating the  $Sa$  residuals differs between the methods. G1 assumes both  $Sa$  residuals are zero at each site, taking  $Sa_{ij} = \widehat{S}a_{ij}$ . G2 generates random realizations of inter-event and intra-event  $Sa$  residuals, considering period-to-period correlations of inter-event  $Sa$  residuals using the model proposed Baker and Cornell (2006), but not site-to-site (spatial) correlations of intra event  $Sa$  residuals. G3 generates random realizations of the  $Sa$  residuals, using models that consider both period-to-period correlations and spatial correlations. Spatially correlated intra-event  $Sa$  residuals are generated with the Loth and Baker (2013) model.

The final method, G4, computes  $Sa_{ij}$  from the simulated or recorded ground motion time histories at each site for the earthquake scenario of interest. For buildings located at a site where ground motion time-history data are not available,  $Sa_{ij}$  is linearly interpolated (in natural log space) based on proximity to neighboring sites.

**Table 4.5. Summary of methods compared for different steps in the loss assessment.**

<b>(a) Methods for developing intensity maps (Steps 3 &amp; 4a in Figure 1)</b>	
<b>ID</b>	<b>Description</b>
G1	$Sa_{ij} = \bar{S}a_{ij}$ . $Sa_{ij}$ taken as the median predicted value from the GMPE.
G2	$Ln(Sa_{ij}) = Ln(\bar{S}a_{ij}) + \sigma_{ij}\epsilon_{ij} + \tau_j\eta_j$ . $Sa_{ij}$ is computed from the GMPE and randomly generated $Sa$ residual values. Considers period-to-period correlation among $\eta_j$ , but not spatial correlation among $\epsilon_{ij}$ .
G3	$Ln(Sa_{ij}) = Ln(\bar{S}a_{ij}) + \sigma_{ij}\epsilon_{ij} + \tau_j\eta_j$ . $Sa_{ij}$ is computed from a GMPE and randomly generated $Sa$ residual values. Considers period-to-period correlation among $\eta_j$ , and spatial correlations among $\epsilon_{ij}$ .
G4	$Sa_{ij}$ is computed from ground motion time histories produced by the scenario earthquake.
<b>(b) Methods for predicting building response (Step 4b in Figure 1)</b>	
<b>ID</b>	<b>Description</b>
E0	$Sa$ -based methods. These methods do not explicitly consider $IDR$ in the regional loss assessment.
E1	$Ln[IDR_h] = A_h + B_h * Ln[Sa_h]$ . Coefficients ( $A_h$ and $B_h$ ) defining $Sa$ - $IDR$ transformations for each building $h$ are randomly generated from a multivariate normal distribution that relates $A_h$ , $B_h$ , and $Sa_{h,collapse}$ . The parameters defining the multivariate distribution are obtained from nonlinear analysis of simulation models for model buildings.
E2	$Ln[IDR_h] = A_h + B_h * Ln[Sa_h]$ . Coefficients ( $A_h$ and $B_h$ ) defining $Sa$ - $IDR$ transformations for each building $h$ are back-calculated from the ground motion time histories and nonlinear response history results for the scenario of interest.
E3	Compute $IDR$ directly from nonlinear response-history analyses at each site for each model building.
<b>(c) Input variables for vulnerability functions (Part of Step 5 in Figure 1)</b>	
<b>ID</b>	<b>Description</b>
V1,V4	$Sa$ . At each site, $Sa$ corresponds to $Sa_{ij}$ at period $T_{l,h}$ , where model building $h$ is located at site $i$ .
V2	$Sa$ and $\epsilon$ . $Sa$ is defined as above. $\epsilon$ is $\epsilon_{ij}$ , obtained by rearranging Equation 4.2: $\epsilon_{ij} = \frac{Ln(\bar{S}a_{ij}) - Ln(Sa_{ij})}{\sqrt{\sigma_{ij}^2 + \tau_j^2}}$ . $\epsilon_{ij}$ is also computed at the first-mode period of model building $h$ ( $T_{l,h}$ ) located at site $i$ .
V3	$IDR$ . $IDR$ corresponds to $IDR_h$ at site $i$ for model building $h$ , determined from methods E1, E2 or E3.
<b>(d) Methods for determining if a building is collapsed (Part of Step 5 in Figure 1)</b>	
<b>ID</b>	<b>Description</b>
C1	Collapse capacity for each model building $h$ (i.e. $Sa_{h,collapse}$ or $IDR_{h,collapse}$ ) is taken as the median collapse capacity from $IDA$ for model building $h$ . These collapse capacities are reported in Table 2. Input variable(s) is the same as the V method used.
C2	$Sa_{h,collapse}$ or $IDR_{h,collapse}$ is randomly generated at each site from a distribution of collapse capacities obtained from $IDA$ (Table 2) for model building $h$ . Input variable(s) is the same as for the V method used.
C3	$Sa_{h,collapse}$ is randomly generated from the distribution of collapse capacities obtained from $IDA$ for model building $h$ , once for each regional loss realization. New “region-wide” values of $Sa_{h,collapse}$ are generated at the onset of each subsequent regional loss realization. There are a number of variants to C3: If combined with V1, $Sa_{h,collapse}$ is randomly sampled from the $Sa$ -based collapse capacity distribution. If combined with V2 or V4, $Sa_{h,collapse}$ is randomly sampled from the $Sa$ - $\epsilon$ -based collapse capacity distribution, taking $\epsilon_{avg,j}$ as the input $\epsilon$ value. If combined with V3, $Sa_{h,collapse}$ is sampled from the multivariate normal distribution defining the coefficients of the $Sa$ - $IDR$ transformations and collapse capacities.
C4	$Sa_{h,collapse}$ is taken as the median collapse capacity obtained from nonlinear analysis results from the simulated or recorded time histories. The median collapse capacity is computed using logistic regression. $Sa_{h,collapse}$ is “region-wide” and the same at all sites with the same building type.
C5	Collapse is simulated directly at each site with nonlinear dynamic analysis.
C6	Assume no buildings collapse.

#### 4.4.2 Predicting Building Responses (IDRs) at Each Site

We next consider alternative methods for relating ground motion intensity to the building response, specifically *IDRs*, of each building in the portfolio (Step 4b in Figure 4.1). Although most regional loss assessment methods do not directly compute or consider *EDPs* such as *IDR*, we hypothesize that it may improve regional loss assessment for two reasons. First, *EDPs* are better predictors of losses to individual buildings than *IMs*, because the explicit computation of *EDPs* reduces that error in the loss estimation that stems from uncertainty in the distribution of *EDP* given *IM* (*EDP/IM*). Second, *EDPs* could be determined in such a way that spatial correlations in building responses are considered. Accounting for spatial correlations of *EDPs* allows for the possibility that buildings perform better or worse than what is expected (given *IM*) throughout the entire region due to region-wide construction or ground motion frequency content characteristics. We classify this here as inter-event variability of *EDP/IM*.

A number of possible approaches could account for these spatial correlations in building response. Here, we follow the proposed approach of DeBock *et al.* (2013). The method is based on the observation that *EDPs* and *Sa* have similar spatial correlation patterns. This observation implies that *IDRs* can be predicted from *Sa* through a linear transformation, which preserves spatial correlation patterns and provides unbiased predictions of *IDRs* (DeBock *et al.* 2013). These so-called *Sa-IDR* transformations have the form:

$$\text{Ln}[IDR_h] = A_h + B_h * \text{Ln}[Sa_h] \quad 4.3$$

DeBock *et al.* (2013) propose a two-step approach for determining the coefficients  $A_h$  and  $B_h$  for each model building  $h$ . First, each model building  $h$  is subjected to IDA with a large suite of ground motion records and *Sa-IDR* transformations are fitted to results from each record, as in Figure 4.8. The distribution of  $A_h$  and  $B_h$  coefficients describing these transformations can be

shown to follow a multivariate normal distribution, shown in Figure 4.8(b), where the uncertainty in  $A_h$  and  $B_h$  reflects variability in ground motion characteristics and structural response. The second step of the approach uses this multivariate normal distribution to randomly generate coefficients defining  $Sa$ - $IDR$  transformations for each model building. This method accounts for  $\varepsilon_{avg,j}$  of the intensity map  $j$  when sampling  $A_h$  and  $B_h$ , as described by DeBock *et al.* (2013). A single realization of an  $Sa$ - $IDR$  transformation for model building  $h$  is used at every site where that model building is located for a given intensity map. We note here that  $Sa_{h,collapse}$  is also jointly distributed with  $A_h$  and  $B_h$ . Therefore, an expected value of  $Sa_{h,collapse}$  for a region can be sampled at the same time as  $A_h$  and  $B_h$ , which is essential for one of the collapse classifications methods presented later.

Table 4.5(b) summarizes the methods considered here for predicting  $IDRs$ . Method E1 generates random  $Sa$ - $IDR$  transformations by the method proposed by DeBock *et al.* (2013). E2 employs  $Sa$ - $IDR$  transformations for each model building that are back-calculated from nonlinear dynamic time-history analysis results for the earthquake scenario. The back-calculated  $Sa$ - $IDR$  transformations, examples of which are shown for Chi Chi and Shakeout in Figure 4.8(a), are achieved by linearly regressing simulated  $Ln[IDR]$  results for the model building of interest with  $Ln[Sa]$  for all the sites in the region for which recorded or simulated time histories are available. In essence, the E2 method determines the coefficients of the  $Sa$ - $IDR$  transformation that best fit the model building simulation results for that specific scenario. The most robust approach, identified as E3, simulates  $IDRs$  directly from the recorded or simulated ground motion time histories and building simulation models for the model buildings. For buildings located between sites where ground motion time histories are not available,  $IDR$  is linearly interpolated (in natural log space) from data recorded at neighboring sites.

For completeness, we note that methods that use  $Sa$ -based or  $Sa$ - $\varepsilon$ -based vulnerability functions do not explicitly compute  $IDR$  as part of the assessment, instead predicting individual building losses directly from  $Sa$ . Such methods are denoted by E0.

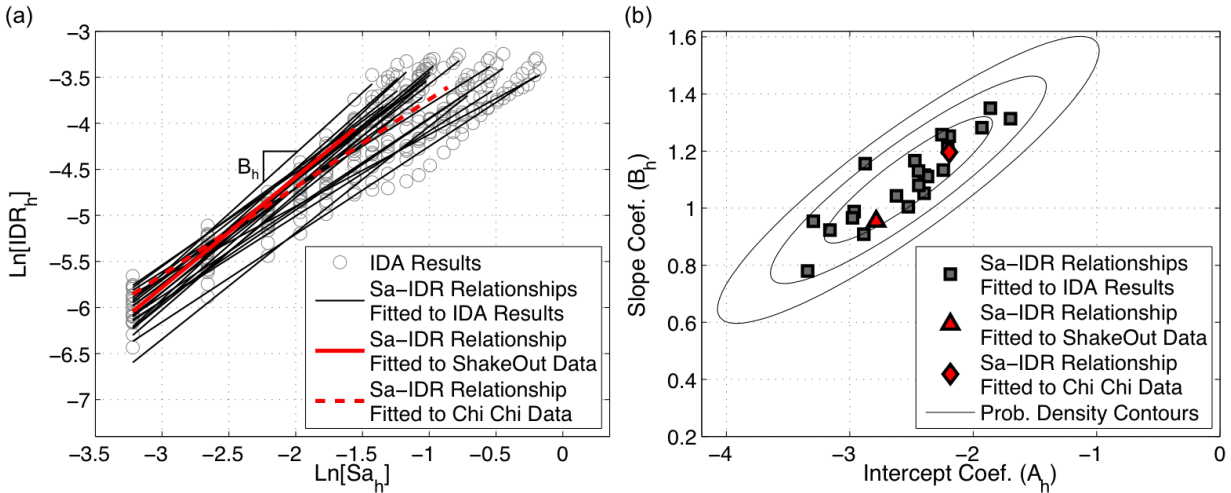


**Figure 4.8. Illustration of  $Sa$ - $IDR$  transformations showing (a)  $Sa$ - $IDR$  transformations for model building no. 4 obtained from IDA for a general set of ground motions (FEMA 2009) and from the ShakeOut and Chi Chi earthquakes and (b) distribution of  $A_h$  and  $B_h$  coefficients describing the  $Sa$ - $IDR$  transformations that are depicted in (a), with contours representing probability densities of the multivariate normal distribution.**

#### 4.4.3 Computing Losses in Individual Buildings

Several methods are explored for computing individual building losses (corresponding to Step 5 in Figure 4.1). As outlined in Table 4.5(c), methods V1-V4 differ in terms of the input to the vulnerability function for determining losses to non-collapsed buildings:  $Sa$ ,  $Sa$ - $\varepsilon$ , or  $IDR$ . In each case, a random loss realization is generated based on the distribution of losses defined by the vulnerability function for the given input (illustrated in Figure 4.7(a)-(b)).

Losses to collapsed buildings are computed probabilistically from the distribution of building replacement costs. The study explores different methods for determining if a building has collapsed, as described in Table 4.5(d). In all cases, a building is collapsed if the demand

(measured by  $Sa$  or  $IDR$ ) exceeds the collapse capacity. Methods differ in how the collapse capacity is obtained and metrics used to define the demand and capacity.

C1 takes the model building collapse capacity as the median collapse capacity that is determined from IDA. In contrast, C2 and C3 randomly generate collapse capacities for each model building, based on the collapse capacity distributions that are determined from IDA. C2 generates the collapse capacity randomly for each model building at each site, whereas C3 generates a single region-wide collapse capacity. In C3, the collapse capacity varies from one regional loss realization to the next, but not from site to site for a given model building  $h$  and intensity map  $j$ . The C4 region-wide collapse capacity for each model building is more precise and computed from the nonlinear structural analysis data for the ShakeOut and Chi Chi time histories. Note that C4 uses only the median  $Sa_{h,collapse}$  from the logistic regression at all sites, rather than sampling from the distribution of collapse capacities for a given model building. Accordingly, C4 can be thought of as the best possible case of C3's region-wide collapse capacity, which, in the case of C4, is informed by time-history analysis for that specific earthquake. Method C5 simulates collapse directly at each site using the time-history analysis results for that specific site. For buildings located between sites with ground motion time-histories, C5 determines collapse based on interpolation of responses from neighboring sites. Finally, C6 assumes none of the buildings collapse. C6 is included to isolate the impacts of different types of vulnerability functions for non-collapsed buildings.

Collapse capacity may be determined from an  $IDR$ -based,  $Sa$ -based, or  $Sa-\varepsilon$ -based collapse capacity distribution. The  $Sa-\varepsilon$  metric for determining  $Sa_{h,collapse}$  deserves the most explanation. In the site-by-site method (C2),  $Sa_{h,collapse}$  is randomly generated from a distribution considering  $\varepsilon_{ij}$  at each site. In the region-wide method (C3), collapse capacities for each model building  $h$  are

based on  $\varepsilon_{avg,j}$  (Equation 4.2). The choice of  $\varepsilon_{avg,j}$  is based on DeBock *et al.* (2013), which showed that unbiased region-wide  $Sa$ - $IDR$  transformations (*i.e.* E3) can be sampled from a multivariate distribution that accounts for  $\varepsilon_{avg,j}$ , and that the  $Sa$ - $IDR$  transformation coefficients ( $A_h$  and  $B_h$ ) are jointly distributed with  $Sa_{h,collapse}$ . These findings imply that region-wide realizations of  $Sa_{h,collapse}$  are also unbiased if they take advantage of additional information provided by  $\varepsilon_{avg,j}$ .

## 4.5 Comparison of Regional Loss Assessment Methods

### 4.5.1 Overview

Loss assessments for the two earthquake scenarios are performed by combining methods, one selected from each group in Table 4.5(a)-(d), and conducting 1000 Monte Carlo regional loss realizations. The evaluation of the methods relies on two categories of comparisons. The first category of comparisons considers only those methods that utilize the ShakeOut and Chi Chi ground motion time histories (*i.e.* methods that involve G4). The metric of interest is the regional loss given these observed time histories, denoted  $[RL/TH]$ . Although none of these methods are feasible for prospective prediction of losses, their evaluation permits direct comparisons of  $Sa$ ,  $Sa$ - $\varepsilon$ , and  $IDR$ -based approaches in regional loss assessment. Values of  $[RL/TH]$  obtained through the different methods are compared to the results from the G4-E3-V3-C5 method. G4-E3-V3-C5 computes losses from nonlinear time-history structural response analyses performed for each building site, providing the most robust estimate of the ShakeOut and ChiChi losses and a “benchmark” for the evaluation of the other methods. Comparisons of  $[RL/TH]$  are made primarily on the basis of median values. Variation in the prediction of  $[RL/TH]$  is due to uncertainty in the vulnerability functions, and, in some cases, collapse capacities. Note that these comparisons are made with respect to the benchmark result, which does not represent the true

loss due to uncertainties and/or biases in modeling, vulnerability functions and other assumptions. Indeed, historical data to which the benchmark may be compared are lacking. However, since the same building simulation models and time-history response data are used to develop all of the regional loss methods, sources of bias affecting the benchmark result are equally present in the other methods, so relative comparisons to the benchmark are still valuable.

The second class of comparisons quantifies the regional losses predicted by the various methods for the ShakeOut and Chi Chi earthquake magnitude ( $M$ ) and rupture ( $R$ ) location,  $[RL/M,R]$ . As such, comparisons of  $[RL/M,R]$  are not intended to determine how well different methods predict the benchmark losses for ShakeOut and Chi Chi, but, rather, how well they predict the distribution of possible losses that could occur. The distributions of  $[RL/M,R]$  obtained by the different methods are evaluated in relation to the distribution obtained from the best, so-called “High-end”, method. The characteristics of the High-end method are identified from the first class of comparisons. Comparisons of the distributions of  $[RL/M,R]$  are made with respect to the median, interquartile range (25<sup>th</sup> to 75<sup>th</sup> quantile), and 5-95 quantile range (5<sup>th</sup> to 95<sup>th</sup> quantile). Variation in the prediction of  $[RL/M,R]$  stems from uncertainty in intensity maps, vulnerability functions, and replacement costs and, in some cases,  $Sa$ - $IDR$  transformations and collapse capacities.

Due to the large number of building stocks and regions on which regional loss methods are tested, the results presented below typically provide one representative example. Unless otherwise stated, similar results are observed for all of the building stocks and regions. We emphasize that numerical values of the loss estimates are used for comparison purposes only, and not for judgment about the risk in a particular region. Only those combinations of methods that are pertinent to the conclusions of this study are presented.

#### 4.5.2 Comparisons of IM-based and EDP-based Methods for Non-Collapsed Buildings

We begin by comparing four loss assessment methods that rely on either  $Sa$  or  $IDR$  for computing losses. This comparison focuses on the first metric,  $[RL / TH]$ , so all of the methods use the ground motion time-history data; *i.e.* in all cases, the intensity map is computed directly from the ground motion accelerograms produced by the historical events. The first two methods, the benchmark (G4-E3-V3-C5) and G4-E2-V3-C5, are  $IDR$ -based. Both use the  $IDR$ -based vulnerability functions, taking  $IDR_{max}$  for all stories of the building as input; the only difference between these two methods is that, in the second,  $IDRs$  are computed from event-specific  $Sa-IDR$  transformations, as compared to nonlinear time-history analysis at each site for the benchmark. The two  $Sa$ -based methods rely on  $Sa$  only (G4-EO-V2-C5) and  $Sa$  and  $\varepsilon$  (G4-EO-V1-C5) as inputs for vulnerability functions. These comparisons examine the ductile model buildings nos. 1-3 and all use collapse identification technique C5, so that the different results are due only to differences in the information that is used for non-collapsed buildings. The nonductile model buildings (nos. 4-6) are excluded because their contribution to regional losses is dominated by collapse.

Figure 4.9 presents boxplots of the distributions of  $[RL / TH]$  predicted. Method G4-E2-V3-C5, an  $IDR$ -based method, produces median regional loss estimates that are closest to the benchmark (within 5%). In contrast, the two  $Sa$ -based methods vary substantially from the benchmark, producing median values of  $[RL / TH]$  as much as 25% different. This result implies that  $Sa-IDR$  transformations used in G4-E2-V3-C5 provide additional useful information for computing regional losses that is not accounted for in either of the  $Sa$ -based methods.

Comparing now only the two  $Sa$ -based methods in Figure 4.9, the results show that the  $Sa-\varepsilon$ -based method (G4-EO-V2-C5) typically outperforms the  $Sa$ -based method (G4-EO-V1-C5) in

matching the median benchmark results, but the difference is neither consistent nor overwhelming. When the spectral shapes of the recorded ground motion time histories are consistent with the values of  $\varepsilon_{ij}$  that are computed for the ground motion time histories at the building's first-mode period (*i.e.* when  $S_a$  values computed for the time history at other periods are similar to what is expected based on  $\varepsilon_{ij}$ ),  $S_a$ - $\varepsilon$ -based vulnerability functions provide better estimations of building losses, as in Figure 4.9(a). However, for cases where the spectral shapes of the recorded ground motions differ from the average shape predicted by  $\varepsilon$ , conditioning losses on  $\varepsilon$  can worsen the loss estimation, as shown in Figure 4.9(b).

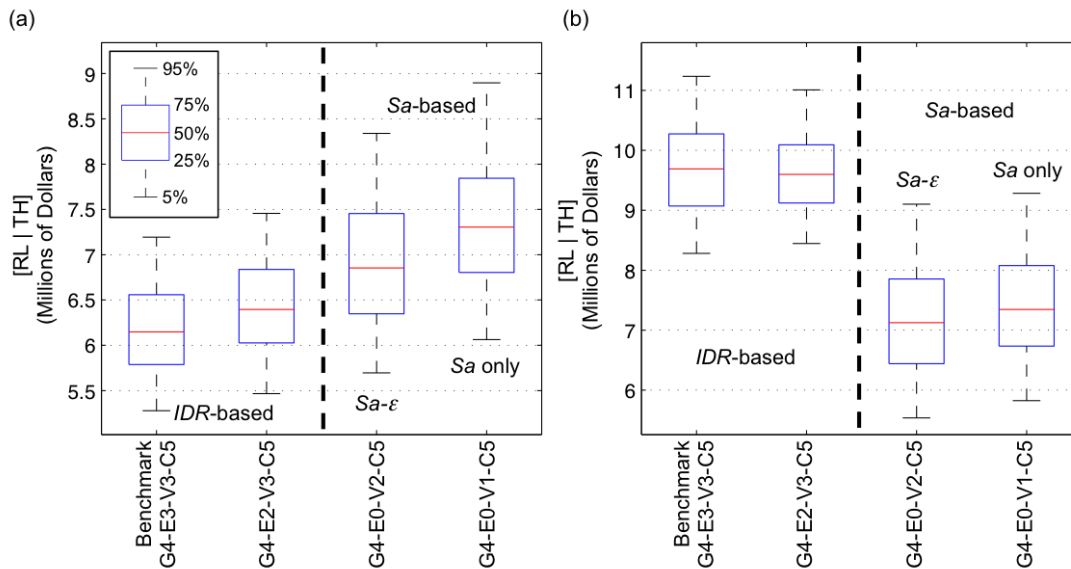


**Figure 4.9. Distributions predicted for  $[RL/TH]$  for the ShakeOut large region and sparse building stock, comparing  $IDR$ -based and  $S_a$ -based methods for loss for all buildings represented by (a) model building no. 1 (28 buildings) and (b) model building no. 2 (16 buildings).**

These first comparisons show that the accuracy of regional loss assessment is increased by accounting for  $IDR$ , indicating that the  $S_a$ - $IDR$  transformations are a critical component of a High-end method. We now examine distributions of  $[RL/M,R]$  that are computed by methods that do not rely on the recorded or simulated time histories. Specifically, an  $S_a$ - $IDR$

transformation method, G3-E1-V3-C6, which is considered the most robust based on the evidence described above, is compared to four methods that do not directly consider *IDR* in the assessment. These four methods fall into two categories. The first category is composed of methods that are *Sa*-based and consider spatial correlations in the development of intensity maps. Of these, G3-E0-V2-C6 is *Sa- $\varepsilon$* -based, while G3-E0-V1-C6 is solely *Sa*-based. The second group does not consider spatial correlations (G2-E0-V2-C6; G2-E0-V1-C6) and differs only by whether  $\varepsilon$  is considered. We assume in all cases that none of the buildings are collapsed (C6), so that differences due to collapse classification do not affect the comparison.

Figure 4.10 shows that each method produces similar median  $[RL/M,R]$  losses (within 10% of each other and the *IDR*-based method). However, methods that consider spatial correlations of ground motion intensity (G3) exhibit much larger variability compared to the G2 methods, as demonstrated by G3's interquartile and 5-95 quantile ranges in Figure 4.10 that are more consistent with that of the *IDR*-based method. Since the G2 methods consistently predict excessively narrow distributions of regional loss, they are not considered beyond this point.

The *IDR*-based method (G3-E1-V3-C6) produces the largest interquartile and 5-95 quantile ranges of  $[RL /M,R]$ , because it accounts for spatial correlations in ground motion intensity and building responses. By including *IDR* correlations, it accounts for inter-event variability in *IDR/Sa*, which results in a larger range of potential regional loss. Among the *Sa*-based methods that account for spatial correlations of ground motions, the method that conditions losses on  $\varepsilon$  (G3-E0-V2-C6) leads to predictions with less variance than the method that does not (G3-E0-V1-C6). The solely *Sa*-based method introduces an additional source of variability by not accounting for the spectral shape of ground motions through the parameter  $\varepsilon_{ij}$  in the prediction of losses. Neglecting to account for  $\varepsilon_{ij}$  widens the inter-quartile and 5-95 quantile ranges, due to

over-predicting large losses and under-predicting small losses. Large losses (like those represented by the 75<sup>th</sup> and 95<sup>th</sup> quantiles) occur when  $Sa$  values are large. When  $Sa$  values are large,  $\varepsilon$  tends to be positive, which reduces the predicted loss for a given  $Sa$ . If  $\varepsilon$  is not considered, the loss given  $Sa$  is over-predicted for large  $Sa$  values. The reverse is true when  $\varepsilon$  is negative. Observe, however, that the magnitude of the additional variance from not considering  $\varepsilon$  is similar to the magnitude of the additional variance that results from considering spatial correlations among  $IDRs$ , as evidenced by the agreement between the interquartile and 5-95 quantile ranges of methods G3-E1-V3-C6 and G3-E0-V1-C6 in Figure 4.10. As a result, the solely  $Sa$ -based method produces the most similar distribution of  $[RL/M,R]$  to the  $IDR$ -based method, but is “right, for the wrong reason.”<sup>9</sup>

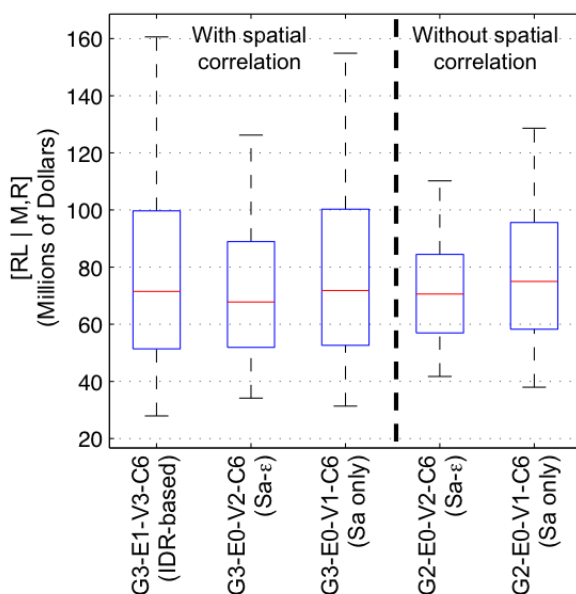


**Figure 4.10. Distributions predicted for  $[RL/M,R]$  for the Chi Chi large region 2 and sparse building stock, comparing four  $Sa$ -based methods to an  $IDR$ -based method.**

<sup>9</sup> Explicitly considering spatial correlations of  $IDRs$  increases the interquartile and 5-95 quantile ranges of  $[RL/M,R]$  by 5-15%. Accounting for the average spectral shape of ground motions in the event by conditioning losses and collapse capacities on  $\varepsilon_{avg,j}$  decreases the range of  $[RL/M,R]$  by 5-15%. These effects are both always of moderate significance, and always have opposing effects on variance. We find no systematic reason why either of these two observations would differ for other regions and building stocks.

### 4.5.3 Comparisons of Methods to Identify Collapsed Buildings

Methods for identifying collapsed buildings are organized to answer the following questions. First, how important is the collapse method to the overall accuracy of the regional loss assessment? Second, what are the differences between methods that randomly generate the collapse capacity of a model building a single time for each regional loss realization (*i.e.* region-wide collapse capacity, C3) and those that randomly generate collapse capacities at each site (C2)? Finally, how does quantifying model building collapse capacity by  $Sa_{h,collapse}$  with and without considering  $\varepsilon$  impact the results?

Figure 4.11 examines these questions by comparing predictions of  $[RL/TH]$  when different collapse identification methods are employed. These results show that methods that predict fractions of collapsed buildings similar to the benchmark also predict losses that are similar to the benchmark. In addition, the impacts of utilizing different vulnerability functions (indicated by the notation of V1 vs. V2 vs. V3 in Figure 4.11) are negligible when compared to the impacts of the collapse classification method. The sensitivity of the regional loss assessment to collapse comes from the large part of the regional loss that is associated with the cost of replacing collapsed buildings. Any region in which a subset of buildings poses a significant collapse risk, like the nonductile concrete buildings in this study, is likely to show a similar sensitivity.

Second, we consider the comparison of site-by-site and a region-wide collapse capacities. Figure 4.11 shows that the region-wide median value of collapse capacity computed from logistic regression of time history results (C4), is the best predictor of the benchmark collapses and losses<sup>10</sup>. Indeed, in Figure 4.11(b), C4 classifies approximately twice as many buildings as

---

<sup>10</sup> It is difficult to verify whether the benchmark prediction for the fraction of collapsed mid-rise nonductile RC moment frame buildings for the large region 2 is consistent with the performance of those buildings in the historical

collapsed as the C2 methods. This discrepancy demonstrates that inter-event variability of collapse capacity strongly impacts the number of collapsed buildings in a region. C2 methods fail to account for inter-event variability of collapse capacity because they generate collapse capacity on a site-by-site basis, assuming that typical collapse capacities throughout the region are distributed about their expected value. On the other hand, C3, of which C4 is the benchmark example because it uses the event time histories, can capture inter-event variability of collapse capacity, because it samples region-wide collapse capacities at the onset of each realization. Note in Figure 4.11 that the median fraction of collapsed buildings predicted by C3 is similar to the C2 methods, but that the fraction of buildings that collapsed in the benchmark analysis (0.77) lies within the range of the C3 predictions. Therefore, we conclude that C3 methods are superior to C2 methods for classifying collapsed buildings.

We now address the question, “how should region-wide collapse capacities be computed?” in Figure 4.12, focusing on comparing C2 and different versions of the C3 method for predicting  $[RL/M,R]$ . The C3 variants differ in terms of the parameters used to define the collapse capacity distribution, specifically whether the collapse distribution is  $S_a$ -based or  $S_a-\varepsilon$ -based (see Table 3(d)). The C2 site-to-site methods are included in Figure 4.12, even though Figure 4.11 showed they are less accurate for  $[RL/TH]$ , because the possibility that they produce a reasonable distribution of collapses for  $[RL/M,R]$  is not ruled out. For the purpose of this evaluation, recall that the most robust method for computing losses to non-collapsed buildings explicitly predicts  $IDR$  through region-wide  $S_a-IDR$  transformations (E1) and computes building losses with  $IDR$ -based vulnerability functions. On the basis of these observations, G3-E1-V3-C3 is identified as

---

Chi Chi earthquake. However, the large region 2 did experience particularly intense ground shaking and Tsai et al. 2000 found that nonductile RC frames performed poorly in the Chi Chi earthquake; therefore the large fraction (~0.77) of the mid-rise nonductile RC frame buildings that collapse in the benchmark analysis seems reasonable.

the most robust regional loss assessment method and is hereafter referred to as the High-end method. Since the High-end method generates  $Sa$ - $IDR$  transformations and collapse capacities for all the model buildings from a joint multivariate distribution, it accounts for cross-correlations between the different model buildings, in terms of  $Sa_{h,collapse}$  and inter-event variability of  $IDR/Sa$ . Spatial correlations of collapse cases are also realistic, as a result of the spatially correlated fields of  $Sa_{ij}$  that are used to represent ground motion intensity, which is the input variable for determining collapse. The other variants of C3, as well as the C2 methods, do not require the user to construct a covariance matrix from IDA data.

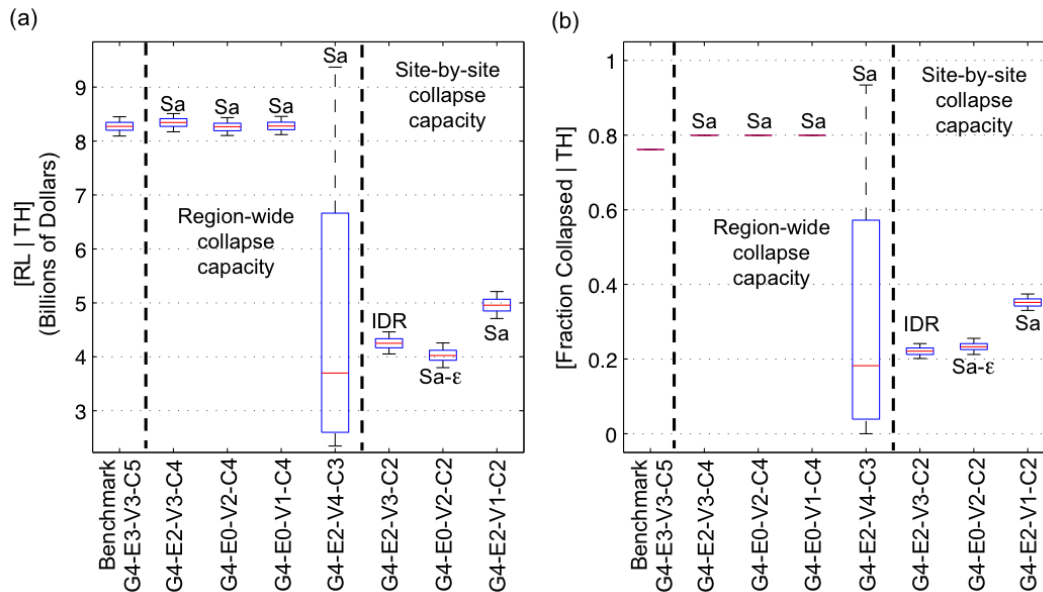


**Figure 4.11. (a) Distributions predicted for  $[RL/TH]$  for the Chi Chi large region 2 and buildings represented by model building no. 5 in the sparse building stock, comparing methods for identifying which buildings have collapsed, and showing (b) fraction of collapsed buildings computed by the different methods. The annotation of  $Sa$ ,  $\epsilon$  and  $IDR$  describes the input for determining collapse.**

Figure 4.12 shows that the site-to-site and region-wide  $Sa$ -based only methods (G3-E0-V1-C2 and G3-E0-V1-C3) predict collapse classifications that are similar to the High-end method. However, the  $Sa$ -based methods overestimate the median and upper quantiles of the distribution of collapsed buildings by 5%-25%. This overestimation stems from realizations that produce

large  $Sa$  values at a number of sites. In reality, sites with large  $Sa$  tend to also have positive  $\varepsilon$ . Neglecting to account for this positive  $\varepsilon$  erroneously increases the fraction of buildings that are classified as collapsed. Figure 4.12 also shows that method G3-E0-V2-C3, which computes region-wide  $Sa_{h,collapse}$  at the onset of each regional loss realization that are conditioned on  $\varepsilon_{avg,j}$ , produces similar probabilistic collapse classifications to the High-end method. There is only one difference between G3-E0-V2-C3 and the High-end method in terms of collapse classification; the High-end method considers collapse capacity as part of a joint distribution along with  $Sa$ - $IDR$  transformation coefficients, whereas method G3-E0-V2-C3 does not utilize  $Sa$ - $IDR$  transformations. As a result, method G3-E0-V2-C3 does not explicitly consider cross-correlations in  $Sa_{h,collapse}$  between different buildings  $h$ . However, most of the cross-correlations in  $Sa_{h,collapse}$  are accounted for by cross-correlations of  $\varepsilon_{avg,j}$  at different first-mode periods for the same intensity map  $j$ . Since both approaches employ  $\varepsilon_{avg,j}$ , G3-E0-V2-C3 produces collapse classification realizations that are similar to the High-end.

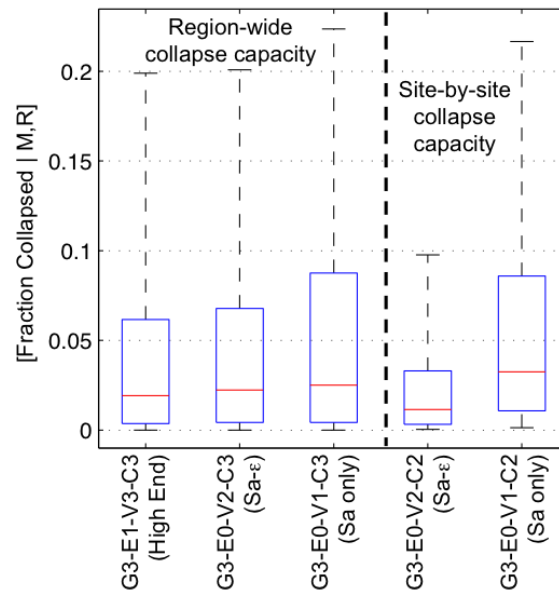


**Figure 4.12. Fractions of buildings collapsed for the ShakeOut large region and dense building stock, comparing collapse classification methods that consider  $Sa$  vs.  $Sa$ - $\varepsilon$  and those that generate region-wide vs. site-by-site collapse capacities.**

#### 4.5.4 Sensitivity of Predicted Regional Loss Distributions to Other Methodological Choices

The objective of this section is to determine how sensitive the probabilistic regional loss distributions  $[RL/M,R]$  are to uncertainty of vulnerability functions, replacement costs and certain building stock characteristics. For these studies, losses are computed by method G3-E0-V4-C3. This method computes losses from spatially correlated intensity maps,  $S_a$ -based vulnerability functions, and region-wide collapse capacity realizations generated from a  $S_a$ - $\epsilon$ -based distribution. G3-E0-V4-C3 is relatively simple, but, when compared to the High-end method in Section 4.5.5, is found to produce very similar loss assessments (<5% difference in the median and interquartile/5-95 quantile ranges).

##### 4.5.4.1 Sensitivity to Variability of the Vulnerability Functions and Replacement Costs

Each loss assessment up to this point has accounted for the variability of vulnerability functions and replacement costs for computing regional losses by treating these quantities probabilistically. The natural question is, “how influential is vulnerability function and replacement cost variability to the total variability of  $[RL/M,R]$ ?” The deterministic loss computation uses the expected value of the vulnerability function or the expected value of the replacement cost as the building loss.

Figure 4.13 shows that treating vulnerability functions and replacement costs probabilistically or deterministically has negligible impact on the median, interquartile range, or 5-95 quantile range of  $[RL/M,R]$ , with less than 3% difference for any quantity. These results imply that regional loss variability is dominated by event-to-event variability of the ground shaking intensity, not by uncertainty of vulnerability functions and replacement costs. Similar

results are expected for any portfolio with more than a couple of buildings if deviations from the expected values of repair and replacement costs are non-systematic (*i.e.* each building's deviation from the expected repair or replacement cost is independent of the others). This expectation follows directly from the observation that the coefficient of variation of a sum of random variables (*e.g.* regional loss) decreases as the number of random variables (*e.g.* individual building losses) increases (Montgomery and Runger 2007). In a sensitivity study, the authors find that the distribution of regional losses is relatively insensitive to the variability of the vulnerability functions and replacement costs for building stocks with as few as five buildings.

Systematic deviations of repair and replacement costs from the expected value are still expected to impact the variance of regional loss, because costs for each building will tend to all be higher or all be lower than the expected values throughout a region, thereby expanding the range of possible regional loss outcomes. Correlations in contractor costs and demand surge are factors that may cause systematic deviations of repair and replacement costs. For example, demand surge is expected to increase costs by 20% or more for large-scale disasters (Olsen and Porter 2011), but is much less significant for small-scale disasters. Therefore, accounting for demand surge would increase of the 75<sup>th</sup> and 95<sup>th</sup> regional loss quantiles (and possibly the median) by 20% or more, but would have little effect on the 5<sup>th</sup> and 25<sup>th</sup> quantiles. As a result, demand surge is expected to significantly increase the variance in regional loss.

#### 4.5.4.2 *Sensitivity of Regional Losses to Building Locations*

The precise distribution of buildings within a region may be difficult to determine (Vasudevan *et al.* 1992, Bal *et al.* 2010). For example, the resolution of the building stock data gathered in this study locates buildings by zip code, but contains no information regarding the

building locations within each zip code. This begs the question about the locational precision required in estimating building locations for the purpose of regional loss assessment. Bal *et al.* (2010) demonstrate that the spatial resolution of building stock data impacts the variance of regional loss, but not the expected value, and that increasing the geographical resolution of building locations reduces the regional loss variance, but with diminishing effects when site resolution is less than approximately a mile.

In this study we hold spatial resolution constant, but vary the locations of buildings within the region. The influence of these uncertainties associated with lack of knowledge about actual building locations on  $[RL/M,R]$  is explored by examining ten different realizations of the Chi Chi large region 1 and sparse building stock. Each stock has the same total square footage of each building type. Five of these building stocks distribute the buildings randomly throughout the region and are referred to as R1-R5. Five additional stocks (S0-S4) cluster the entire building inventory into a sub-region approximately 2 mi. x 3 mi. in one corner or near the center of the region, as shown in Figure 4.5.

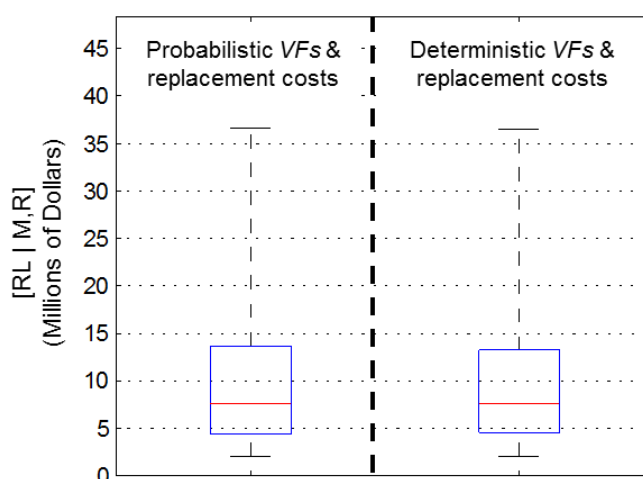


**Figure 4.13. Distributions predicted for  $[RL/M,R]$  for the ShakeOut small region and sparse building stock (18 buildings), comparing methods that incorporate probabilistic and deterministic techniques for computing individual building losses. Losses are computed by G3-E0-V4-C3.**

The similarities between the medians and ranges of the loss assessments for the randomized building stocks in Figure 4.14 indicates that the precise location of each building is not necessary for computing the distribution regional losses. Clustering of buildings, as illustrated by sub-regions S0-S4, impacts the median and ranges of the regional loss substantially, by more than 100% in some cases. The median is affected, because clusters located closer to the fault rupture tend to experience greater losses than more distant clusters. Clustering also impacts the ranges of the losses, because locating buildings closer to one another increases correlations of their losses, which increases the variance of the regional loss predictions.<sup>11</sup> These observations suggest that it is important to account for clustering of buildings into sub-regions when such a phenomenon is likely to occur, such as in dense downtown areas, but that a single realization of the building stock is sufficient for computing regional losses.

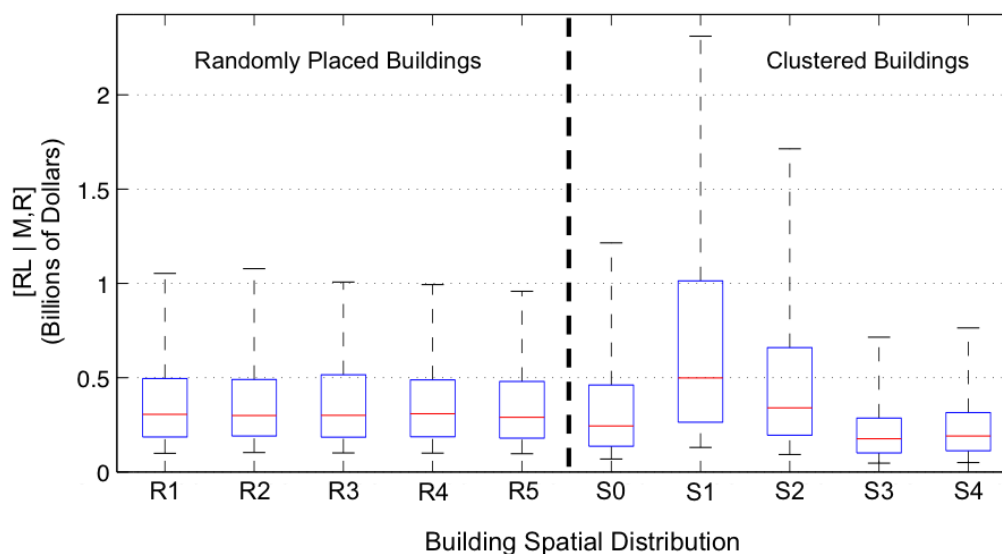


**Figure 4.14. Distributions predicted for  $[RL/M,R]$  for the Chi Chi large region 1 for sparse building stocks with the same buildings, but different spatial distributions. Losses are computed by G3-E0-V4-C3.**

<sup>11</sup> Although S3 and S4 have smaller ranges of loss, the coefficients of variation of the losses are still larger than for the regions where buildings are randomly distributed throughout the entire large region (R1-R5).

For a full analysis that considers multiple faults and probable rupture locations, we hypothesize that the importance of building cluster locations in the exposed inventory may be reduced in some cases. This hypothesis is based on the assumption that the location of the cluster matters less if multiple faults contribute to the regional hazard. However, when soil conditions vary significantly throughout a region, it will still be important to know where a cluster of buildings is located in order to represent soil conditions correctly for predicting  $Sa_{ij}$ . In our test regions, the variability of soil conditions is not large enough for locations of building clusters to have a significant impact for analyses in which multiple fault rupture locations are considered. However, for regions in which there is large variability in soil conditions, such as some regions near the San Francisco Bay in California (USGS 2010), the impact could be significant.

#### 4.5.4.3 Sensitivity of Regional Losses to Building Classification

Next, we examine the effects of building height and capacity misclassifications of the building stock on  $[RL/M,R]$ . Nine additional versions of the ShakeOut small region and dense building stock are created, each of which has the same gross building square footage as the original building stock, but with different attributes.

Five of the new building stocks contain height misclassifications, but maintain the same capacity (*i.e.* strength and ductility) classifications as the original building stock, which are representing by either modern or older RC frame buildings. Height misclassifications are introduced in the first case by reclassifying half of the mid-rise building square footage as low-rise and the other half as high-rise. The results in Figure 4.15 demonstrate that considering only two height classes (low and high), rather than three, yields an almost identical regional loss distribution to that of the original building stock. The next three building stocks assume that all of the buildings are classified as low-rise, mid-rise, or high-rise. Condensing the entire building

stock to a single height category increases the 5-95 quantile range of regional losses by as much as 20%, due to building losses being excessively correlated as a result of all of buildings belonging to the same height category. Aslani *et al.* (2012) also observed that less diverse building stocks have greater regional loss variation than diverse building stocks. A final building stock divides the gross square footage equally between the three height classes. This division overestimates the low-rise and mid-rise square footage, while under-estimating the high-rise square footage (refer to Figure 4.3). However, all quantiles of the resulting regional loss distribution closely resembles that of the original building stock (less than 5% different).

The four building stocks with capacity misclassifications have the same height distribution as the original stock, but misclassify 25%, 50%, 75%, or 100% of the older (lower ductility and strength capacity) buildings as modern (higher ductility and strength capacity). Misclassifications of capacity have a strong impact on regional losses, as demonstrated by Figure 4.15. Older nonductile buildings account for a significant portion of the regional loss. Therefore, the entire regional loss distribution reduces (*i.e.* each quantile is lower) when older buildings are misclassified as newer. In fact, median losses are predicted to reduce by roughly 50% for the ShakeOut earthquake small region and dense building stock if all of the buildings are assumed to be modern. Capacity misclassifications other than those having to do with year of construction, such as assuming the wrong structural system (*e.g.* RC shear walls versus RC moment frames), are expected have similar impacts on the regional loss distribution.

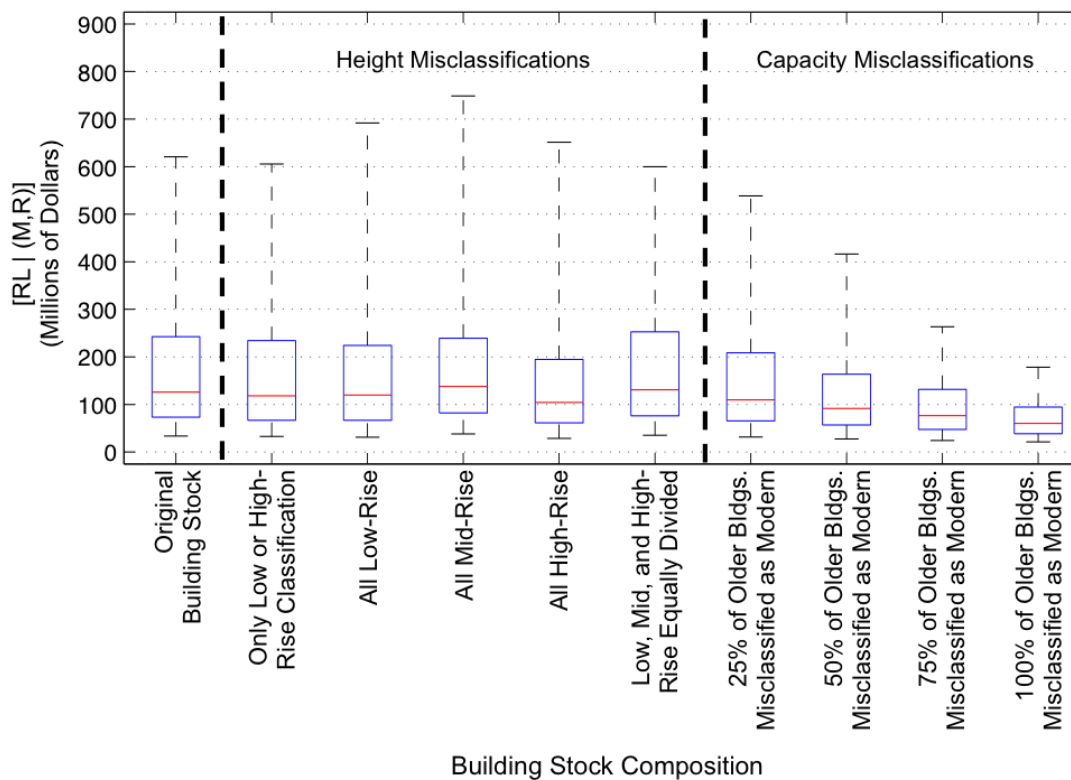


**Figure 4.15. Distributions predicted for  $[RL/M,R]$  for the ShakeOut small region and dense building stock, examining building height and capacity misclassifications. Losses are computed by G3-E0-V4-C3.**

Based on these observations, we conclude that accurate classification of building capacity is crucial for obtaining accurate regional loss predictions. In most building inventory data, building capacity is represented by classifications defined by building year and structural system (Bal et al. 2008). However, height misclassifications are not expected to significantly impact the results of probabilistic regional seismic loss assessments, and a couple of gross height categories can likely be used to represent the regional exposure of buildings of different types<sup>12</sup>.

<sup>12</sup> Building classes for which height and capacity are strongly correlated would be an exception to this observation.

#### 4.5.5 Recommended Methods for Computing Regional Building Loss

A primary objective of this study is to recommend methods for regional seismic loss assessment. The High-end method (G3-E1-V3-C3) is developed based on observations from previous sections. This method begins each regional loss realization by developing a map of spatially correlated ground motion intensities, since accounting for spatial correlations is essential for predicting the distribution of  $[RL/M,R]$ . For non-collapsed buildings,  $IDRs$  are computed from a  $Sa-IDR$  transformation for each model building  $h$ , the coefficients of which are randomly generated for each regional loss realization. Losses are computed with  $IDR$ -based vulnerability functions. Collapsed buildings are identified by a region-wide collapse capacity. The random variables representing the coefficients of the  $Sa-IDR$  transformations and the collapse capacities for different buildings are sampled from a multivariate normal distribution that depends on  $\varepsilon_{avg,j}$ .

Since the High-end method is time-consuming, two alternative methods are also proposed. These methods are described as “simplified,” because they compute losses without considering  $EDPs$  explicitly. Simplified<sub>1</sub> corresponds to G3-E0-V4-C3. Like the High-end method, it begins by generating a suite of intensity maps that consider spatial correlations of  $Sa$ . However, losses for non-collapsed buildings are computed from  $Sa$ -based vulnerability functions. To identify collapsed buildings, region-wide realizations of collapse capacity are sampled from each model building’s  $Sa$ - $\varepsilon$ -based collapse capacity distribution at the onset of each regional loss realization, considering  $\varepsilon_{avg,j}$  for intensity map  $j$ . The features of Simplified<sub>1</sub> are motivated by previous observations, first, that loss distributions require spatially correlated intensity maps. Second, distributions of  $[RL/M,R]$  for non-collapsed buildings in a region are estimated well by  $Sa$ -based vulnerability functions. However, implementing  $Sa$ -based vulnerability functions does not

account for the small increase in variance that is due to inter-event variability of  $IDR/Sa$ , nor does it account for the small decrease in variance that results from considering  $\varepsilon_{avg,j}$ . The misestimations that result from ignoring both of these sources systematically cancel each other out, making the distribution of  $[RL/M,R]$  obtained by  $Sa$ -based only methods “right for the wrong reason.” Third, the best method for identifying collapsed buildings utilizes region-wide realizations sampled from  $Sa$ - $\varepsilon$ -based collapse capacity distributions.

The Simplified<sub>2</sub> method is G3-E0-V1-C2. It is identical to Simplified<sub>1</sub>, except in terms of the collapse identification method. In Simplified<sub>2</sub>, collapse capacities for each model building  $h$  are based on a  $Sa$ -only distribution and are randomly generated on a site-by-site basis. Although less robust than the Simplified<sub>1</sub> and High-end methods, Simplified<sub>2</sub> is appealing because losses due to building damage and collapse are computed from a single intensity measure,  $Sa$ . In doing so, Simplified<sub>2</sub> is consistent with  $Sa$ -based vulnerability functions that do not explicitly distinguish between collapsed and non-collapsed cases.

Figure 4.16 compares the distributions of  $[RL/M,R]$  predicted by the Simplified and High-end methods. Looking first at the results for Simplified<sub>1</sub>, the median and lower quantiles are very similar to the High-end method (errors range from 0-5% for most of the building stocks and regions), and the values of the 75<sup>th</sup> and 95<sup>th</sup> quantiles are on the order of 0-10% different than the High-end method. Simplified<sub>2</sub> computes 5<sup>th</sup> and 25<sup>th</sup> quantiles of  $[RL/M,R]$  that are typically within 10% of the High-end method, but the losses at the median and upper quantiles are generally 5-25% higher than the High-end. The errors in Simplified<sub>2</sub> are predominantly due to under-predicting building collapse capacities when  $Sa$  is large and  $\varepsilon$  is positive.

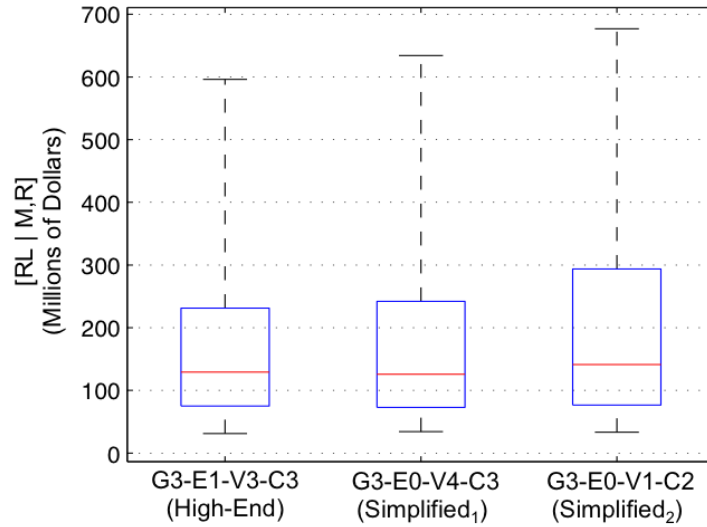


**Figure 4.16. Distributions predicted for  $[RL|M,R]$ , comparing Simplified and High-end methods for the ShakeOut small region and dense building stock.**

We also acknowledge a plausible Simplified<sub>3</sub> method, which does not align precisely with any of the methods described in Table 3. Simplified<sub>3</sub> classifies collapsed buildings in the same manner as Simplified<sub>1</sub>. For non-collapsed buildings, Simplified<sub>3</sub> computes losses with  $Sa$ - $\varepsilon$ -based vulnerability functions that take  $Sa$  and  $\varepsilon_{avg,j}$  as input. These vulnerability functions are then shifted to account for inter-event variability of  $IDR/Sa$ . Mechanically, this shift in the vulnerability function is accomplished by generating a realization of a standard normal random variable at the onset of each regional loss realization  $j$ . This realization is then multiplied by the standard deviation of the vulnerability function that is due to uncertainty in  $IDR/Sa$  ( $\sigma(VF)_{IDR|SA}$ ), essentially modifying the distribution to be consistent with the computed inter-event variability.

Figure 4.17 shows that Simplified<sub>3</sub> is indeed promising and produces results that are similar to the High-end and Simplified<sub>1</sub> methods when used for a single model building. In this example, the loss associated with every quantile of the regional loss distribution obtained by the Simplified<sub>3</sub> method is within 5% of that obtained by the High-end method. However,

implementation of Simplified<sub>3</sub> for a regional loss assessment with many model building types is difficult. First, it requires vulnerability functions that account for  $\varepsilon$ . Second, the analyst must compute the portion of the standard deviation of the vulnerability function that is due to variability of  $[IDR/Sa, \varepsilon]$ . Third, the shifted vulnerability functions should be correlated between the different model buildings. To determine these correlated shifts of the vulnerability functions for different model buildings, suites of  $Sa$ - $IDR$  relationships are required. Thus, there is no reduction in computational effort compared to the High-end method.

If a simpler approach to probabilistic regional loss assessment than the High-end method is desired, the comparison here recommends Simplified<sub>1</sub>. Simplified<sub>1</sub> produces distributions of  $[RL/M, R]$  that are similar to the High-end method, but is “right for the wrong reason” (see Section 4.5.2). The advantage of Simplified<sub>1</sub> is that it does not require considering  $EDPs$  directly in the assessment, which can be difficult. Simplified<sub>2</sub> is conducive to use with vulnerability functions that are based on  $Sa$  and do not distinguish between collapsed and non-collapsed buildings, making it an attractive method for analysts who already have such vulnerability functions available. However, Simplified<sub>2</sub> over-predicts the occurrence of building collapse for strong shaking events (*e.g.* large magnitude events with high  $Sa$  and positive  $\varepsilon$  at many sites), so it is conservative. The Simplified<sub>3</sub> method is robust, but too complex for current implementation. Nevertheless, a new library of vulnerability functions may make Simplified<sub>3</sub> an optimum choice in the future.

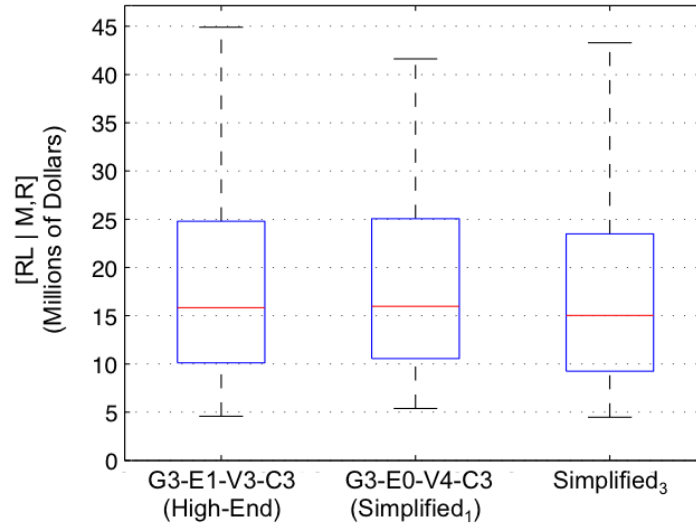


**Figure 4.17. Distributions predicted for  $[RL|M,R]$ , comparing Simplified<sub>3</sub> to the High-end and Simplified<sub>1</sub> methods for buildings for loss from all buildings represented by model building no. 2 in the Chi Chi large area 2 and sparse building stock.**

## 4.6 Conclusions

Several different methods for Monte Carlo-based probabilistic regional (portfolio) loss assessment are implemented for case-study building stocks and earthquake scenarios. Findings are based on a stock of ductile and nonductile reinforced concrete moment frame buildings ranging in height from two to eight stories. On the basis of these investigations, the study concludes that the most important factors to consider in probabilistic regional seismic loss assessments are: (1) spatial correlations of ground motion intensity; (2) regional versus site-to-site methods for collapse classification; (3) accurate characterization of building capacity, especially strength and ductility; (4) spatial clustering of buildings if such clusters exist in the inventory. Each of these factors significantly impacts the variance of regional loss predictions.

Based on comparisons to a Benchmark method, which estimates building responses via nonlinear dynamic time-history analysis, a High-end method is recommended. The High-end method follows a procedure developed by DeBock *et al.* (2013). It begins by generating random

realizations of ground motion intensity maps from a ground motion prediction equation (GMPE), considering spatial correlations of ground motion intensity, which is achievable with existing spatial correlation models. This and past studies have demonstrated the importance of considering spatial correlations among ground motion intensities for assessing regional losses probabilistically. Next, the High-end method uses spectral acceleration at the first-mode period of each model building  $h$  ( $Sa_h$ ) to predict interstory drift ratio ( $IDR_h$ ) at each site through region-wide “ $Sa$ - $IDR$  transformations”. This step explicitly accounts for spatial correlations among  $IDR$ , as well as inter-event variation of  $IDR/Sa$ , and is found to broaden the distribution of the regional loss that is estimated for a given fault rupture. Losses for non-collapsed buildings are computed with  $IDR$ -based vulnerability functions. Collapsed buildings are identified by a region-wide collapse capacity for each model building  $h$  ( $Sa_{h,collapse}$ ), which is generated at the onset of each new intensity map realization. The High-end method samples the region-wide  $Sa_{h,collapse}$  for all model buildings at the same time that it generates transformation equations for converting  $Sa$  to  $IDR$ , because  $Sa_{h,collapse}$  and the coefficients for the  $Sa$ - $IDR$  transformations for all the model buildings are correlated. Losses for collapsed buildings are taken as the replacement cost for the building. The total loss in each regional loss realization is the sum of the losses for all of the individual buildings.

Simplified methods for modeling probabilistic regional losses, which do not account for  $IDRs$  explicitly, are recommended. Like the High-end method, the proposed simplified methods generate random intensity maps, considering spatial correlations. The first simplified method takes advantage of the observation that losses for non-collapsed buildings estimated with vulnerability functions that take only  $Sa$  as their input variable artificially broadens the regional loss distribution by not conditioning individual building losses on epsilon ( $\epsilon$ ) to account for

spectral shape effects. This artificial broadening of the distribution is approximately equal to the broadening in the distribution that is observed when *IDRs* are explicitly considered. The preferred simplified procedure generates random region-wide  $Sa_{h,collapse}$  for each model building  $h$  from collapse capacity distributions that are conditioned on the average  $\varepsilon$  ( $\varepsilon_{avg,j}$ ) for the earthquake. Another simplified method classifies collapse by generating random realizations of  $Sa_{h,collapse}$  that are independent from site to site and do not take  $\varepsilon$  as an input variable. This second method is less conservative and overestimates large rare losses. However, it lends itself to circumstances in which the analyst desires to implement vulnerability functions that do not depend on  $\varepsilon$  and do not distinguish between collapsed and non-collapsed states explicitly.

We conclude also that only coarse height classifications (*i.e.* each height class represents a range of possible heights) are necessary for modeling a building stock, for the purpose of estimating probabilistic regional loss distributions. It is observed, however, that building capacity (*e.g.* strength and ductility) misclassifications introduce significant errors into the regional loss assessment. Therefore, correctly classifying buildings according to their capacity is a crucial aspect for modeling a regional building stock. Capacity is most often related to the type of structural system and year a building was built. We also show that the details of precise building locations are unimportant for probabilistic regional loss assessment. However, it is important to identify clusters of building concentrations, as in a downtown area, when modeling the regional building stock. Additional findings show that implementing vulnerability functions and replacement costs deterministically rather than probabilistically has negligible impact on the distribution of probabilistic regional losses, if deviations of repair and replacement costs are assumed to be non-systematic. This results because variability of the regional loss is dominated

by sources other than non-systematic variability of repair and replacement costs, *e.g.* variation in ground shaking intensity from each realization to the next.

#### **4.7 Acknowledgments**

This material is based upon work supported by the National Science Foundation under Grant Number 1250163 and the Southern California Earthquake Center (SCEC) (contribution number 1743). SCEC is funded by NSF Cooperative Agreement EAR-0529922 and USGS Cooperative Agreement 07HQAG0008. Any opinions, findings, and conclusions or recommendations expressed in this material are those of the author(s) and do not necessarily reflect the views of the National Science Foundation. We are grateful to Rob Graves for providing the simulated ground motions, Curt Haselton for providing the modern RC frame models, Kevin Kim for conducting some of the PACT analyses, and Jack Baker, Holly Bonstrom, Ross Corotis, and Keith Porter for their helpful insights to the study.

## 5 SUMMARY AND CONCLUSIONS

The essence of performance-based earthquake engineering (PBEE) is to design and analyze structures for specific performance levels rather than prescriptive design requirements. The central goal of such efforts is to enable decision-makers to make risk-informed decisions concerning structures. This thesis applies PBEE methods to problems that can be divided into two categories: (1) seismic design criteria for buildings and (2) regional (portfolio) seismic loss assessment. In the first category, PBEE methods are employed to evaluate a potential change in building seismic standards (*i.e.* altering seismic design requirements for accidental torsion) by assessing the performances of several archetype buildings designed with and without the potential changes. In the second category, regional seismic loss methodologies are developed and evaluated with a special focus on factors that affect the variance of regional seismic loss predictions, because the variance of potential regional losses is key to quantifying risks associated with rare, potentially catastrophic events.

While making recommendations for building design codes and quantifying future regional losses probabilistically are two distinctly different problems, the PBEE methods employed to address them are fundamentally similar. In both cases, building performance is estimated with nonlinear models that are intended to capture important building response properties (*e.g.* ultimate load capacity and post capping negative stiffness). These models are subjected to nonlinear time history analyses. Moreover, uncertainties in ground motion characteristics, building response, and other key parameters, are propagated through the assessment.

As with any study, the mathematical, statistical and physics-based models used in this study (*e.g.* ground motion prediction equations, vulnerability functions, building inventories, building simulation models, *etc.*) are subject to limitations, which should not be ignored when analyzing

the results and making conclusions. One strategy that is taken in these studies for dealing with model limitations is to rely on relative comparisons, rather than absolute performance measures, to reach conclusions. For example, the importance of accidental torsion seismic design requirements is evaluated by comparing the performances of archetype buildings that are designed with and without accidental torsion, rather than on the absolute collapse capacity of the archetype buildings. For evaluating regional seismic loss assessment methods, each candidate method is executed using the same regions, building inventories, ground motion prediction equations (GMPE), building simulation models, *etc.* These relative comparisons are not error-proof, but the impacts of systematic biases in the analyses that are due to model errors/inaccuracies are reduced, because comparisons are made between analyses that are subject to similar sets of limitations. Limitations specific to the models used in each case are discussed in more detail below.

## **5.1 Building Code Development: Accidental Torsion Seismic Design Requirements**

### **5.1.1 Summary and Implications**

The primary goal of examining accidental torsion requirements is to quantify when they are necessary in the seismic design of building structures in order to ensure adequate safety against collapse and, conversely, to determine when such requirements may be safely omitted in the seismic design process. The importance of design provisions for accidental torsion design is evaluated from two viewpoints: the *significance* of the requirements (comparing the collapse capacities of buildings that are designed with and without ASCE/SEI 7 accidental torsion provisions) and the *need* for the requirements (comparing collapse capacities of buildings designed without accidental torsion to those of torsionally-stiff buildings, *i.e.* perimeter frame buildings). The Torsional Irregularity Ratio (*TIR*) is employed to quantify the level of torsional

sensitivity in the building, accounting for both asymmetry and torsional flexibility. The *TIR* is defined in ASCE/SEI 7 as the ratio of the maximum story drift at one end of the structure to the average of the story drifts at the two ends of the structure, where both drifts are computed in the same direction of interest. The drifts for computing the *TIR* include a 5% offset of the line of action for seismic forces (relative to a building's dimensions) in the most critical direction to account for torsional flexibility.

This study finds that the ASCE/SEI 7 accidental torsion design requirements are only *significant* (i.e. affecting collapse capacity by 5% or more) for Seismic Design Category (SDC) B buildings with  $TIR > 1.4$  and for SDC D buildings with  $TIR > 1.2$ . These limits correspond to the definitions of horizontal irregularity Type 1a ( $TIR > 1.2$ ) and Type 1b ( $TIR > 1.4$ ). Therefore, the findings support a proposed modification to the ASCE/SEI 7 Standard whereby the accidental torsion design provisions are only required in SDC B if the building has a Type 1b horizontal irregularity, and are only required in other Seismic Design Categories (SDC C and above) if the building has a Type 1a (or worse) horizontal irregularity. Even a nominally symmetric building may have a Type 1 horizontal irregularity if it is torsionally flexible.

Modern building codes rely on a 5% offset of the center of mass to compute an accidental torsional moment that is used in design. It can be argued that there other methods for handling accidental torsion requirements in building design, and these approaches may better predict actual seismic demands in structures due to accidental torsion. Such a change in approach to designing for accidental torsion could increase the *significance* of accidental torsion in design. Even so, the values of *need* for accidental torsion provisions obtained in this study provide little justification that such an approach is warranted for buildings with low *TIR*.

Comparing the impacts of the accidental torsion design requirements for two Seismic Design Categories, this study finds that the additional requirements in SDC D, namely the torsional amplification factor,  $A_x$ , and drift limits enforced at the building edges, successfully prevent the collapse capacity from degrading as torsional irregularity and flexibility increase. The absence of such requirements in SDC B is the primary reason that accidental torsion design requirements are less significant for SDC B as compared to SDC D buildings with large *TIR*.

Perhaps most importantly, the study of accidental torsion seismic design requirements in this thesis provides an example of how a building code requirement can be examined analytically. In the past, expert judgment has been the primary (or even sole) factor for proposing and evaluating many seismic design requirements. Expert judgment should never be abandoned in the building code development process. However, given the sophistication of modeling tools that are currently available and their continual improvement, future studies of building code requirements may see expert judgment accompanied by analytical studies. The analytical studies are useful for validating, refining, or even modifying building code recommendations that stem from expert judgment. For example, it is easy to expect, based on engineering judgment, that accidental torsion design requirements are relatively insignificant for torsionally stiff buildings, but quantifying the characteristics of buildings for which they become significant is difficult to predict without an analytical study.

### **5.1.2 Limitations**

The study of accidental torsion seismic design requirements was carefully executed so that the limitations influenced the conclusions as little as possible. The processes of designing the archetype buildings, modeling their behavior, and constructing simplified building simulation models were performed systematically. Nonetheless, uncertainties and limitations still remain.

One limitation is that the 3D analytical models used in predicting significance and need for accidental torsion can only approximate building behavior from a global perspective (*i.e.* nonlinearities and deterioration properties are lumped into braces that are calibrated to global behaviors of high-end models). Furthermore, the high-end models to which they are calibrated have several limitations, including nonlinear features that are calibrated from test data for slow (rather than fast, as in an earthquake) cyclic tests and that are lumped into zero-length elements. The collapse capacities of the archetype building models show that their probabilities of collapsing when the ground motion intensity is equal to the maximum considered earthquake ( $MCE_R$ ) intensity defined by ASCE/SEI 7 is 5% to 20%. These collapse probabilities are consistent with the expected collapse safety based on FEMA P-695. Even so, the absolute collapse capacities of the archetype models are not used for making conclusions in this study. Rather, conclusions are based on relative comparisons of performances between similar models so that systematic biases in the models will not adversely affect the conclusions. Additionally, the 3D analytical models have only two frame lines in each orthogonal direction, unlike many real buildings that have several. Having fewer frame lines makes them less redundant and likely more sensitive to torsional effects than buildings with several frame lines. It is expected that this limitation makes the study's conclusions conservative, because accidental torsion design requirements are shown to be more important to torsionally sensitive buildings and the limited number of frame lines makes the archetypes more torsionally sensitive.

Another limitation is that not all possible building types are explicitly represented by the archetype buildings. For example, wood, steel, masonry, and RC shear-wall buildings are not analyzed, and only a finite number of plan aspect ratios, frame layouts, and building heights are considered. However, important properties for building responses to earthquakes, such as

strength, stiffness, ductility, plan configuration, and height are varied systematically in the archetype design space; the variation of these properties spans a relatively broad range so that properties of many real buildings are expected to fall within the range of properties represented by the archetype design space. Therefore, factors that affect buildings' structural properties (*e.g.* structural system type and plan configuration) are represented implicitly, based on the assumption that the important structural properties of such buildings still fall within the range of structural properties represented by the archetype design space. Conclusions are drawn from observations that are consistent across all of the variations of the archetype design space, so it is reasonable to extend these conclusions to many additional structural systems and building types, even if they are not represented explicitly. Exceptions, however, are buildings whose structural properties are not bounded by structural properties represented in the archetype design space. For example, masonry buildings are expected to be less ductile than any of the archetype buildings that are used for this study, so the applicability of the findings in this study to masonry buildings is uncertain. The author hypothesizes that the conclusions of this study can be extended to buildings whose structural properties are not within the bounds of the archetype design space, but further studies are needed to confirm this hypothesis.

### **5.1.3 Future Work**

There is a large potential list of building code seismic provisions, both in new and existing building standards, that may benefit from future analytical examination. The author is currently examining the implications of rigid versus flexible diaphragm assumptions for distributing lateral design loads in buildings that are permitted for the "Simplified Procedure" of the ASCE/SEI 7-10 standard (*i.e.* Section 12.14 of ASCE/SEI 7-10). In the near future, the author would also like to conduct (or see conducted) analytical studies to evaluate seismic design provisions in

ASCE/SEI 7 that pertain to the horizontal and vertical irregularities that are summarized in Table 12.3 of ASCE/SEI 7-10. Analytical studies could help answer the questions: which additional design requirements are truly necessary for buildings with irregularities? At what points do the additional requirements for irregular buildings become necessary? Are the additional requirements for irregular buildings too conservative or not conservative enough? These analyses can help support expert judgment in the building code development process.

## **5.2 Regional (Portfolio) Seismic Loss Assessment**

Probabilistic estimates for regional seismic losses require an analysis framework that considers the variability of the predicted regional losses. This variability stems from both aleatory and epistemic sources, such that it represents both the inherent randomness in future seismic losses as well as our uncertainty in our ability to predict these losses. Past research has demonstrated that spatial correlations of ground motion intensity are important for quantifying regional loss variance. In this thesis, the concept of spatial correlation for regional seismic loss assessments is extended to incorporate spatial correlations of building responses. Based on these findings, advancements to regional seismic loss assessment methods are proposed and tested.

### **5.2.1 Incorporation of Spatial Correlations Between Building Response Parameters in Regional Seismic Loss Assessment: Summary and Implications**

This thesis' examination of spatial correlations between building response parameters shows that correlations in building response are more significant for more similar buildings and closely spaced sites. A critical observation is that spatial correlation patterns between engineering demand parameters (*i.e.* *EDPs*, particularly interstory drift) and spectral accelerations at a building's first-mode period ( $S_a$ ) are similar, when evaluated in natural log space. These findings are based on models of ductile and nonductile reinforced concrete (RC) moment frame buildings

ranging in height from two to eight stories that are evaluated for five different earthquake scenarios for which large numbers of recordings are available.

Building on these observed patterns of spatial correlations, a method for incorporating correlations in building response in regional seismic loss assessment procedures is proposed. In the proposed approach, maps of correlated ground motion intensity measures (*IM*) are generated with preexisting models. These “intensity maps” are used to predict spatial distributions of engineering demand parameters (*EDP*) through linear “*IM-EDP* transformations.” The transformations produce building responses that capture the expected spatial correlation structure of *EDPs*. The distribution of coefficients for defining such transformations is obtained by performing incremental dynamic analysis (IDA) on nonlinear models representing each building type of interest. This addition to regional loss assessment methods represents the first time correlations in building responses, as well as ground motion intensities, are explicitly considered.

## **5.2.2 A Comparative Evaluation Probabilistic Regional Seismic Loss Assessment**

### **Methods, Using Scenario Case Studies: Summary and Implications**

Several different methods for Monte Carlo-based probabilistic regional (portfolio) loss assessment are implemented for case-study building stocks and earthquake scenarios. Findings are based on a stock of ductile and nonductile RC moment frame buildings ranging in height from two to eight stories and two different earthquake scenarios. On the basis of these investigations, it is concluded that important factors to consider in probabilistic regional seismic loss assessments are: (1) spatial correlations of ground motion intensity; (2) regional versus site-to-site methods for collapse classification; (3) accurate characterization of building capacity, especially strength and ductility; and (4) spatial clustering of buildings if such clusters exist in the inventory. Each of these factors significantly impacts the variance of regional loss

predictions. It is also known that demand surge significantly affects the variability of regional seismic losses, although this phenomenon is not examined in the present study.

Based on comparisons to a Benchmark, which estimates building responses via nonlinear dynamic time-history analysis, the regional loss assessment method that converts  $S_a$  intensity maps to maps of  $EDPs$  is found to be more robust than methods that do not consider  $EDPs$  explicitly and is referred to the “High-end” method. Simplified methods for modeling probabilistic regional losses, which do not account for  $EDPs$  explicitly, are also recommended.

### **5.2.3 Sample Regional Seismic Risk Assessment: Summary and Implications**

A regional seismic risk assessment is documented in the appendix to this thesis. For an example geographically-distributed building stock, Monte Carlo simulation (MCS) procedures are employed to: (1) generate fault ruptures; (2) produce suites of ground motion intensity maps (intensity is quantified by  $S_a$ ); (3) reduce the number of intensity maps with  $k$ -means clustering; and (4) compute regional losses. Large magnitude events and high strength intensity maps are preferentially sampled with importance sampling techniques recommended by Jayaram and Baker (2010).

For each intensity map, a regional loss realization is generated by the “Simplified<sub>1</sub>” method that is developed in Chapter 4. Regional seismic loss results for the suite of realizations for an example building stock are presented to illustrate how they can inform decisions at a community (or portfolio) level. The regional losses for the sample building stock are deaggregated multiple ways to show how different portions of the building stock contribute to regional seismic risks. Evaluating seismic risks from a regional perspective, particularly when the risks are deaggregated by structural class, can provide policy makers and risk holders with information that they need to make risk-informed decisions concerning groups of buildings.

#### 5.2.4 Limitations

The key contribution of Chapter 3 is the development of a new method for dealing with correlations in building responses in the context of regional seismic loss analysis. There are several limitations to this study that are worth discussing. First, the author cannot rule out the possibility that the correlation patterns of *EDPs* that are observed in this study are, at least in part, a byproduct of the modeling techniques used to simulate building responses. However, a side-study produced similar results for simulation models for wood frame buildings, exhibiting similar patterns of spatial correlations and cross-correlations of *Sa* and *EDP*. Since these models are fundamentally different than the RC moment frame building simulation models, the similar results provide some confidence that the observed correlation patterns are not just a result of a specific modeling technique or specific to a particular class of buildings. Nonetheless, representing an entire structural class of buildings (*e.g.* modern mid-rise RC moment frames) with a single structural model (*e.g.* the 4-story modern RC frame model used in this study) likely causes a biased over-estimation of correlation, because variability of building structural characteristics (*e.g.* first-mode period, ultimate strength, *etc.*) within the structural class is ignored. The impacts of this potential bias are evaluated and discussed in Section 4.5.4.3, where it is shown that representing all buildings within a structural class with a single model has a negligible impact on the regional seismic loss assessment results, as long as a building inventory is divided into a sufficient number of structural system types and height classifications. The most robust approach to measure correlations of building responses would be to record and analyze the actual seismic responses of several real buildings that are geographically distributed. There are currently not enough data for this approach to be feasible, but this may become possible in the future with more instrumented buildings.

In addition, the method for generating *EDP* maps with *IM-EDP* transformations is based almost exclusively on analyses with ductile and non-ductile RC moment frame models. The aforementioned side-study of wood shear wall buildings showed that the *IM-EDP* transformation approach could also work for these buildings, although other common lateral systems, such as steel moment frames, braced frames, RC shear walls, and masonry, are not examined. Since the method for generating *EDP* maps with *IM-EDP* transformations works for two distinctly different building types, the author expects that it will work for the additional building types as well, although this hypothesis is not explicitly tested.

In the evaluation of regional seismic loss assessment methods in Chapter 4, the regional loss methodologies do not directly account for soil liquefaction and soil-structure interaction effects, which may significantly impact regional losses. For regions with liquefiable soils, a robust analysis should consider the possibility of liquefaction – a method for doing so is beyond the scope of this study, but is likely to improve regional seismic loss assessments by accounting for collapse cases and large repair costs that can result from soil liquefaction. Liquefaction can cause foundation failures and ground settlements, as well as tilting (Ambraseys and Sarma 1969). Soil-structure interaction has important impacts on the response of stiff structures that are located on relatively soft soils (ATC 2012). The degree to which soil-structure interaction impacts regional losses is unknown, but it could be tested a number of ways. One possibility is to develop distributions of *IM-EDP* transformations that depend on soil conditions. These *IM-EDP* transformations could be developed by analyzing the same models, but with varying foundation fixities to represent different soil conditions. Since the *IM-EDP* transformations are also specific to a class of buildings, such a method would account for the differences in soil-structure interaction on buildings with different periods.

Furthermore, a number of ground motion intensity measures other than  $Sa$  could have been considered, such as peak ground acceleration ( $PGA$ ) or arias intensity. However,  $Sa$  at a building's first-mode period is significant, because spatial correlations are shown to be sensitive to building period. Inelastic spectral displacement ( $Sd_i$ ), which also accounts for building period, may be a good  $IM$  for producing  $EDP$  maps through  $IM-EDP$  transformations as well. Since  $Sd_i$  is based on building capacity and represents a nonlinear response, an  $Sd_i$  map may be a suitable substitute for an  $EDP$  map and, indeed, eliminate the need for an  $IM-EDP$  transformation.  $Sd_i$  is not used in this study, because current GMPEs for producing  $Sd_i$  intensity maps are limited in comparison to those for  $Sa$ . Since unbiased  $EDP$  maps can be predicted from  $Sa$  maps, the prospect of an  $IM$  that is more difficult to compute than  $Sa$  is not investigated. However,  $Sd_i$  still may provide more precise results than  $Sa$  and could be the topic of future studies. On the other end of the spectrum, if an  $IM-EDP$  transformation is required, it may be possible in some cases to use a simpler  $IM$ , like  $PGA$ , for this purpose. This change would produce somewhat larger uncertainty in the  $IM-EDP$  transformation.

The sensitivity of regional seismic loss assessments to limitations in building stock classifications and vulnerability functions is also assessed. One limitation in regional loss assessments is that not every building can be represented by a model building that characterizes it specifically – nor is it often feasible to confidently describe a building stock in such great detail in the first place. Instead, buildings are categorized and the represented by model buildings to which they are most similar (*i.e.* a 5-story building falls into the “mid-rise” category and is represented by a 4-story model). The study finds that only coarse height classifications (*i.e.* each height class represents a range of possible heights) are necessary for modeling a building stock, for the purpose of estimating probabilistic regional loss distributions. Discretization of building

heights into several small categories is not expected to significantly impact the probabilistic regional loss distribution. Furthermore, height misclassifications do not significantly impact regional loss distribution predictions because, for the RC frames examined, capacity is not strongly correlated with height; however, height misclassifications are expected to affect regional loss distributions if building height and building capacity are closely related.

It is observed, however, that building capacity misclassifications introduce significant errors into the regional loss assessment. Therefore, correctly classifying buildings according to their capacity is a crucial aspect for modeling a regional building stock. Capacity is often related to the type of structural system and the building code era in which a building was built. Several other factors, such as quality of design, materials, and craftsmanship influence capacity as well. Many of these factors are difficult to quantify.

Another limitation of regional seismic loss assessments is that determining building locations is often difficult. However, the details of precise building locations are found to be relatively unimportant for probabilistic regional loss assessments. Nevertheless, it is important to identify clusters of building concentrations, as in a downtown area, when modeling the regional building stock. Clustering of buildings is expected to be particularly important for regions that have high spatial variability of soil properties.

Some vulnerability functions output only expected loss values, but not their standard deviations (HAZUS vulnerability functions, for example). An additional study tests the impact of using deterministic vulnerability functions rather than probabilistic vulnerability functions. Implementing vulnerability functions (and replacement costs) deterministically rather than probabilistically has negligible impact on the distribution of probabilistic regional losses, if deviations of repair and replacement costs are assumed to be non-systematic. In essence, this

finding shows that regional loss is dominated by sources other than non-systematic variability of repair and replacement costs, *e.g.* variation in ground shaking intensity from each realization to the next. However, systematic variations of repair and replacement costs, such as demand surge, are still expected to significantly impact regional loss variability.

The conclusions that are made about regional loss assessment methods are all based on relative comparisons – not absolute loss predictions, because the regional losses that are computed in this study, even for the benchmark, may be affected by systematic biases. Potential sources of bias include systematic errors in soil classification, GMPE predictions, building simulation models, vulnerability functions, and building inventory data. For example, the vulnerability functions are created by analyzing building simulation models that may not accurately represent the buildings that are actually present in the real building stock, and are based on assumed quantities and types of building components that may not reflect the true components of the buildings. Therefore, the actual dollar values of regional losses reported in this study should not be interpreted as the real values that would occur in the scenario events. However, the relative comparisons of assessments of identical building inventories, using the same soil classifications and GMPEs, and employing vulnerability functions that are created from the same models and data sets, are considered to be reliable. These comparisons are reliable because the main sources of error (for example, misestimating the quantities and costs of building components when creating vulnerability functions) are equally present in all of the analysis methods, so comparisons between methods are relatively insensitive to those errors.

Nevertheless, there are still limitations concerning relative comparisons between regional loss estimations that deserve mentioning. For one, the simplified regional loss assessment procedures that are recommended by these studies are shown to be “right for the wrong reason,”

because the additional variance of regional loss due to using a simple intensity measure,  $S_a$ , is approximately equal to the additional variance of regional loss that is observed when spatial correlations of  $IDR$  are explicitly considered. While the author finds no reason to expect a different result for other building types that are not considered in this study, it is uncertain whether this same observation would be made for other structural types (ordinary braced frames, for example) and/or with different modeling techniques. Additional analytical studies with different building simulation models or, better yet, recorded data from building instruments in several real and spatially-distributed buildings subjected to earthquakes could confirm (or refute) the validity of the proposed regional loss assessment methods.

In addition, the finding that collapse capacity is defined better on a region-wide basis for each structural class of buildings than on a site-to-site basis may not hold true for all building types. The reason that region-wide collapse capacities work better than site-to-site collapse capacities in these studies is because collapse capacity is sensitive to ground motion spectral shape. Since there exists inter-event variability of ground motion spectral shape, there is also inter-event variation of collapse capacity, which is not captured when collapse capacity is determined independently from each site to the next. If a building's collapse capacity is insensitive to spectral shape, then it is unlikely that region-wide collapse capacity determinations will have any advantage over site-to-site collapse capacity determinations. Region-wide collapse capacity determinations could also account for additional factors that are not reflected by  $S_a$  (such as arias intensity and duration), but cause inter-event variation in collapse performance; these are not explored in this study, but could be topics of future work.

### **5.2.5 Future Work**

The regional seismic loss assessment procedures that are recommended in this thesis and demonstrated in the appendix have several useful applications. However, it is unlikely that many of the parties interested in applying them will have the tools, resources, and skills to execute them. Packaging the regional loss assessment tools into user-friendly software may be an effective way to make them available to more people. A probabilistic regional seismic loss software application could be added as an additional layer to existing software such as PACT (FEMA 2012) or HAZUS (FEMA 2003), or possibly as its own stand-alone application.

In the future, it may also be possible to adapt a regional seismic loss assessment procedure to create community fragility or vulnerability functions. Such a function could be convolved with regional magnitude-recurrence information or with the hazard for a representative site to obtain seismic risks for communities of buildings.

## **6 Appendix: Documentation of Regional (Portfolio) Seismic Risk Analysis**

### **6.1 Overview**

This chapter documents the implementation and use of a regional seismic risk assessment software application, using an example region and building inventory. The tool uses Monte Carlo Simulation (MCS) techniques. The output is a suite of regional loss realizations, each of which having an expected frequency of occurrence, that describe the regional seismic risks. The methodology for computing regional seismic losses that is implemented in this section is referred to as “Simplified<sub>1</sub>” in Chapter 4 of this thesis.

### **6.2 Application Software and Organization**

The regional seismic risk assessment tool is a MATLAB application, consisting of two scripts and a couple dozen functions. It requires the user to define a region and building stock beforehand. For the user-defined region, it generates a suite of fault rupture scenarios (*i.e.* magnitudes and rupture locations), based on a database of active faults and their properties and the expected regional seismicity. Following this, random fields of ground motion intensities are sampled for every fault rupture scenario. The random fields of ground motion intensity (“intensity maps”) are sampled from probability distributions of ground motion intensity that are obtained with a ground motion prediction equation (GMPE). Spatial correlations of ground motion intensity are considered in the generation of intensity maps. The total number of intensity maps for representing the regional hazard is reduced with importance sampling techniques and by *k*-means cluster analysis, following recommendations from Jayaram and Baker (2010). For each intensity map, a regional loss realization is generated. Regional loss results from all of the MCS realizations are compiled to quantify the regional seismic risks. These steps are executed

with two scripts: the first script completes the steps required to obtain the suite of intensity maps; the second script computes the regional losses for each intensity map and compiles the results.

### 6.3 Define a Region and Building Stock

The regional seismic loss assessment procedure that this chapter documents assumes that a building stock has been defined. For example purposes, a 36 square mile test region in the Los Angeles and South Los Angeles area (Figure 6.1) of southern California is considered throughout this chapter. A portfolio of reinforced concrete (RC) moment frames is considered, which has the same building classifications and number of buildings per area as the ‘low density’ building stocks developed by DeBock et al. 2013 (Chapter 4).

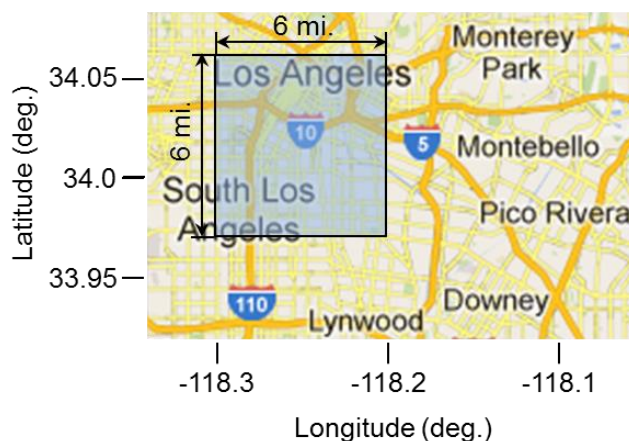


**Figure 6.1** Test region location for the building stock (inventory) example that is considered throughout this chapter.

The test region has 145 buildings, shown graphically in Figure 6.2. Each building’s occupancy is classified as either commercial, residential, or hospitality, and its structural characteristics (*i.e.* fundamental period, capacity, etc.) are represented by one of six nonlinear multi-degree-of-freedom model buildings that is most similar to the building of interest. The model buildings, each representing a structural class, are summarized in Table 2.1. The structural classes include ductile and non-ductile buildings and range in height from 2 to 8 stories. Ductile

model buildings are taken from Haselton *et al.* (2011) and nonductile model buildings are taken from Liel *et al.* (2011).

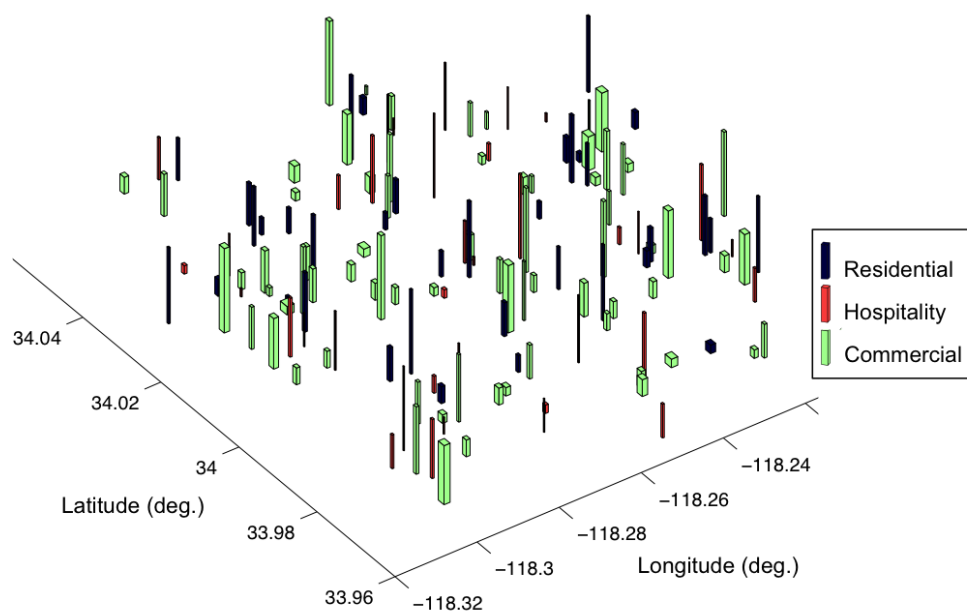


**Figure 6.2** Map of building locations for the building stock that is analyzed in this example. Building sizes are represented graphically, but differences in size are exaggerated.

**Table 6.1** Summary of Model Buildings Representing Each Structural Class.

Structural Class	Model Bldg. Description	No. of Stories	First-Mode Period ( $T_1$ ) (s)*	Ductility Capacity <sup>†</sup>
1	Low-rise, new (Ductile)	2	0.60	15.0
2	Mid-rise, new (Ductile)	4	0.91	10.7
3	High-rise, new (Ductile)	8	1.81	6.0
4	Low-rise, old (Nonductile)	2	1.03	3.3
5	Mid-rise, old (Nonductile)	4	1.92	2.3
6	High-rise, old (Nonductile)	8	2.23	2.3

\* Determined from eigenvalue analysis assuming cracked concrete sections of about 35% of the gross properties, depending on axial load. As a result, these periods are longer than those that have been measured in moderate shaking events (Goel and Chopra 1997).

<sup>†</sup> Determined by nonlinear static pushover analysis as described in FEMA (2009). There are many methods for computing ductility, so these values are provided for the purpose of comparing deformation capacity of the model buildings.

## **6.4 Generating Fault Rupture Scenarios**

The first step in the MCS process for regional seismic loss assessment is to generate a suite of fault rupture scenarios. This process requires the identification and characterization of faults in and near the region of interest. This section describes the method by which faults are identified and characterized. The fault characterization is used to generate random fault rupture scenarios that are probabilistically consistent with regional seismicity.

### **6.4.1 Fault Properties**

For the Southern California example region, active faults and their properties are obtained from a database of California faults that is publically available from the California Geological Survey (CGS 2013). The database provides information such as start and end coordinates, slip rate, maximum magnitude, and fault type for the documented faults in California. Potential faults are considered within a 200 km radius of the region of interest. Figure 6.3 shows all of the active faults that are located within 200 km of the test region.

### **6.4.2 Sampling Earthquakes for Each Fault**

After identifying faults in the region, suites of earthquakes are sampled from each fault by generating random magnitudes and rupture locations. The frequency density of earthquake magnitudes is defined for each active fault using the characteristic magnitude-recurrence relationship of Youngs and Coppersmith (1985). The characteristic magnitude-recurrence model assumes a uniform recurrence rate for the characteristic magnitude range and an exponential recurrence relationship for all other magnitudes. The fault input data for the Youngs and Coppersmith magnitude-recurrence model is obtained from the California Geological Survey (CGS 2013). Figure 6.4 shows the earthquake frequency density as a function of magnitude for an example fault; frequency is measured in events per year. Note that the area under the

frequency density function in Figure 6.4 is not one, but rather is equal to the annual frequency of any earthquake of magnitude  $m \geq 5.0$  occurring on that fault. Following Jayaram and Baker (2010), only magnitude 5.0 earthquakes and greater are considered, since smaller earthquakes are not expected to result in significant damage or loss to buildings. For each sampled earthquake, the length of the fault rupture is estimated with empirical relationships developed by Wells and Coppersmith (1994), and its location is designated to a randomly selected portion of the fault.

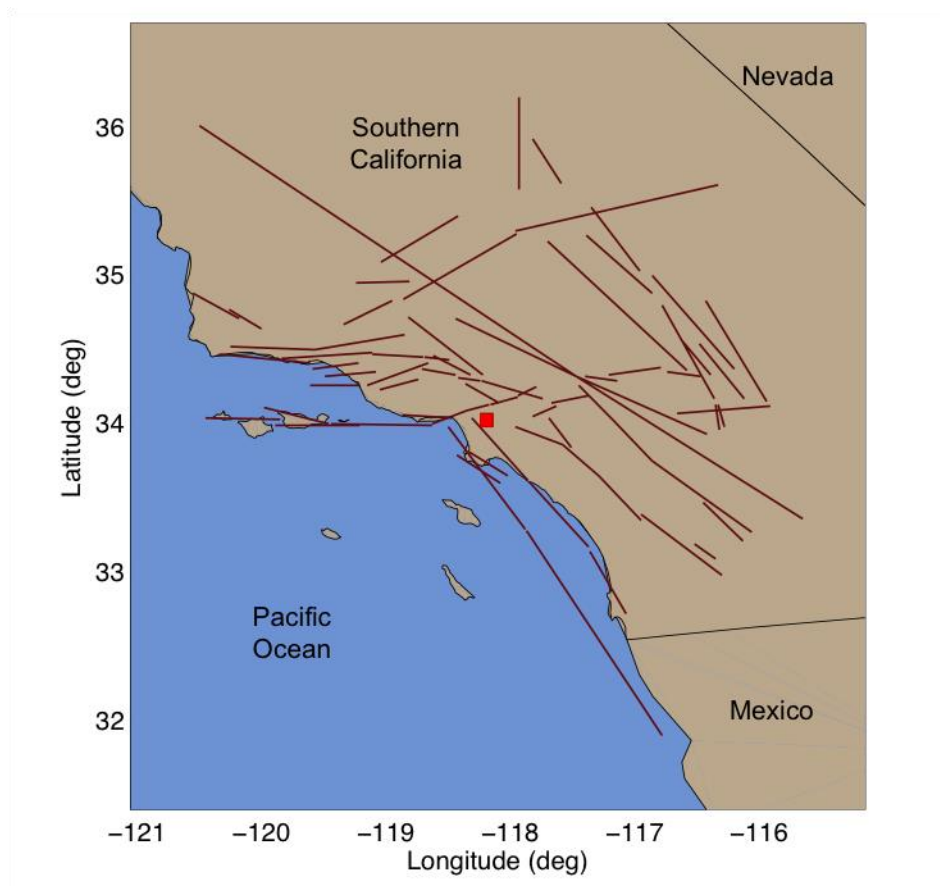


**Figure 6.3** Map showing region of interest (red rectangle) and all documented faults within a 200 km (124 mile) radius in Southern California.

It is desirable to sample earthquakes covering the full range of possible magnitudes. However, since small earthquakes occur with greater frequency than large earthquakes, a traditional MCS approach would sample several small earthquakes and few large earthquakes.

Jayaram and Baker (2010) recommend sampling earthquake magnitudes from a partitioned distribution, as in Figure 6.4, in order to ensure that sampled earthquakes span the full range of possible magnitudes without generating an excessive number of small magnitude events. The same number of earthquakes is sampled from each partition of the magnitude frequency distribution for each fault. In this scheme, large magnitude events are preferentially sampled by creating more partitions at larger magnitudes (*i.e.* narrower partition widths).

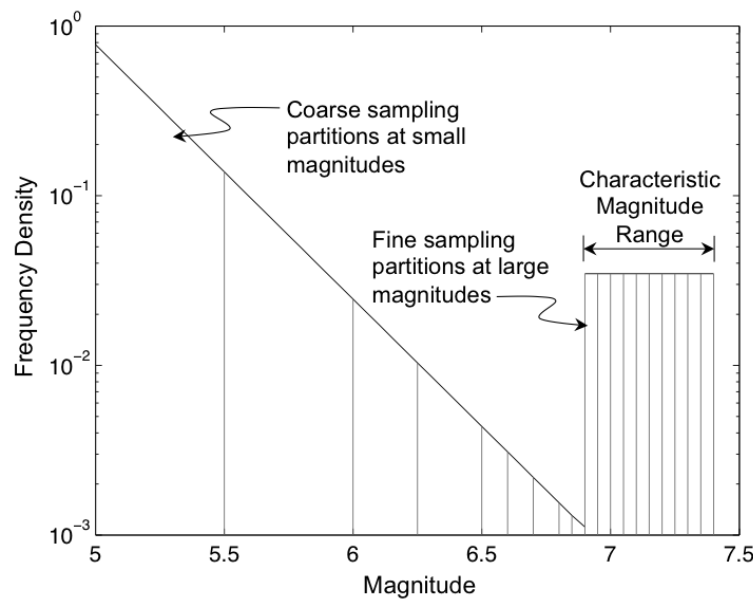


**Figure 6.4** Frequency density function for earthquake magnitudes on a selected fault. Partitions are constructed to preferentially sample large magnitudes.

In this example, one earthquake is sampled from each partition and partition widths are 0.5 for  $5.0 \leq m < 6.0$ , 0.25 for  $6.0 \leq m < 6.5$ , 0.1 for  $6.5 \leq m < 6.8$ , and 0.05 for  $m \geq 6.8$ , as shown in Figure 6.4. A total of approximately 800 fault ruptures are sampled for the entire region. Since the partitioned sampling technique is biased toward sampling large earthquakes, each sampled earthquake is assigned an importance sampling (*IS*) weight, denoted  $IS_m$ .  $IS_m$  is the annual frequency of an earthquake from a given partition occurring and is equal to the area beneath the magnitude frequency density function for the partition interval. For an explanation of the theory

behind importance sampling techniques for *MCS* from a regional seismic loss analysis perspective, the reader is referred to Jayaram and Baker (2010).

### 6.4.3 Matching the 2009 USGS Regional Magnitude-Recurrence

The regional magnitude-recurrence relationship is defined by the Mean Rate of Exceedance (MRE) per year, *i.e.* the frequency at which a given magnitude is expected to be exceeded, and is referred to as an MRE curve. The MRE of a given magnitude  $m$  for the sampled earthquakes can be computed with Equation 6.1

$$MRE_m = \sum_{l=1}^n IS_{m,l} * I_{m_l > m} \quad 6.1$$

where  $MRE_m$  is the *MRE* for magnitude  $m$ ,  $n$  is the number of earthquake realizations that are generated for the whole region,  $IS_{m,l}$  is  $IS_m$  for earthquake  $l$ , and  $I_{m_l > m}$  is a Boolean indicator that is one if the magnitude of earthquake  $l$  is greater than  $m$  and 0 otherwise.

Generating random fault ruptures on a fault-by-fault basis is not guaranteed to produce an unbiased regional magnitude-recurrence relationship due to a number of limitations, including not directly accounting for multi-segment fault ruptures or background seismicity. To correct these errors, the sampling procedure that is described in the previous section is modified to produce a target regional magnitude-recurrence relationship. The target regional magnitude-recurrence relationship is obtained with the Earthquake Probability Mapping tool, which is publically available from the United States Geological Survey (USGS 2009).

The magnitude sampling procedure is adjusted in two steps. In step 1, the maximum magnitude for each fault is increased by 0.2. As a result, the characteristic magnitude is increased and the frequency with which small magnitude events occur is decreased. The motivation for this step is to indirectly account for multi-segment fault rupture possibilities; the adjustment factor of 0.2 is based on the author's judgment. A regional magnitude-recurrence relationship, resulting

from the sampled earthquake magnitudes with only the step 1 adjustment, is shown in Figure 6.5 (see the line labeled, “Sampled Magnitudes”).

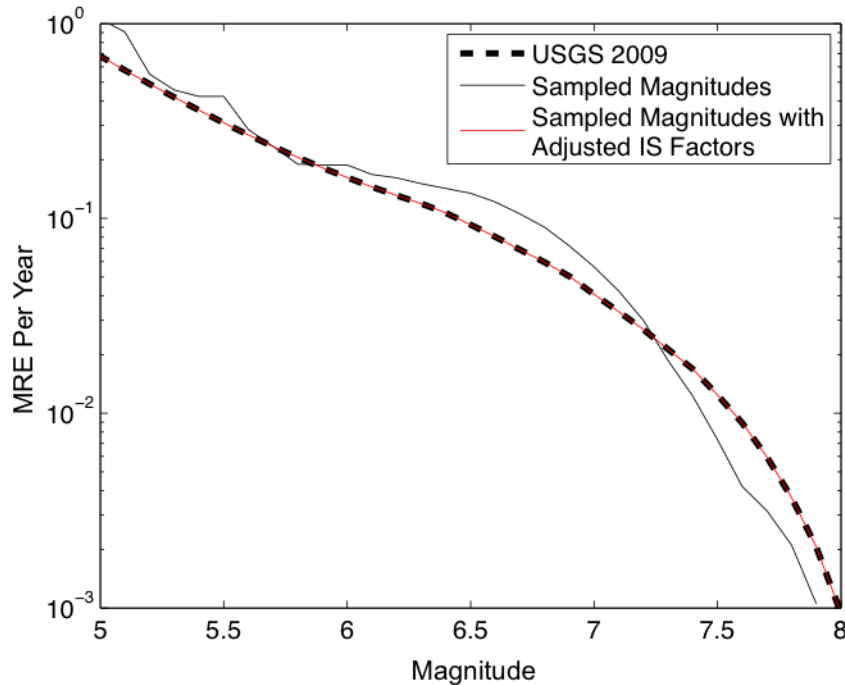


**Figure 6.5** Magnitude-recurrence relationship for the test region, considering only fault ruptures within 200 km (124 miles). Consider adding the other curve for the thesis.

Step 2 omits fault ruptures that are not located within 200 km of the region and adjusts the  $IS_m$  weights for the remaining earthquake events such that they produce a regional magnitude-recurrence relationship that matches the target. The process for adjusting the  $IS_m$  weights to achieve a target MRE curve is systematic, starting with a large magnitude and working downward in increments of magnitude ( $\Delta_m$ ). For the first increment, the target MRE is matched by uniformly scaling all of the  $IS_m$  weights for earthquakes with magnitudes greater than the starting magnitude  $m$  such that their sum is equal to  $MRE_m$  from the target magnitude recurrence relationship. For each subsequent increment, the  $IS_m$  weights for all earthquakes within the increment are uniformly scaled so that  $MRE_m$  matches the target. This implies that all  $IS_m$  weights for earthquakes in the magnitude increment range are uniformly increased or decreased

so that the magnitude frequency density for that range is consistent with the target. A constant increment of  $\Delta_m=0.1$  is used for modifying the approximately 800  $IS_m$  values in this example, but a larger increment size may be desirable for analyses with fewer fault ruptures. The MRE curve for earthquake magnitudes that is computed with the adjusted  $IS_m$  weights is plotted in Figure 6.5; by design, it matches the target MRE curve from the 2009 USGS Earthquake Probability Mapping tool.

#### 6.4.4 An Alternative Approach for Generating Random Fault Rupture Scenarios

Jayaram and Baker (2010) generate fault rupture scenarios by an alternative method that is mathematically equivalent to the method described in Sections 6.4.2 and 6.4.3. Rather than sample earthquakes from each individual fault, they sample earthquake magnitudes from a regional magnitude recurrence relationship (*e.g.* the target MRE curve obtained from the 2009 USGS earthquake probability mapping tool) and use a regional magnitude probability distribution to compute  $IS_m$  weights. After sampling an earthquake, magnitude is either: (1) randomly assigned to an individual fault, where the probability of assigning it to any fault is proportional to the likelihood of a magnitude of its size occurring on that fault; (2) assigned to each fault in the region. For case 2, where the sampled magnitude is assigned to every fault in the region, the  $IS_m$  weight for each fault  $i$ ,  $IS_{m,l}$ , is the product of  $IS_m$  for the region,  $IS_{m,region}$ , and the probability that a given earthquake of magnitude  $m$  occurs on fault  $l$ :

$$IS_{m,l} = IS_m * P(\text{Fault } l \mid m) \quad 6.2$$

### 6.5 Generating Ground Motion Intensity Maps

Once a suite of fault ruptures is obtained, a group of ground motion intensity maps is generated for each fault rupture, again using importance sampling techniques that are based on Jayaram and Baker (2010). Following the ‘‘Simplified<sub>1</sub>’’ method proposed in Chapter 4, this

example uses spectral acceleration at a building's first-mode period,  $Sa(T_1)$ , as the ground motion intensity measure, which is hereafter abbreviated as  $Sa$ . Generating the ground motion intensity maps is completed by: (1) computing the expected values and standard deviations of  $Sa$  for each site and for each building period with a GMPE; (2) generating random realizations of residual terms, which are added to the expected  $Sa$  values to compute intensity map realizations.

### 6.5.1 Compute Expected $Sa$ at Each Site from a GMPE

For each fault rupture, expected  $Sa$  values corresponding to each of the building periods are computed with the 2008 Boore and Atkinson GMPE. This GMPE is selected because it was developed with ground motions that are relevant for the Southern California tectonic environment and because the input parameters that it requires, *i.e.* magnitude, distance, period, fault type, and average shear wave velocity in the top 30 meters of site soil ( $V_{s30}$ ), are readily obtainable from the previous steps of the regional loss assessment. The GMPE predicts the natural log of  $Sa$  and its standard deviation, which can be deaggregated into inter-event and intra-event components. Accordingly,  $Sa$  for a site  $i$  and event  $j$  ( $Sa_{ij}$ ) can be represented by Equation 6.3, where  $\sigma_{ij}$  and  $\tau_j$  are intra-event and inter-event standard deviations, respectively. The intra-event and inter-event residual terms,  $\epsilon_{ij}$  and  $\eta_j$ , are both normally distributed with a mean of zero and standard deviation of one. Intra-event residuals vary from site to site (*i.e.* within the event), whereas inter-event residuals are constant across all sites (for a given period), and only vary from one event to the next (and from period to period).

$$\ln(Sa_{ij}) = \ln(\widehat{Sa}_{ij}) + \sigma_{ij}\epsilon_{ij} + \tau_j\eta_j \quad 6.3$$

The total residual,  $\varepsilon$ , is the difference between  $Sa$  and the expected value of  $Sa$  from the GMPE, normalized by the total standard deviation of the GMPE. Referring to Equation 6.3,  $\varepsilon$  for site  $i$  and ground shaking intensity map  $j$  is can be written as:

$$\varepsilon_{ij} = \frac{\sigma_{ij}\epsilon_{ij} + \tau_j\eta_j}{\sqrt{\sigma_{ij}^2 + \tau_j^2}} \quad 6.4$$

### 6.5.2 Generate Residuals and Build the Intensity Maps

Intensity maps are created by generating random realizations of inter-event and intra-event residuals and adding these residuals to the expected *Sa* values at each site through Equation 6.3. Several researchers have shown that intra-event residuals are spatially correlated (*e.g.* Wesson and Perkins 2001), indicating that sites in close proximity to one another are likely to have similar intra-event residuals. Inter-event residuals for different periods are also positively correlated, having higher correlations at similar periods and lower correlations at dissimilar periods (*e.g.* Baker and Cornell 2006).

In order to capture spatial correlations of intra-event residuals in the MCS analysis, random fields of intra-event residuals are generated from a multivariate distribution whose covariance matrix describes the site-to-site correlations of intra-event residuals. For this example, covariance between sites is computed with the Loth and Baker (2013) spatial correlation model. This model is developed for computing spatial correlations of intra-event residuals for the same period, as well as cross-correlations of intra-event residuals for different periods, which is necessary for this example. Figure 6.6 shows the spatial correlation of intra-event residuals as a function of distance for a period of 1.0 seconds, computed by the Loth and Baker (2013) model. Notice in Figure 6.6 that the inter-event residual term, which is constant at all sites for a given period and earthquake, is perfectly correlated, and that the correlation of the total residual is between the intra-event correlation and 1.0.

A traditional MCS approach would generate a large number of random fields of intra-event residuals in order to sufficiently capture their range of possibilities. Jayaram and Baker (2010)

demonstrate that the number of random fields of intra-event residuals that is sufficient for capturing the variance of regional losses can be reduced by preferentially sampling fields with large positive residuals. This preferential sampling can be accomplished by shifting the mean of the distribution of site intra-event residuals from a joint distribution with a mean of 0.0 to a joint distribution with mean of 1.0<sup>13</sup>. This shift is accounted for by computing importance sampling weights for each of the fields of intra-event residuals,  $IS_{\epsilon}$ , calculated with Equation 6.5:

$$IS_{\epsilon} = \exp\left(\frac{1}{2}(\epsilon - ms)' * COV^{-1} * (\epsilon - ms) - \frac{1}{2}\epsilon' * COV^{-1} * \epsilon\right) \quad 6.5$$

In Equation 6.5 (from Jayaram and Baker (2010)),  $\epsilon$  is the vector of the intra-event residuals for a given realization,  $ms$ , is the mean shift ( $ms=1.0$  in for this example application) and  $COV$  is the covariance matrix for the multivariate distribution of intra-event residuals. With this importance sampling method, recommendations from Jayaram and Baker (2010) indicate that  $r=50$  random fields of intra-event residuals for each of the fault rupture scenarios (*i.e.* 50 intensity maps per scenario) is sufficient.

Inter-event residuals are generated in a manner similar to that by which the intra-event residuals are generated. Six inter-event residuals are generated for each intensity map realization, corresponding to the periods of the six structural classes that represent the building stock. Inter-event residuals are sampled from a joint distribution that reflects the separation of building periods. The covariance matrix of the joint distribution is calculated from the relationship developed by Baker and Cornell (2006) that quantifies period-to-period correlations of residuals. As described above, regional loss assessment can be done more efficiently if these residuals are preferentially sampled for the larger values. Therefore, the mean of the distribution of inter-

---

<sup>13</sup> Jayaram and Baker (2010) recommend values by which to shift the mean that depend of the size of a region and the number of sites.

event residuals is shifted from zero to  $0.8^{14}$ , and importance sampling weights for inter-event residuals,  $IS_{\eta}$ , are computed by an equation similar Equation 6.5. For a given intensity map, the same inter-event residual values are repeated at all of the sites; a new set of inter-event residuals is generated for each intensity map.

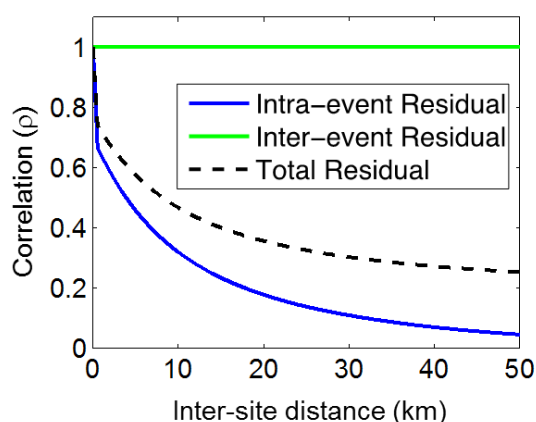


**Figure 6.6** Correlation of residuals as a function of distance for  $Sa(T_1=1.0 \text{ sec})$ , computed with the Loth and Baker (2013) spatial correlation model.

### 6.5.3 Summary and Validation of Resulting Intensity Maps

For each of the approximately 800 fault rupture realizations,  $r = 50$  realizations of residuals are combined with the expected values and standard deviations from the GMPE, using Equation 6.3, to produce  $r = 50$  intensity maps per fault rupture. Therefore, the total number of maps is approximately  $800 \times 50 = 40,000$ .

The procedure for generating the suite of intensity maps is validated through a site hazard analysis. To conduct the validation, the hazard at a site within the region is computed from the MCS intensity maps and then compared to results of a site hazard analysis that is conducted with OpenSHA (2013). To make the comparison, a new suite of intensity maps is generated for

---

<sup>14</sup> Jayaram and Baker (2010) recommend a mean shift ( $ms$ ) of the inter-event residual distribution of  $0.5 \leq ms \leq 1.0$ .

periods of 0.5, 1.0, and 2.0 seconds, and matching the target 2002 USGS magnitude recurrence relationship, such that predictions are directly comparable to OpenSHA. Site hazard MRE values can be computed from the suite of intensity maps by applying Equation 6.6 to  $S_a$  at the site of interest.

$$MRE_{S_a>h} = \sum_{l=1}^n \left\{ IS_{m,l} * \frac{1}{r} * \sum_{j=1+l*r}^{r+l*r} IS_{\epsilon,j} * IS_{\eta,j} * I_{S_a>h} \right\} \quad 6.6$$

In Equation 6.6,  $MRE_{S_a>h}$  is the mean annual rate at which  $S_a$  for the site of interest is expected to exceed a value  $h$ .  $n$  is the number of fault ruptures and  $r$  is the number of intensity maps that are generated for each fault rupture.  $IS_{m,l}$  is the importance sampling weight for fault rupture  $l$  with magnitude  $m$ .  $IS_{\epsilon,j}$  and  $IS_{\eta,j}$  are the importance sampling weights for the intra-event and inter-event residuals, corresponding to map  $j$ .  $I_{S_a>h}$  is a Boolean indicator that is one if  $S_a>h$  and zero otherwise.

The site hazard comparison is shown in Figure 6.7. The suite of approximately 40,000 maps produced by the MCS procedure produces site hazard that is very similar to OpenSHA results. A random site was selected for this comparison, so it is reasonable to assume that similar results (*i.e.* the hazard calculated from MCS being similar to the hazard calculated from OpenSHA) would also be observed at other sites.

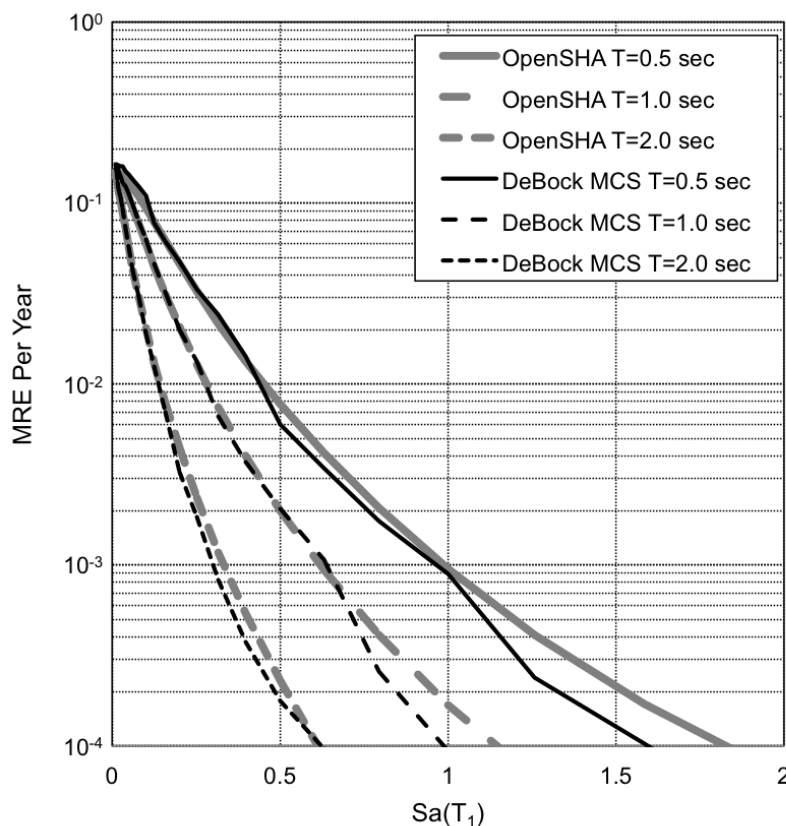


**Figure 6.7** Comparison of site hazard with OpenSHA (2013) and the MCS analysis. For this example, the magnitude recurrence is adjusted to match the 2002 USGS mag recurrence, since the 2009 USGS model is not available in OpenSHA.

## 6.6 K-means Clustering of Intensity Maps

Even with importance sampling, the number of ground motion intensity maps that are generated by MCS is excessively large ( $\approx 40,000$ ), making it desirable to further reduce the number of intensity maps for which regional loss computations are performed. One approach could be to increase partition widths for sampling earthquake magnitudes and/or decrease the number of intensity maps that are generated for each fault rupture. However, this approach runs the risk of underrepresenting large rare events. Jayaram and Baker (2010) propose the use of  $k$ -means clustering techniques (McQueen 1967) to select a subset of intensity maps that are representative of the entire suite of maps. This method groups similar maps into clusters, and one

map is selected from each cluster to represent all of the maps in its cluster. Their approach can significantly reduce the number of intensity maps for which regional losses are calculated, while still representing a full range of regional ground shaking intensities. This section describes how  $k$ -means clustering is performed and how it is applied to select representative maps for regional loss assessment.

### 6.6.1 General Description of $k$ -means Clustering

$k$ -means clustering assembles data into  $k$  clusters, such that the variance of the clustered data is minimized. The variance of a cluster is typically measured by the sum of the squares of the Euclidian distances of the data to the cluster's centroid. The total variance of the clustered data is the sum of the variances from each of the clusters.  $k$ -means clustering is performed iteratively. The first step is to randomly pick  $k$  cluster centroids and assign all of the data to the closest centroids. Then, the centroids are recomputed for each cluster and the data are reassigned to the closest new centroid locations. This process is repeated until no more reassignments occur. Figure 6.8a shows an example data set, wherein each datum  $i$  is a vector quantity of two components,  $X_i$  and  $Y_i$ . In Figure 6.8b, the data is clustered into  $k=3$  clusters with the circle, triangle, and square markers indicating which data are assigned to each of the three clusters.

### 6.6.2 Clustering Intensity Maps

$k$ -means clustering is applied to the suite of intensity maps that is generated by MCS. Jayaram and Baker (2010) produce a total of 150 clusters to represent the regional seismic hazard. This example groups intensity maps into approximately 1,300 clusters. This example uses more clusters than Jayaram and Baker (2010) for two reasons. The first reason is that the procedure for computing losses in this example depends on the total  $S_a$  at each site and also accounts for the level of contribution from inter-event residuals, whereas Jayaram and Baker

computed losses only from the total  $Sa$  at each site. Therefore, if 150 clusters are necessary to represent the possible distributions of  $Sa$ , then each of those clusters should be further divided into sub-clusters of maps whose inter-event residual values are similar, resulting in several more clusters. The second reason for using more clusters is that the number of representative intensity maps for which regional losses are computed does not significantly affect the computation time unless over 1,500 maps are used, although this number will vary from one computer to the next.

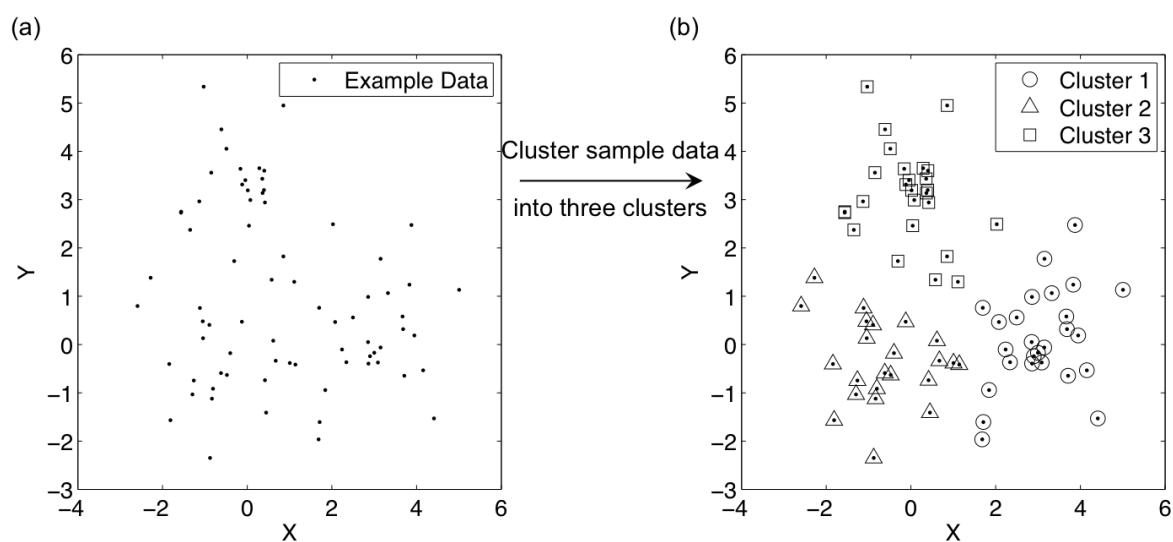


**Figure 6.8** k-means clustering example. Random data pairs  $(X_i, Y_i)$  (a) are grouped into three clusters (b).

Clustering is performed in stages for computational efficiency. Jayaram and Baker (2010) performed clustering in two stages. Stage 1 clustered intensity maps into  $k_1$  clusters, based on the sum of the intensities of all the sites in the region. For illustration, this is analogous to clustering the data in Figure 6.8 based on a data set  $Z$ , where  $Z_i = X_i + Y_i$ . Since the data to be clustered in stage 1 is scalar rather than vector quantities, the first stage of the cluster analysis computes rather quickly. For each of the  $k_1$  clusters, stage 2 of their analysis groups the intensity maps into  $k_2$  clusters, based on data vectors containing  $Sa$  values for every site in the region. Jayaram and Baker used  $k_1=50$  and  $k_2=3$  to obtain  $K = k_1 \times k_2 = 150$  clusters.

In this example, intensity maps are clustered in 3 stages. Stage 1 is similar to Jayaram and Baker (2010); intensity maps are grouped into  $k_1$  clusters, based on the sum of intensities for the entire region. To deal with a building stock characterized by multiple structural classes, it is necessary here to consider  $S_a$  at multiple periods. Since  $S_a$  at short periods tends to be larger than  $S_a$  at long periods, a straightforward cluster analysis is dominated by short-period  $S_a$  values. To make the cluster analysis unbiased with respect to period, a normalized set of intensity maps is created for the purpose of clustering. The normalized intensity maps are produced by multiplying all  $S_a$  values by their associated period; this normalization is based on the assumption that  $S_a$  values predicted by the GMPE are approximately inversely proportional to their period, which is reasonable for the range of building periods considered in this example. For other building stocks, different normalization techniques may be more effective. The clustering then proceeds using the random variable representing the sum of the normalized  $S_a$  values for the intensities in the entire region.

In this study, Stage 2 of the cluster analysis groups the intensity maps from each of the  $k_1$  clusters into  $k_2$  sub-clusters, based on each map's vector of inter-event residuals. Since there are six structural classes considered in this example (*i.e.* six building periods), the inter-event residuals for each intensity map form a vector of six quantities. Stage 2 insures that each cluster of intensity maps has similar inter-event residuals. After Stage 2, there are a total of  $k_1 \times k_2$  clusters. In the final clustering stage, the maps in each of the clusters from Stage 2 are grouped into  $k_3$  sub-clusters, based on their vector quantities of normalized  $S_a$  values in the region.

To do the clustering for the example region and building stock,  $k1=10$ ,  $k2=10$ , and  $k3=15$ <sup>15</sup>. However, the total number of clusters is  $K = 1,301$  rather than  $K = k1 \times k2 \times k3 = 1,500$ , because some of the clusters that are formed in stage 2 of the cluster analysis have fewer than 15 maps; in such cases, the number of  $k3$  sub-clusters is less than 15. Figure 6.9 plots  $Sa$  at  $T=0.91$  seconds for pairs of intensity maps that are randomly selected from three different clusters, illustrating that intensity maps belonging to the same cluster are similar to one another.

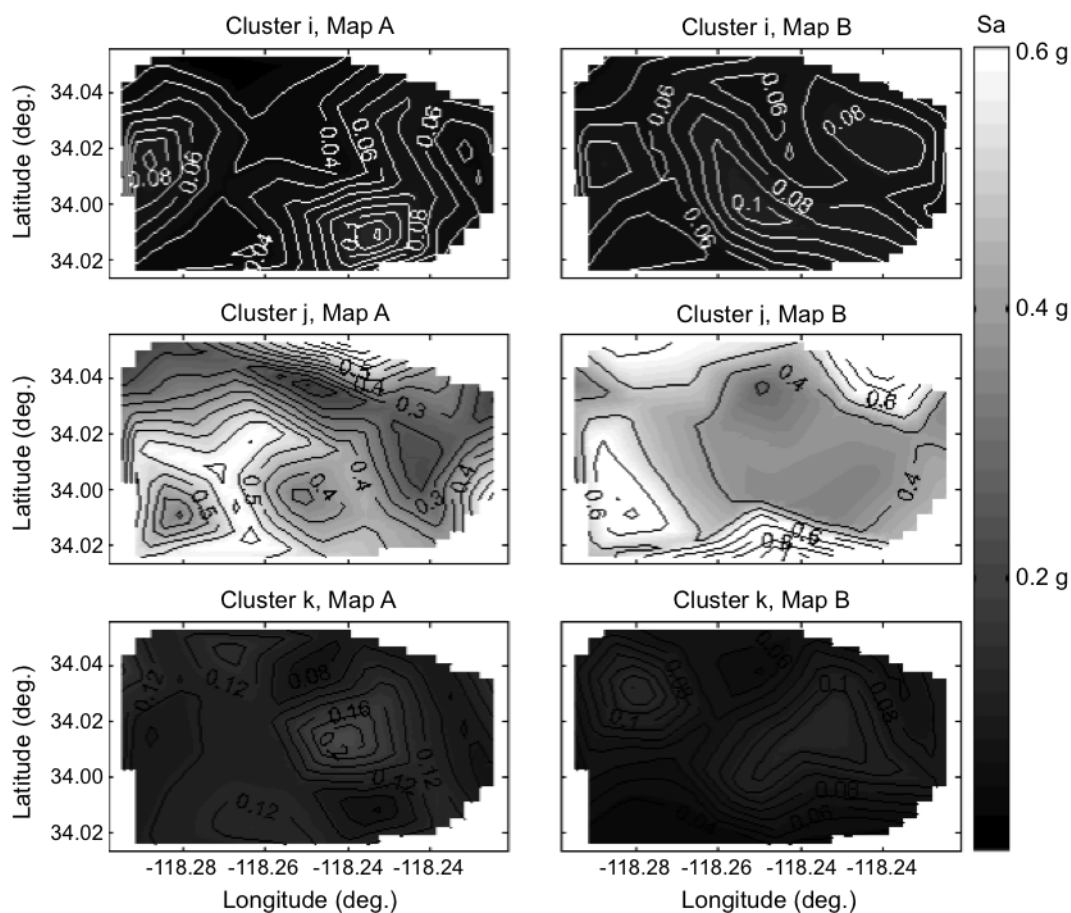


**Figure 6.9** Sample of intensity maps from three clusters denoted i, j, and k, where maps ‘A’ and ‘B’ are randomly sampled from the group of maps belonging to a given cluster. For this illustration,  $Sa$  is  $Sa(T_f=0.91 \text{ sec})$ .

<sup>15</sup> The values of  $k1$ ,  $k2$ , and  $k3$  are based on judgment. Computational efficiency can be increased by increasing  $k1$  and decreasing  $k3$ . Based on, Jayaram and Baker (2010) the product of  $k1$  and  $k3$  should be at least 150.

Since each cluster is composed of similar intensity maps, one map is selected from each cluster to represent all of the maps in the cluster for the subsequent loss analysis. The representative intensity map is randomly selected from all of the maps in the cluster, with the probability of selecting any particular map being proportional to its importance sampling weight. For representing the regional seismic hazard, a new importance sampling weight is assigned to the representative map ( $IS_{RM}$ ), which is equal to the sum of the weights for all of the intensity maps within the cluster, according to Equation 6.7.

$$IS_{RM} = \sum_{\text{All maps in } k^{\text{th}} \text{ cluster}} IS_m * \frac{1}{r} * IS_{\epsilon,j} * IS_{\eta,j} \quad 6.7$$

## 6.7 Computing Regional Losses

### 6.7.1 Overview

A realization of regional loss experienced by the building stock is generated for each intensity map, and the results are compounded to quantify the seismic risk of the region. Losses are computed according to a method proposed by DeBock et al. 2013, which is referred to as “Simplified<sub>1</sub>” in Chapter 4. Regional seismic risk is estimated from the set of representative intensity maps by the following steps applied to each map:

1. Compute losses for collapsed buildings
2. Compute losses for non-collapsed buildings
3. Determine regional losses for each map and compile the results to develop probabilistic assessment of regional loss

### 6.7.2 Computing Losses for Collapsed Buildings

A building is considered collapsed if  $Sa$  at its site is greater than the building’s collapse capacity that is measured in terms of  $Sa$ , *i.e.*  $Sa_{collapse}$ .  $Sa_{collapse}$  for each structural class, *e.g.* mid-

rise reinforced concrete (RC) special moment frame (SMF) buildings, is generated from a collapse capacity distribution that is a function of  $\varepsilon$ .

Adopting the approach recommended in Chapter 4, region-wide collapse capacities for each of the structural classes are randomly generated for each intensity map. The input value of  $\varepsilon$  for generating collapse capacity is its average value for earthquake realization  $j$ ,  $\varepsilon_{avg,j}$ . Recognizing that the average value of intra-event residuals for an earthquake is zero and the Boore and Atkinson (2008) GMPE has constant inter-event and total dispersion at all sites,  $\varepsilon_{avg,j}$  is computed by Equation 6.8:

$$\varepsilon_{avg,j} = \frac{\tau_j \eta_j}{\sqrt{\sigma_{ij}^2 + \tau_j^2}} \quad 6.8$$

The loss due to each collapsed building is the replacement cost of the building. Replacement costs are estimated the same way as in Chapter 4; they are based on RSMeans (2009) and range from \$160 to \$200 per gross square foot in 2009 dollars, depending on their structural class and occupancy type. Replacement costs are assumed to be lognormally distributed with dispersion of 0.4, based on recommendations from Ramirez and Miranda (2009).

### 6.7.3 Computing Losses for Non-Collapsed Buildings

For each building that is not identified as collapsed, the loss is computed from a vulnerability function that takes  $Sa$  as its input. The input  $Sa$  value is  $Sa$  at the site where the building is located. This example uses the vulnerability functions that were developed in Chapter 4. The vulnerability functions are generated by fitting local polynomial regressions to suites of loss data that are obtained with the Performance Assessment Calculation Tool, PACT (ATC 2012). The vulnerability function assumes that dispersion of the loss data is logarithmically distributed about the median value, as seen in the example vulnerability function that is shown in Figure 6.10.

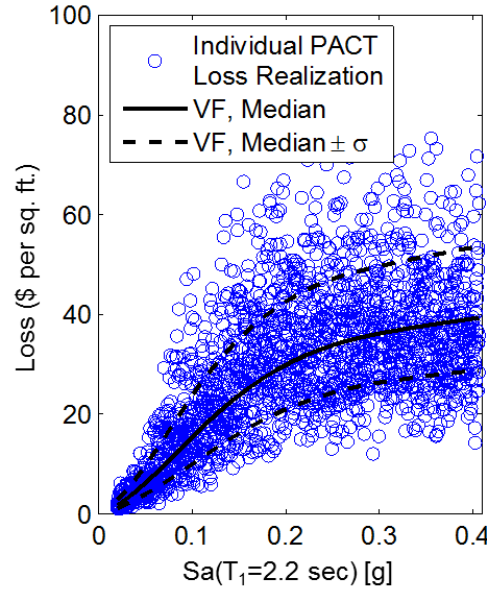


**Figure 6.10** Example vulnerability function for structural class 6 (8-story nonductile RC frames), with commercial occupancy.

#### 6.7.4 Computing Regional Losses

The regional loss for each representative intensity map ( $RL_{RM}$ ) is the sum of the losses to all of the buildings for that map:

$$RL_{RM} = \sum_{All\ bldgs.} LOSS_{Individual\ bldg.} \quad 6.9$$

The regional loss realizations from each map are combined using probabilistic methods, which are detailed in Section 6.8.

#### 6.8 Compiling the Probabilistic Regional Loss Results

The MCS analysis in this example produces 1,301 representative intensity maps, each having an associated importance sampling weight ( $IS_{RM}$ ) and regional loss ( $RL_{RM}$ ). The final step is to compile the results in ways decision-makers find meaningful and interpretable. The possibilities for presenting the regional loss information are infinite; the purpose of this section is not to explore every possibility. Rather, this section aims to present regional loss results in ways that

aid certain decision-making scenarios/perspectives. Depending on the decision at hand and the perspective of the decision-maker(s), different interpretations of the results may provide better insight than others; this section provides just a few examples of the many possibilities.

### 6.8.1 MRE for Regional Loss

A common method to present seismic risk and hazard results is via MRE curves. For a regional seismic risk analysis, this corresponds to the mean rates at which regional loss exceeds various threshold values. The importance sampling weight of each representative map ( $IS_{RM}$ ) corresponds to frequency; therefore, the MRE for a regional loss threshold  $H$  ( $MRE_H$ ) is computed by Equation 6.10:

$$MRE_H = \sum_{RM=1}^K IS_{RM} * I_{RL>H} \quad 6.10$$

where  $K$  is the total number of representative maps (1,301 in this example) and  $I_{RL>H}$  is a Boolean indicator function that is one when  $RL>H$  and zero otherwise. The MRE curve for the example building stock is shown in Figure 6.11.

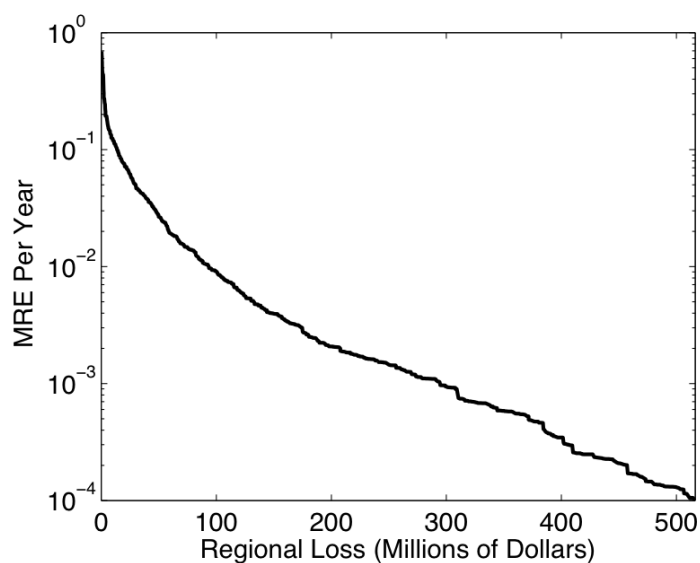


**Figure 6.11** MRE for the sample building stock for different levels of regional loss.

## 6.8.2 Dissecting the MRE Results

While a standard MRE curve is highly informative about the collective risk of a portfolio of buildings, it may be useful in some cases to also determine what specific factors are contributing to the risk or vulnerability of the region. This section explores some different ways to deaggregate the regional seismic loss results.

### 6.8.2.1 *Collapse Costs vs. Non-collapse Costs*

One way to deaggregate the data is to separate losses into two categories: costs to repair damaged buildings and their components (“non-collapse costs”) and costs to replace collapsed buildings (“collapse costs”). Figure 6.12 describes the same data as Figure 6.11, but illustrates the relative fractions of each loss level that are due to collapse costs versus non-collapsed costs. The same deaggregated loss results are plotted in Figure 6.13, but the data are smoothed with a local polynomial regression. This same smoothing technique is applied to Figure 6.14 as well.

It is evident that large rare losses are dominated by collapse costs, but small frequent losses are dominated by non-collapse costs. Based on this observation, a risk-holder concerned about mitigating large rare losses may decide to focus on improving collapse capacities through structural system improvement of buildings throughout the region, since they account for the majority of the loss in large catastrophic events. On the other hand, more frequent costs are dominated by non-collapse costs; improving building contents and components can reduce these losses.

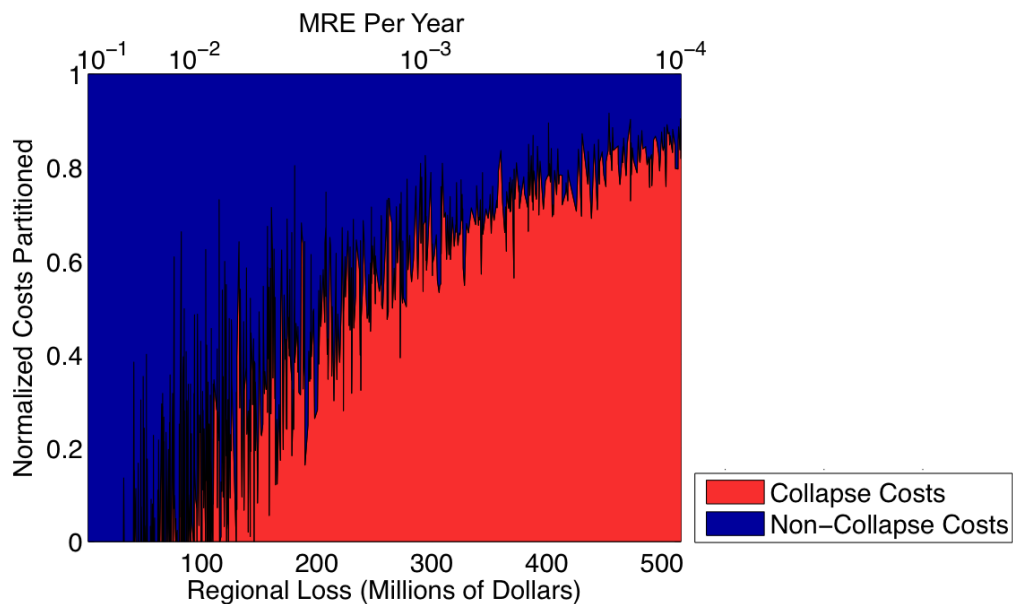


**Figure 6.12** Deaggregation of costs to show the portions of the loss due to costs for collapsed buildings versus non-collapsed buildings.

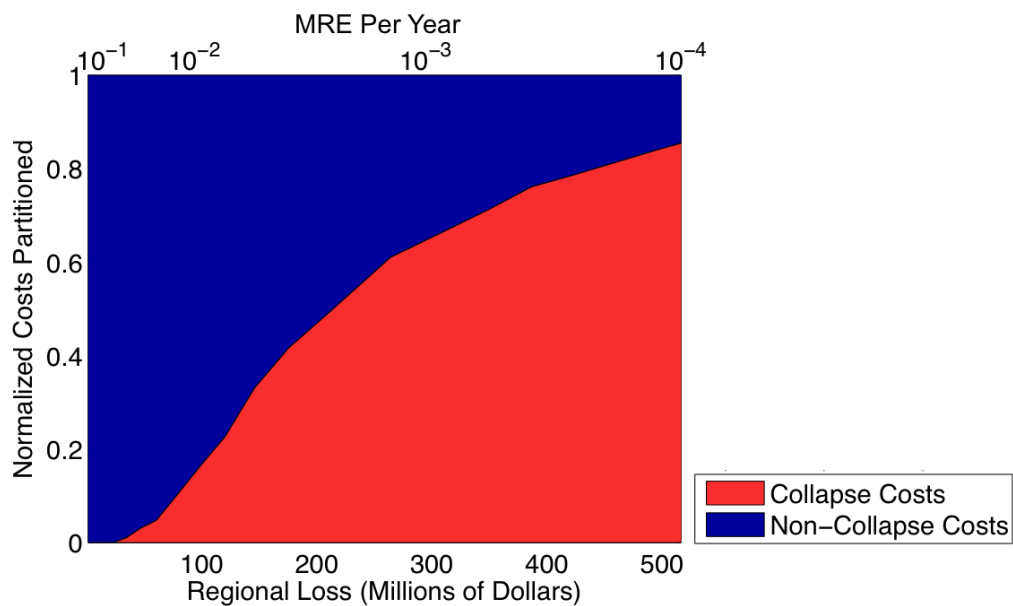


**Figure 6.13** “Smooth” Deaggregation of costs to show the portions of the loss that are due to costs for collapsed buildings versus non-collapsed buildings.

### 6.8.2.2 Losses by Structural Classification

Deaggregation of the regional loss by structural classification is presented in Figure 6.14. The results show that structural classes represented by nonductile buildings (*i.e.* structural classes 4-6) are responsible for the majority of the regional loss at all hazard levels. This representation of the regional risks is useful from a policy-making standpoint. Since nonductile buildings represent the majority of the regional risk, policies that target nonductile buildings will have the greatest impact on reducing the regional seismic risk.

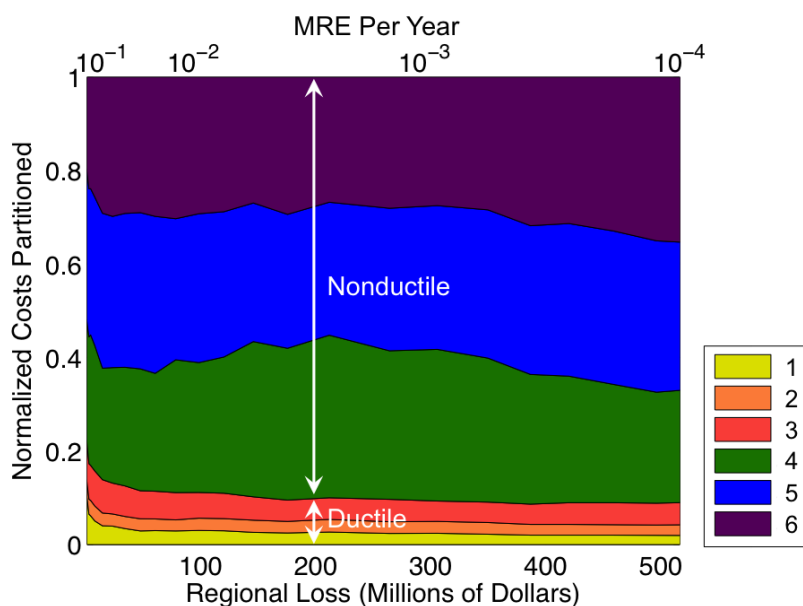


**Figure 6.14** Deaggregation of costs to show the portions of the loss that are due to costs for the different structural classes.

Nonductile buildings contribute more to regional seismic risks than ductile buildings in this example partly because there are more of them. Therefore, the deaggregated loss plot shown in Figure 6.14 may be misleading for a risk-holder who is interested in investing limited resources as effectively as possible. Another way to view the deaggregated regional risk is to compute the MRE for each structural class individually and then normalize it by the cost to replace all of the

buildings belonging to that structural class, *i.e.* to compute the “relative risk” for each class of structures and in Figure 6.15.

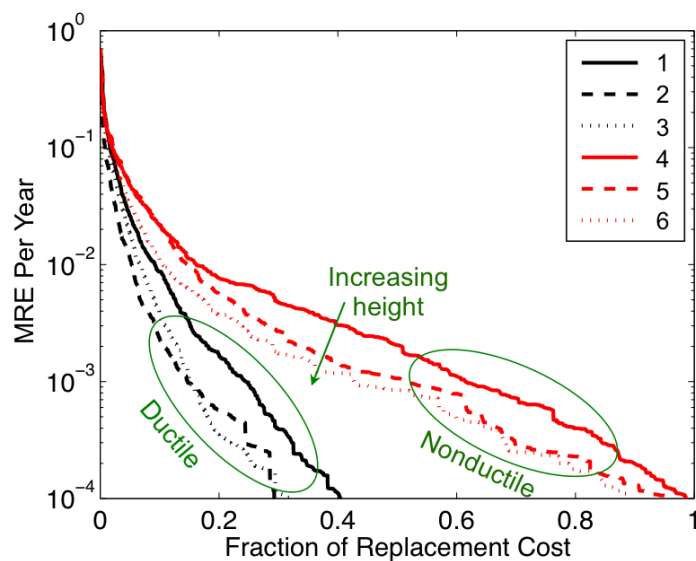


**Figure 6.15** MRE plot for each structural class, normalized by the cost to replace all of the buildings in the structural class.

Figure 6.15 shows that the relative risks of nonductile buildings (represented by structural classes 4-6) are much higher than for ductile buildings (structural classes 1-3). In addition, the relative risks generally decrease as height increases, which is a result of the taller buildings collapsing less frequently and having damage concentrated only in a fraction of their stories for non-collapsed cases. For example, the relative losses of structural classes 1, 2, and 3 for a 100-year return period ( $MRE=10^{-2}$ ) are 0.09, 0.05, and 0.07, respectively (*e.g.* an event causing damage to buildings belonging to structural class 1 that is equal to or greater than 9% of the cost to replace all of the buildings in structural class 1 is expected to occur once in 100 years). The relative 100-year losses for structural classes 4, 5, and 6 are 0.16, 0.15, and 0.11. Therefore, height and ductility are both important factors for risks in 100-year events. For 1000-year events ( $MRE=10^{-3}$ ), the relative losses for structural classes 1, 2, and 3 are 0.25, 0.15 and 0.15,

respectively and 0.62, 0.52, and 0.43 for structural classes 4, 5, and 6, respectively. The relative regional loss due to nonductile buildings is nearly three times greater than for ductile buildings for a 1000-year loss level and is equal to more than half of the cost to replace all of the nonductile buildings; therefore, nonductile buildings pose a serious regional risk in extremely rare events.

### 6.8.2.3 Annualized Costs

Another perspective for analyzing the regional loss data is to compute the average expected loss for any given year, or “annualized cost.” The annualized costs that are summarized in Table 6.2 represent the “risk-neutral” cost for insuring a building stock (*i.e.* over infinite time, a premium of this amount, in present value dollars, is equivalent to the cost of repairing earthquake damage to the uninsured building stock). This kind of information is useful to risk-holders and ensures for establishing a lower limit for insurance premiums. The total annualized cost is 6.4 million dollars. As expected, the nonductile buildings (structural classes 4-6) represent a majority of the annualized costs (Figure 6.16). When normalized by their replacement costs, the most expensive buildings are those belonging to structural classes 4 and 5, which are the low-rise and mid-rise nonductile buildings. The mid-rise ductile buildings (structural class 2) are the least expensive in terms of normalized annual costs. The pie charts in Figure 6.16 compliment Table 6.2 by showing the percentage of the total annualized costs for which each structural class is responsible next to the breakdown of gross building area by structural class. Buildings represented by structural classes 4 and 5 (low-rise and mid-rise nonductile buildings) represent disproportionately large fractions of the annualized costs compared to their contributions to gross building area.

Table 6.2. Annualized Costs by Structural Class

Ductility Classification	Structural Class	Annualized Cost	Percentage of Replacement Cost
Ductile	1	\$193,088	0.71%
	2	\$139,024	0.34%
	3	\$368,307	0.51%
Nonductile	4	\$1,565,565	1.06%
	5	\$1,974,560	1.03%
	6	\$1,844,614	0.72%
Entire Stock		\$6,085,158	0.83%

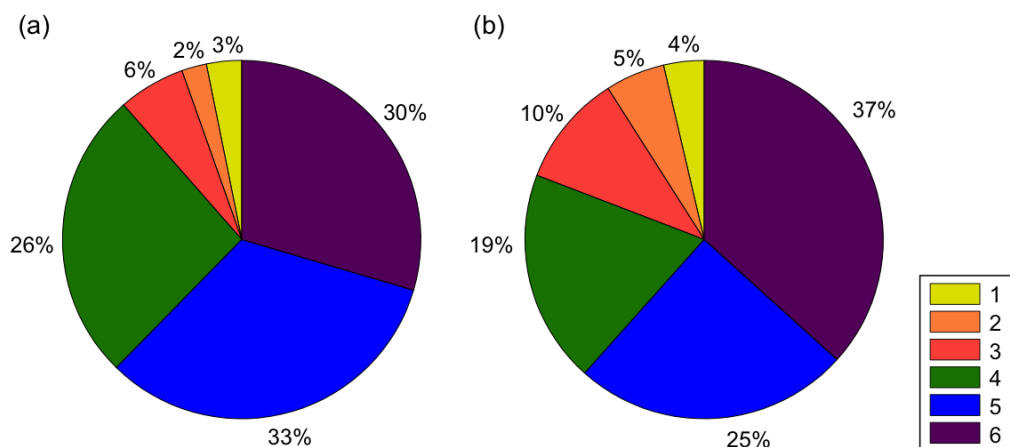


Figure 6.16 Visual breakdown of (a) annualized costs and (b) percentage of gross building area by structural class ID.

## 6.9 Summary

The implementation of a regional seismic loss assessment is documented in this chapter. For an example geographically-distributed building stock, Monte Carlo simulation (MCS) procedures are employed to: (1) generate fault ruptures; (2) produce suites of ground motion intensity maps (intensity is quantified by spectral acceleration at a buildings first-mode period,

*i.e.*  $Sa(T_1)$  or  $Sa$  for short); (3) reduce the number of intensity maps with  $k$ -means clustering; (4) compute regional losses.

Large magnitude events and high strength intensity maps are preferentially sampled with importance sampling techniques recommended by Jayaram and Baker (2010). Jayaram and Baker showed that the variance of the Mean Rates of Exceedence (MRE) curves for regional loss can be reduced by preferentially sampling in the upper tails of the magnitude and intensity distributions, because that is where MRE is most difficult to estimate.

For each intensity map, a regional loss realization is generated by the “Simplified<sub>1</sub>” method that is developed in Chapter 4. This method identifies collapsed buildings by comparing ground motion intensity at each site to a building’s collapse capacity. Collapse capacities for each structural class are generated at the onset of each regional loss computation. Losses for non-collapsed buildings are computed with vulnerability functions that take  $Sa$  as the input variable.

Regional seismic loss results for an example building stock are presented to illustrate how they can inform decisions at a community (or portfolio) level. Regional loss results for the sample building stock are deaggregated multiple ways to show how different portions of the building stock contribute to regional seismic risks. Evaluating seismic risks from a regional perspective, particularly when the risks are deaggregated by structural class, can provide policy makers and risk holders with information that they need to make risk-informed decisions concerning groups of buildings.

## 7 REFERENCES

- Abrahamson, N., and W. Silva (2008). Summary of the Abrahamson & Silva NGA ground motion relations, *Earthq. Spectra* **24** 67–97.
- ACI Committee 318 (2005). *Building code requirements for structural concrete (ACI 318-05) and commentary (318R-05)*. American Concrete Institute, Farmington Hills, Mich., pp 430.
- Altoontash, A. (2004). Simulation and Damage Models for Performance Assessment of Reinforced Concrete Beam-Column Joints, Doctoral Dissertation, Stanford University.
- Ambraseys, N., and S. Sarma (1969). Liquefaction of soils induced by earthquakes. *Bull. Seismol. Soc. Am.* **59** 651-664.
- Anagnostopoulos, S.A., C. Alexopoulou, K.G. Stathopoulos (2010). “An answer to an important controversy and the need for caution when using simple models to predict inelastic earthquake response of buildings with torsion.” *Earthquake Engineering and Structural Dynamics*. **39** 521–540.
- ASCE (2007). *Seismic Rehabilitation of Existing Buildings, ASCE Standard ASCE/SEI 41-06*, American Society of Civil Engineers, Reston, VA.
- ASCE (2010). *Minimum Design Loads for Buildings and Other Structures, ASCE Standard ASCE/SEI 7-10*, American Society of Civil Engineers, Reston, VA.
- Aslani, H. (2005). *Probabilistic Earthquake Loss Estimation and Loss Deaggregation in Buildings*, Doctoral Dissertation, Stanford University.
- Aslani, H., C. Cabrera, M. Rahnama (2012). Analysis of the sources of uncertainty for portfolio-level earthquake loss estimation. *Earthq. Eng. Struct. Dyn.* **41** 1549-1568.
- ATC (1985). *Earthquake Damage Evaluation Data for California (ATC-13)*. Applied Technology Council, FEMA Contract No. EMW-C-0912, Redwood City, CA.
- ATC (2012). *Soil-structure interaction for Building Structures (ATC-83)*. Prepared for U.S. Department of Commerce National Institute of Standards and Technology.
- Baker, J.W., and C.A. Cornell (2005). A vector-valued ground motion intensity measure consisting of spectral acceleration and epsilon, *Earthq. Eng. Struct. Dyn.* **34** 1193–1217.
- Baker, J.W., and C.A. Cornell (2006a). Spectral shape, epsilon and record selection. *Earthq. Eng. Struct. Dyn.* **34** 1193-1217.
- Baker, J.W., C.A. Cornell (2006b). Correlation of response spectral values for multicomponent ground motions. *Bull. Seismol. Soc. Am.* **96** 215-227.
- Baker, J.W and N. Jayaram (2007). Validation of ground motion simulations for engineering applications. *Poster, SCEC annual meeting, Palm Springs, CA*.
- Bal, I. E., J.J. Bommer, P.J. Stafford, H. Crowley, R. Pinho. (2010). The influence of geographical resolution of urban exposure data in an earthquake loss model for Istanbul. *Earthq. Spectra* **26** 619-634.
- Bazzurro, P., and N. Luco (2005). Accounting for uncertainty and correlation in earthquake loss estimation, *Proceedings of the Ninth International Conference on Structural Safety and Reliability, Rome, Italy*, pp. 2687-2694.
- Beck, J.L, K.A. Porter, R. Shaikhutdinov, S.K. Au, K. Mizukoshi, M. Miyamura, H. Ishida, T. Moroi, Y. Tsukada, M. Masuda (2002). *Impact of seismic risk on lifetime property values*. Report CKIV-03, Consortium of Universities for Research in Earthquake Engineering, Richmond, CA.
- Bennett, R.J. (1979). *Spatial Time Series: Analysis-Forecasting-Control*. Pion Limited, London.
- Boore, D.M., and G.M. Atkinson (2008). Ground motion prediction equations for the average horizontal component of PGA, PGV, and 5%-damped PSA at spectral periods between 0.01 s and 10.0 s, *Earthq. Spectra* **24** 99–138.
- Building Seismic Safety Council (BSSC) (2009). NEHRP Recommended Seismic Provisions for New Buildings and Other Structures, FEMA P-750. Washington, DC: Federal Emergency Management Agency.
- Campbell, K.W., and Y. Bozorgnia (2007). Campbell-Bozorgnia NGA ground motion relations for the geometric mean horizontal component of peak and spectral ground motion parameters, *Technical Report PEER 2007/02*, PEER, Berkeley, California.
- CGS (1996). *Probabilistic seismic hazard assessment for the state of California*. <http://www.consrv.ca.gov/cgs/rghm/psha/ofr9608/Pages/index.aspx>. Last accessed October 2013.
- Chang, H.Y., C.C.J. Lin, K.C. Lin, J.Y. Chen (2009). “Role of accidental torsion in seismic reliability assessment for steel buildings.” *Steel and composite structures*, **5** 457–472.

- Chiou, B., and R. Youngs (2008). An NGA model for the average horizontal component of peak ground motion and response spectra, *Earthq. Spectra* **24** 173–215.
- Chiou, B., R. Darragh, N. Gregor, and W. Silva (2008). NGA project strong-motion database. *Earthq. Spectra* **24** 23-44.
- Comerio, M.C., T. Anagnos (2012). Los Angeles inventory: implications for retrofit policies for nonductile concrete Buildings. *Proceedings of the 15<sup>th</sup> World Conference on Earthquake Engineering*, Lisbon, Portugal.
- Cornell, C.A., F. Jalayer, R.O. Hamburger, D.A. Foutch (2002). Probabilistic basis for 2000 SAC FEMA steel moment frame guidelines, *J. Struct. Eng.* **128** 526- 533.
- Crowley, H., J.J. Bommer (2006). Modeling seismic hazard in earthquake loss assessment with spatially-distributed exposure, *Bull. Earthq. Eng.* **4** 249-273.
- CSI (Computers and Structures Inc.) (2009). SAP2000 v14 Integrated Finite Element Analysis and Design of Structures. CSI, Berkeley.
- David, M., (1977). *Geostatistical ore reserve estimation*. Elsevier, Amsterdam.
- De la Llera, J.C., and A.K. Chopra (1992). "Evaluation of code-accidental torsion provisions using earthquake records from three nominally symmetric-plan buildings," *SMIP92 Seminar on Seismological and Engineering Implications of Recent Strong-Motion Data*, pp. 4-1 - 4-16.
- De la Llera, J.C., and A.K. Chopra, (1995). "Estimation of accidental torsion effects for seismic design of buildings." *J. Struct. Eng.* **121** 102-114.
- De Stefano M, B. Pintucchi (2008). "A review of research on seismic behaviour of irregular building structures since 2002". *Bull. Earthq. Eng.* **6** 285–308.
- DeBock, D.J., J.W. Garrison, K.Y. Kim, A.B. Liel (2013). Incorporation of spatial correlations between building response parameters in regional seismic loss analysis, *Bull. Seismol. Soc. Am.* In review.
- DeBock, D.J., J.W. Garrison, K.Y. Kim, and A.B. Liel (2014a), "Incorporation of spatial correlations between building response parameters in regional seismic loss analysis." *Bull. Seismol. Soc. Am.* In Press.
- DeBock, D.J. and A.B. Liel (2014b), "A comparative evaluation of probabilistic seismic loss assessment methods, using scenario case studies." *J. Earthq. Eng.* Under Review.
- Der Kiureghian A. (1996). A coherency model for spatially varying ground motions. *Earthq. Eng. Struct. Dyn.* **25** 99–111.
- Du, W., and G. Wang (2013). Intra-event spatial correlations for cumulative absolute velocity, arias intensity, and spectral accelerations based on regional site conditions. *Bull. Seismol. Soc. Am.* **103** 1117-1129.
- Elwood, K.J. (2004). "Modeling failures in Existing Reinforced Concrete Columns." *Canadian J. Civil Eng.* **31** 846-859.
- Esposito S., and I. Iervolino (2011). PGA and PGV spatial correlation models based on European multievent datasets. *Bull. Seismol. Soc. Am.* **101** 2532-2541.
- Eurocode 8 (2004). *Design Provisions for Earthquake Resistance of Structures – Part 1: General rules, seismic actions and rules for buildings*. European Committee for Standardization, Brussels
- FEMA. (2003). HAZUS-MH MR3 Tech. Manual, Wash., DC.
- FEMA (2009). *Quantification of Building Seismic Performance Factors (FEMA P-695)*. Prepared by ATC for FEMA, Washington (DC).
- FEMA (2012). *Seismic performance assessment of buildings (FEMA P-58)*. Prepared by ATC for FEMA.
- Folz, B., & Filiatrault, A. (2001). Cyclic analysis of wood shear walls. *J. Struct. Eng.* **127** 433-441.
- Fishman GS (2006). *A First Course in Monte Carlo*. Duxbury: Belmont, CA.
- Garrison, J.W. (2012). Spatial Correlations in Building Seismic Response. MS Report. CU Boulder.
- Ghannoum, W.M. and J.P. Moehle (2008). "Shear Failure Model for Flexure-Shear Critical Reinforced Concrete Columns." The 14<sup>th</sup> World Conference on Earthquake Engineering. October 12-17, 2008, Beijing, China.
- Goel, R.K., A.K. Chopra (1997). Period formulas for moment-resisting frame buildings. *J. Struct. Eng.* **123** 1454-1461.
- Goda, K., and H.P. Hong (2008a). Estimation of seismic loss for spatially-distributed buildings, *Earthq. Spectra*. **24** 889-910.
- Goda, K., and H.P. Hong (2008b). Spatial correlation of peak ground motions and response spectra, *Bull. Seismol. Soc. Am.* **98** 354–365.
- Goda, K., and G.M. Atkinson (2009). Probabilistic characterization of spatially correlated response spectra for earthquakes in Japan. *Bull. Seism. Soc. Am.* **99** 3003-3020.
- Google (2013). Google Streetview, *maps.google.com*. Last accessed April, 2013.
- Goovaerts P. (1997). *Geostatistics for Natural Resources Evaluation*. Oxford University Press: Oxford, New York.
- Graves, R.W. (2005). Broadband ground motion simulations for the Puente Hills thrust system, *USGS*.

- Graves, R.W., B.T. Aagaard, K.W. Hudnut, L.M. Star, J.P. Stewart, H.T. Jordan (2008). Broadband simulations for Mw 7.8 southern San Andreas earthquakes: Ground motion sensitivity to rupture speed. *Geophysical Research Letter*.
- Haimes, Y.Y. (1998). Risk Modeling, Assessment, and Management. New York: John Wiley & Sons, Inc.
- Haselton, C.B., and J.W. Baker (2006). "Ground motion intensity measures for collapse capacity prediction: Choice of optimal spectral period and effect of spectral shape," *Proceedings*, 8th National Conference on Earthquake Engineering, San Francisco, California.
- Haselton, C.B. and G.G. Deierlein (2007). *Assessing Seismic Collapse Safety of Modern Reinforced Concrete Frame Buildings*, PEER Report 2007/08, Pacific Earthquake Engineering Research Center, University of California, Berkeley, California.
- Haselton, C.B., A.B. Liel, S.T. Lange, G.G. Deierlein (2008). *Beam-column element model calibrated for predicting flexural response leading to global collapse of RC frame buildings*, *Pacific Earthquake Engineering Research Center*, PEER 2007/03, May, 2008.
- Haselton, C.B., A.B. Liel, G.G. Deierlein, B.S. Dean, J.H. Chou (2011a). Seismic collapse safety of reinforced concrete buildings: I. Assessment of ductile moment frames, *J. Struct. Eng.* **137** 481-491.
- Haselton, C.B., J.W. Baker, A.B. Liel, G.G. Deierlein, (2011b). Accounting for ground-motion spectral shape characteristics in structural collapse assessment through an adjustment for epsilon. *J. Struct. Eng.* **137** 332-344.
- Hastie, T., R. Tibshirani, J. Friedman (2008). *The Elements of Statistical Learning: Data Mining, Inference, and Prediction (2nd edition)*. Springer-Verlag.
- Henze, N., B. Zirkler (1990). A class of invariant consistent tests for multivariate normality. *Communications in Statistics-Theory and Methods*, **19** 3595-3617.
- Houilding, S.W. (2000). *Practical Geostatistics: Modeling and Spatial Analysis*. Springer, Berlin.
- Ibarra, L.F., R.A. Medina, H. Krawinkler (2005). "Hysteretic Models that Incorporate Strength and Stiffness Deterioration." *Earthq. Eng. Struct. Dyn.* **34** 1489- 1511.
- Jayaram, N., J.W. Baker (2009). Correlation model for spatially-distributed ground-motion intensities, *Earthq. Eng. Struct. Dyn.* **38** 1687–1708.
- Jayaram, N., J.W. Baker (2010). Efficient sampling and data reduction techniques for probabilistic seismic lifeline risk assessment, *Earthq. Eng. Struct. Dyn.* **39** 1109–1131.
- Lee R., and A. Kiremidjian (2007). Uncertainty and correlation for loss assessment of spatially-distributed systems. *Earthq. Spectra* **23** 753–770.
- Liel, A.B., C.B. Haselton, G.G. Deierlein (2011). Seismic collapse safety of reinforced concrete buildings. II: Comparative assessment of nonductile and ductile moment frames, *J. Struct. Eng.* **137** 492–502.
- Liel, A.B., G.G. Deierlein (2012), Using Assessed Collapse Risk to Inform Seismic Safety Decisions for California's Older Concrete Buildings, *Earthq. Spectra*, **28** 1495-1421.
- Loth, C., and J.W. Baker (2013). A spatial cross-correlation model of ground motion spectral accelerations at multiple periods. *Earthq. Eng. Struct. Dyn.* **42** 397-417.
- Lowes, L. N., N. Mitra, A. Altoontash (2004). A Beam-Column Joint Model for Simulating the Earthquake Response of Reinforced Concrete Frames, PEER 2003/10, Pacific Earthquake Engineering Research Center, University of California, Berkeley, California.
- McQueen, J.B. (1967). Some methods for classification and analysis of multivariate observations. *Proceedings of the 5<sup>th</sup> Berkeley Symposium on Mathematical Statistics and Probability*, Berkeley, CA.
- Mitrani-Reiser, J. (2007). *An ounce of prevention: probabilistic loss estimation for performance-based earthquake engineering*. Doctoral dissertation, California Institute of Technology.
- MOC (2008). *Manual de diseño de obras civiles. Diseño por sismo. Recomendaciones y Comentarios*. Instituto de Investigaciones Eléctricas, Comisión Federal de Electricidad, (in Spanish).
- Montgomery, D.C., and G.C. Runger (2007). *Applied Statistics and Probability for Engineers (4<sup>th</sup> edition)*, John Wiley and Sons, Inc.
- NRCC (2010). *National Building Code of Canada (NBCC)*, 13th ed., National Research Council of Canada, Ottawa, ON.
- NZS (2004). *New Zealand Standard, Structural Design Actions Part 5: Earthquake actions*. New Zealand.
- Olsen, A.H., and K.A. Porter (2011). What we know about demand surge: Brief summary. *Natural Hazards Review*, **12**, 62-71.
- OpenSHA. *Open Source Seismic Hazard Analysis*. <http://www.opensha.org/>. Last accessed October 2013.
- Park, J., P. Bazzurro, J.W. Baker (2007). Modeling spatial correlation of ground motion intensity measures for regional seismic hazard and portfolio loss estimation, *ICASP 10*, Tokyo, Japan.

- PEER. (2011). "OpenSees (Open System for Earthquake Engineering Simulation)." January, 2011, from OpenSees.berkeley.edu.
- Porter, K.A., A.S. Kiremidjian, J.S. LeGrue (2001). Assembly-based vulnerability of buildings and its use in performance evaluation. *Earthq. Spectra*, **17** 291-312.
- Porter, K.A., R. Kennedy, R. Bachman (2007). Creating Fragility Functions for Performance- Based Earthquake Engineering. *Earthq. Spectra* **23** 471-489.
- Ramirez, C.M., and E. Miranda (2009). *Building-specific Loss Estimation Methods & Tools for Simplified Performance-based Earthquake Engineering*. The John A. Blume Earthquake Engineering Center, Department of Civil and Environmental Engineering, Stanford University, Stanford (CA). Report No. 171.
- Royston, J. P. (1983). Some techniques for assessing multivariate normality based on the shapiro-wilk W. *Applied Statistics*, 121-133.
- Rowe, K. (2011). *Probabilistic Assessment of Building Response to Simulated and Recorded Ground Motions*, MS Thesis. CU Boulder.
- RSMMeans (2009). *Square Foot Costs: 30<sup>th</sup> Annual Edition*. R.S. Means Company, Inc. Kingson, MA.
- Rubin, C.M., K. Sieh, Y.G. Chen, J.C. Lee, H.T. Chu, R. Yeats, K. Mueller, Y.C. Chan (2001). Surface rupture and behavior of thrust faults probed in Taiwan. *Eos, Transactions American Geophysical Union*, **82** 565-569.
- Sokolov V., F. Wenzel, W.Y. Jean, and K.L. Wen (2010). Uncertainty and spatial correlation of earthquakes ground motion in Taiwan. *Terrestrial, Atmospheric and Oceanic Sciences* 21, no. 6, 905-921.
- Star, L. M., J.P. Stewart, R.W. Graves, R. W. (2011). Comparison of ground motions from hybrid simulations to NGA prediction equations. *Earthq. Spectra* **27** 331-350.
- Stathopoulos, K.G., S.A. Anagnostopoulos (2010). "Accidental design eccentricity: Is it important for the inelastic response of buildings to strong earthquakes?" *Soil Dyn. and Earthq. Eng.* **30** 782-797.
- Therneau, T.M. and B. Atkinson (2010). *Recursive Partitioning*. R port by Brian Ripley. R package version 3.1-48. October, 2011 from <http://CRAN.R-project.org/package=rpart>.
- Tsai, K.C., C.P. Hsiao, M. Bruneau (2000). Overview of building damages in 921 Chi-Chi earthquake J. Earthquake Eng. Eng. Seismol. **2** 93-108.
- Tso, W.K., and R.S. Smith (1999). "Re-evaluation of seismic torsional provisions," *Earthq. Eng. Struct. Dyn.* **28** 899-917.
- USGS (2009). *Earthquake Probability Mapping*. <https://geohazards.usgs.gov/eqprob/2009/index.php>. Last accessed October 2013.
- USGS (2010). *Predefined Vs30 Mapping*. <http://earthquake.usgs.gov/hazards/apps/vs30/>. Last accessed November 2013.
- Vasudevan, R., A.S. Kiremidjian, H.C. Howard (1992). *An Integrated Inventory Methodology for Seismic Damage Assessment*. Blume Earthquake Engineering Center, Dept. of Civil and Environmental Engineering, Stanford University, Stanford, CA. Report No. 102.
- Vamvatsikos, D., and C.A. Cornell (2002). Incremental dynamic analysis. *Earthq. Eng. Struct. Dyn.* **31** 491-514
- Vaziri P., R. Davidson, P. Apivatanagul, L. Nozick (2012). Identification of optimization-based probabilistic earthquake scenarios for regional loss estimation. *J. Earthq. Eng.* **16** 296-315.
- Wang M. and T. Takada (2005). Macrospatial correlation model of seismic ground motions, *Earthq. Spectra* **21** 1137-1156.
- Weisstein, E., Great Circle. MathWorld. <http://mathworld.wolfram.com/GreatCircle.html>. (Last accessed Oct. 2012).
- Wells, D. L. and K.J. Coppersmith (1994). New empirical relationships among magnitude, rupture length, rupture width, rupture area, and surface displacement. *Bull. Seismol. Soc. Am.*, **84** 974-1002.
- Wesson, R. L., and D. M. Perkins (2001). Spatial correlation of probabilistic earthquake ground motion and loss, *Bull. Seismol. Soc. Am.* **91** 1498-1515.
- Youngs, R.R. and K.J. Coppersmith (1985). Implications of fault slip rates and earthquake recurrence models to probabilistic seismic hazard estimates. *Bull. Seismol. Soc. Am.*, **75** 939-964.